



University of Kentucky
UKnowledge

Theses and Dissertations--Electrical and
Computer Engineering

Electrical and Computer Engineering


2018

ADVANCED SYNCHRONOUS MACHINE MODELING

YuQi Zhang

University of Kentucky, yuqi.zhang@uky.edu

Author ORCID Identifier:

 <https://orcid.org/0000-0002-2878-2775>

Digital Object Identifier: <https://doi.org/10.13023/ETD.2018.211>

[Right click to open a feedback form in a new tab to let us know how this document benefits you.](#)

Recommended Citation

Zhang, YuQi, "ADVANCED SYNCHRONOUS MACHINE MODELING" (2018). *Theses and Dissertations--Electrical and Computer Engineering*. 118.

https://uknowledge.uky.edu/ece_etds/118

This Doctoral Dissertation is brought to you for free and open access by the Electrical and Computer Engineering at UKnowledge. It has been accepted for inclusion in Theses and Dissertations--Electrical and Computer Engineering by an authorized administrator of UKnowledge. For more information, please contact UKnowledge@lsv.uky.edu.

STUDENT AGREEMENT:

I represent that my thesis or dissertation and abstract are my original work. Proper attribution has been given to all outside sources. I understand that I am solely responsible for obtaining any needed copyright permissions. I have obtained needed written permission statement(s) from the owner(s) of each third-party copyrighted matter to be included in my work, allowing electronic distribution (if such use is not permitted by the fair use doctrine) which will be submitted to UKnowledge as Additional File.

I hereby grant to The University of Kentucky and its agents the irrevocable, non-exclusive, and royalty-free license to archive and make accessible my work in whole or in part in all forms of media, now or hereafter known. I agree that the document mentioned above may be made available immediately for worldwide access unless an embargo applies.

I retain all other ownership rights to the copyright of my work. I also retain the right to use in future works (such as articles or books) all or part of my work. I understand that I am free to register the copyright to my work.

REVIEW, APPROVAL AND ACCEPTANCE

The document mentioned above has been reviewed and accepted by the student's advisor, on behalf of the advisory committee, and by the Director of Graduate Studies (DGS), on behalf of the program; we verify that this is the final, approved version of the student's thesis including all changes required by the advisory committee. The undersigned agree to abide by the statements above.

YuQi Zhang, Student

Dr. Aaron M. Cramer, Major Professor

Dr. Caicheng Lu, Director of Graduate Studies

ADVANCED SYNCHRONOUS MACHINE MODELING

DISSERTATION

A dissertation submitted in partial fulfillment of the
requirements for the degree of Doctor of Philosophy in the
College of Engineering at the University of Kentucky

By

YuQi Zhang

Lexington, Kentucky

Director: Dr. Aaron M. Cramer, Associate Professor of Electrical Engineering

Lexington, Kentucky

2018

Copyright© YuQi Zhang 2018

ABSTRACT OF DISSERTATION

ADVANCED SYNCHRONOUS MACHINE MODELING

The synchronous machine is one of the critical components of electric power systems. Modeling of synchronous machines is essential for power systems analyses. Electric machines are often interfaced with power electronic components. This work presents an advanced synchronous machine modeling, which emphasizes on the modeling and simulation of systems that contain a mixture of synchronous machines and power electronic components. Such systems can be found in electric drive systems, dc power systems, renewable energy, and conventional synchronous machine excitation. Numerous models and formulations have been used to study synchronous machines in different applications. Herein, a unified derivation of the various model formulations, which support direct interface to external circuitry in a variety of scenarios, is presented. Selection of the formulation with the most suitable interface for the simulation scenario has better accuracy, fewer time steps, and less run time.

Brushless excitation systems are widely used for synchronous machines. As a critical part of the system, rotating rectifiers have a significant impact on the system behavior. This work presents a numerical average-value model (AVM) for rotating rectifiers in brushless excitation systems, where the essential numerical functions are extracted from the detailed simulations and vary depending on the loading conditions. The proposed AVM can provide accurate simulations in both transient and steady states with fewer time steps and less run time compared with detailed models of such systems and that the proposed AVM can be combined with AVM models of other rectifiers in the system to reduce the overall computational cost.

Furthermore, this work proposes an alternative formulation of numerical AVMs of machine-rectifier systems, which makes direct use of the natural dynamic impedance of the rectifier without introducing low-frequency approximations or algebraic loops. By using this formulation, a direct interface of the AVM is achieved with inductive circuitry on both the ac and dc sides allowing traditional voltage-in, current-out formulations of the circuitry on these sides to be used with the proposed formulation directly. This numerical AVM formulation is validated against an experimentally validated detailed model and compared with previous AVM formulations. It is demonstrated that the proposed AVM formulation accurately predicts the system's low-frequency behavior during both steady and transient states, including in cases where previous AVM formulations cannot predict

accurate results. Both run times and numbers of time steps needed by the proposed AVM formulation are comparable to those of existing AVM formulations and significantly decreased compared with the detailed model.

KEYWORDS: AC machines, electric machines, brushless machines, converters, generators, simulation.

YuQi Zhang

Author's signature

May 29, 2018

Date

ADVANCED SYNCHRONOUS MACHINE MODELING

By

YuQi Zhang

Aaron M. Cramer
Director of Dissertation

Caicheng Lu
Director of Graduate Studies

May 29, 2018

Date

This work is dedicated to my family and friends.

ACKNOWLEDGEMENTS

The research work in this dissertation is supported by the Office of Naval Research (ONR) through the United States Naval Academy N00189-14-P-1197 and through the ONR Young Investigator Program N00014-15-1-2475.

First, I would like to express my gratitude to my adviser Dr. Aaron M. Cramer for his guidance, support, and encouragement through the learning process of this dissertation. It was a wonderful experience for me to study in power electronics lab. Also, I would like to thank my committee members, Dr. Bruce Walcott, Dr. Yuan Liao, and Dr. Joseph Sottile, and the outside examiner Dr. Zongming Fei for the time they spent on my dissertation review and the valuable comments and suggestions.

Furthermore, I would like to thank all the members of power electronics lab group who have helped me and supported me throughout my work.

Finally, I would like to give many thanks to my loved ones, who have supported me throughout the entire process. I will be grateful forever for your constant support and help.

TABLE OF CONTENTS

Acknowledgements	iii
Table of Contents	iv
List of Tables	vi
List of Figures	vii
1 Introduction	1
2 Background and Literature Review	4
2.1 Background	5
2.1.1 Construction of Synchronous Machines	5
2.1.2 Voltage, Flux Linkage and Torque Equations in Machine Variables	6
2.1.3 Voltage and Flux Linkage Equations in Arbitrary Reference Frame Variables	14
2.1.4 Park's Equations and Equivalent Circuits	15
2.2 Literature Review	20
3 Unified Model Formulations for Synchronous Machine Model with Saturation and Arbitrary Rotor Network Representation	28
3.1 Notation	29
3.2 Synchronous Machine Model	30
3.3 Model Formulations	43
3.3.1 qd Formulation	44
3.3.2 SVBR Formulation	46
3.3.3 FVBR Formulation	46
3.3.4 SFVBR Formulation	47
3.4 Formulation Comparison	48
4 Numerical Average-Value Modeling of Rotating Rectifiers in Brushless Excitation Systems	56
4.1 Average-Value Model of Brushless Excitation System	57
4.1.1 Notation	57
4.1.2 Rectifier relationships	58
4.1.3 Brushless exciter model	59
4.1.4 Differentiator approximation	61
4.1.5 Model integration	63
4.1.6 Model summary	64
4.2 Rectifier Characterization	66
4.3 Model Validation	68

5	Formulation of Rectifier Numerical Average-Value Model for Direct Interface with Inductive Circuitry	82
5.1	Average-Value Model of Machine-Rectifier Systems	83
5.1.1	Notation	83
5.1.2	Rectifier relationships	84
5.1.3	Model summary	86
5.2	Rectifier Characterization	87
5.3	Model Validation	89
5.3.1	Main machine and stationary rectifier load	90
5.3.2	Exciter, rotating rectifier, main machine, and infinite bus	94
5.3.3	Exciter, rotating Rectifier, main machine, and stationary rectifier load	97
6	Conclusion and Future Work	102
6.1	Conclusion	102
6.2	Future Work	103
	Bibliography	107
	Vita	116

LIST OF TABLES

3.1	Case Results	50
4.1	Brushless Exciter Parameters	68
4.2	Support Points for Functions $\alpha(\cdot)$, $\beta(\cdot)$, and $\phi(\cdot)$	70
4.3	Model Computational Efficiency	71
5.1	Support Points for Stationary Rectifier Functions $\alpha(\cdot)$, $\beta(\cdot)$, and $\phi(\cdot)$	91
5.2	Support Points for Rotating Rectifier Functions $\alpha(\cdot)$, $\beta(\cdot)$, and $\phi(\cdot)$	92
5.3	Model Computational Efficiency	93

LIST OF FIGURES

2.1	Two-pole, three-phase, wye-connected, salient-pole synchronous machine [1]	7
2.2	Equivalent circuits of a three-phase synchronous machine in the rotor reference frame [1]	18
3.1	Synchronous machine model in rotor reference frame.	30
3.2	Summary of model formulations. The integrators associated with the mechanical state variables are represented within the Mechanical Model block.	45
3.3	Case II arrangement.	51
3.4	Case II results.	52
3.5	Case III arrangement.	53
3.6	Case III results.	53
3.7	Case IV arrangement.	54
3.8	Case IV results.	55
4.1	Stationary rectifier system.	58
4.2	Rotating rectifier system.	59
4.3	Summary of model formulation (dashed lines represent external interfaces to/from the proposed model).	65
4.4	Functions $\alpha(\cdot)$, $\beta(\cdot)$, and $\phi(\cdot)$.	69
4.5	Case I (excitation voltage step change) results.	72
4.6	Case I (excitation voltage step change) results.	73
4.7	Case II (terminal voltage step change) results.	75
4.8	Case II (terminal voltage step change) results.	76
4.9	Case III circuit.	77
4.10	Case III (rectifier load step change) results.	79
4.11	Case III (rectifier load step change) results.	80
4.12	Case III (rectifier load step change) results (exciter armature q -axis current during transient and steady-state conditions and FFT results). The stationary, rotating, and full AVM each represent numerical AVMs.	81
5.1	Rectifier.	86
5.2	Summary of model formulation (dashed lines represent external interfaces from/to the proposed model).	87
5.3	Stationary functions $\alpha(\cdot)$, $\beta(\cdot)$, and $\phi(\cdot)$.	89
5.4	Rotating functions $\alpha(\cdot)$, $\beta(\cdot)$, and $\phi(\cdot)$.	90
5.5	Case I and Case II arrangement.	92
5.6	Case I (excitation voltage step change) results.	94
5.7	Case II (dc fault) results.	95
5.8	Case III and Case IV arrangement.	96
5.9	Case III (rotor angle change) results.	97
5.10	Case IV (ac fault) results.	98

5.11 Case V and Case VI arrangement. 99
5.12 Case V (excitation voltage step change) results. 99
5.13 Case VI (dc fault) results. 101

Chapter 1

Introduction

The synchronous machine, featuring its shaft rotation synchronized with the frequency of the supply current, is one of the critical components of electric power systems. An electric power system, by definition a network of electrical components used to supply, transmit and use electric power, broadly consists of four main elements: generation, transmission, distribution, and loads. Generators supply the electric power; transmission systems carry the power from generation stations to load centers; distribution systems feed the power to industries and homes in the neighborhood; and loads are the terminals of the power system, consuming the electric power. Synchronous machines are widely recognized as generator units in various power systems [2–8]. Almost all electrical energy utilized around the world is generated by synchronous machines. Also, synchronous machines are used in motor applications from the load side.

Modeling of synchronous machines is essential for power systems analyses. As a generator, it determines the electric characteristics of the power system, especially for the system security, the ability to withstand sudden disturbances such as faults, switching, and load changes [9–11]. The power system behavior is also dependent on the electrical and electromechanical processes of synchronous machines. However, it is generally impractical to conduct experiments and diagnosis directly on the main power grid. As an alternative, modeling synchronous machines can achieve further insight in the complex electro-magnetic behavior of the machine, as well as power systems simulation and analy-

ses [12–14].

Synchronous machine modeling has been extensively studied for decades. Various models have been proposed in the literature. Most analytical models for synchronous machines are based on Park’s transformation [15]. Those models are formulated in terms of variables of fictitious windings in the rotor reference frame. The advantages of this formulation are 1) the corresponding equations become time invariant since they are independent of rotor position; and 2) the state variables are constant in the steady state. Thus, using these fictitious variables can simplify the machine analysis. However, the disadvantage is its inherently inefficient to represent converter circuits for machine-converter systems.

Synchronous machine-converter systems are widely used in automobiles, ships, airplanes and brushless excitation systems. Modeling the machine-converter interface is important for numerical accuracy and computational performance of the overall simulation. In the traditional qd models, the interface modeling is typically resolved by using a resistive or capacitive snubber circuit, which is required to calculate the interfacing voltage and leads to multiple numerical disadvantages. The VBR models can achieve a direct interface of machine models with the external electrical networks.

Numerous models and formulations have been used to study synchronous machines in different applications. Herein, a unified derivation of the various model formulations, which support direct interface to external circuitry in a variety of scenarios, is presented. A synchronous machine model with magnetizing path saturation including cross-saturation and an arbitrary rotor network representation is considered. This model has been extensively experimentally validated and includes most existing machine models as special cases. Derivations of the standard voltage-in, current-out formulation as well as formulations in which the stator and/or the field windings are represented in a voltage-behind-reactance form are presented in a unified manner, including the derivation of a field-only voltage-behind-reactance formulation. The formulations are compared in a variety of simulation scenarios to show the relative advantages in terms of run time and accuracy. It has

been demonstrated that selection of the formulation with the most suitable interface for the simulation scenario has better accuracy and less run time.

Numerical average-value modeling has been successfully applied in a variety of cases involving machine-converter interactions. These techniques are adapted to the rotating rectifier in a brushless excitation system in this study. A numerical average-value modeling of rotating rectifiers in brushless excitation systems is proposed. This model averages the periodic switching behavior of the rotating rectifier. Furthermore, an alternative formulation of numerical AVMs of machine-rectifier systems is developed, which works for both stationary rectifiers and rotating rectifiers. In the proposed formulation, it is not necessary to introduce low-frequency approximations or to invert the voltage-current interfaces on either the ac or dc side. The proposed AVM formulation is validated with an experimentally validated detailed model and compared with previous AVM formulations. The results show that the low-frequency behavior of the system is accurately represented and that the high computational efficiency associated with existing AVM formulations is retained. Because the proposed AVM formulation can be directly included in simulation models with traditional voltage-in, current-out formulations of the ac and dc equipment, it can be readily used with existing models of such equipment in commercial simulation toolboxes.

The remainder of this work is organized as follows. Chapter 2 provides the background on synchronous machines and their modeling, and also reviews existing techniques for electrical machines modeling. Chapter 3 presents unified model formulations for synchronous machine model with saturation and arbitrary rotor network representation. A numerical average-value modeling of rotating rectifiers in brushless excitation systems and a formulation of rectifiers numerical average-value model for direct interface with inductive circuitry are proposed in Chapter 4 and Chapter 5, respectively. A concluding summary and areas of future work are provided in Chapter 6.

Chapter 2

Background and Literature Review

Synchronous machines are very important electromechanical energy-conversion devices, which play a key role both in the production of electricity and in certain special drive applications. Synchronous generators convert mechanical energy from the hydro or steam turbines or combustion engines into electric energy. In most power systems, 99% of the electrical power is generated by synchronous generators. Synchronous motors find applications in all industrial applications where constant speed is necessary. Also, synchronous motors are employed as power factor correction and voltage regulation.

Analytical modeling of synchronous machines has been extensively studied with and without magnetic saturation, including using the physical variables in the physical form and the fictitious variables in the rotor reference frame. For the physical variables in the physical form, the corresponding equations and the state variables are time-varying. By transforming the stator variables to the rotor reference frame based on Park's equations, the corresponding equations eliminate the time-dependent inductances and become invariant, also the state variables become constant in the steady state. Yet, it is difficult to represent converter circuits in terms of the transformed stator variables. If the machine is represented in terms of physical variables, little work is required from the system analyst's perspective, and greatly reduces the work needed in modeling a machine-converter system.

Synchronous machines are usually acknowledged to be accurately modeled by two lumped-parameter equivalent circuits representing the q -axis and the d -axis. The number

of the rotor damper branches is selected in accordance with the rotor design. In current research literature, the rotor branches are designed with low-order circuits in which the components are with specific physical meanings. The equivalent circuits are modeled for some particular applications/conditions.

This chapter gives the background information related to this work and a literature review about the typical models of synchronous machines in recent years.

2.1 Background

2.1.1 Construction of Synchronous Machines

The principal components of a synchronous machine are the stator and the rotor. The stator carries three armature windings (three-phase), which are identical sinusoidally distributed windings displaced from each other by 120 degrees. The rotor carries field windings and may have one or more damper windings. Field windings are connected to an external dc current source via slip rings and brushes or to a revolving dc source via a special brushless configuration, producing the main magnetic field. The strength of the magnetic field is proportional to the applied field current which is aligned with the axis of the field windings. The rotor behaves as a large electromagnet and may be replaced by a permanent magnet. The magnetic poles can be either salient (sticking out of the rotor's core) or non-salient constructions. Generally, non-salient structure is used for high-speed synchronous machines, such as steam turbine generators, while salient pole structure is used for low-speed applications, such as hydroelectric generators. Salient-pole machines have magnetically unsymmetrical rotors, which limits the applicability of transforming rotor variables. However, the stator variables are usually referred to the rotor reference frame based on Park's transformation, or to the arbitrary reference frame for better analytical modeling and simulating electrical machines.

The inductances of the stator windings are the places where the energy is stored, and

the amount of energy stored depends on the rotor position. As the rotor moves, there is a change in the energy stored. In synchronous motors, the energy is extracted from the magnetic field and becomes the mechanical energy. In synchronous generators, the energy is stored in the magnetic field and eventually flows into the electrical circuit that powers the stator. The rotor is turned by external means in order to produce a rotating magnetic field. The frequency of the power is synchronized with the mechanical rotational speed.

2.1.2 Voltage, Flux Linkage and Torque Equations in Machine Variables

A typical synchronous machine (two-pole, three-phase, wye-connected, salient-pole synchronous machine), which is shown in Figure 2.1, can be used to predict the electrical and electromechanical behavior of most synchronous machines [1]. The stator windings are identical sinusoidally distributed and physically displaced from each other by 120 degrees. Axes represent the direction in which the current in the coil produces the magnetic flux. The as , bs , and cs axes represent the magnetic axes of the stator windings. The stator windings have N_s equivalent turns with resistance r_s . The rotor carries a field winding (fd winding) and three damper windings (kd , $kq1$ and $kq2$ windings), which are all sinusoidally distributed. The fd winding has N_{fd} equivalent turns with resistance r_{fd} . The kd winding, which has the same magnetic axis as the field winding, has N_{kd} equivalent turns with resistance r_{kd} . The direct axis (d axis) is the magnetic axis of the fd and kd windings. The $kq1$ winding has N_{kq1} equivalent turns with resistance r_{kq1} . The $kq2$ winding has N_{kq2} equivalent turns with resistance r_{kq2} . The quadrature axis (q axis) is the magnetic axis of the $kq1$ and $kq2$ windings. The d axis is displaced 90 degrees behind of the q axis as shown in Figure 2.1. θ_r is the electrical angular position. ω_r is the electrical angular velocity.

It is assumed that the direction of positive stator currents is into the terminals. The

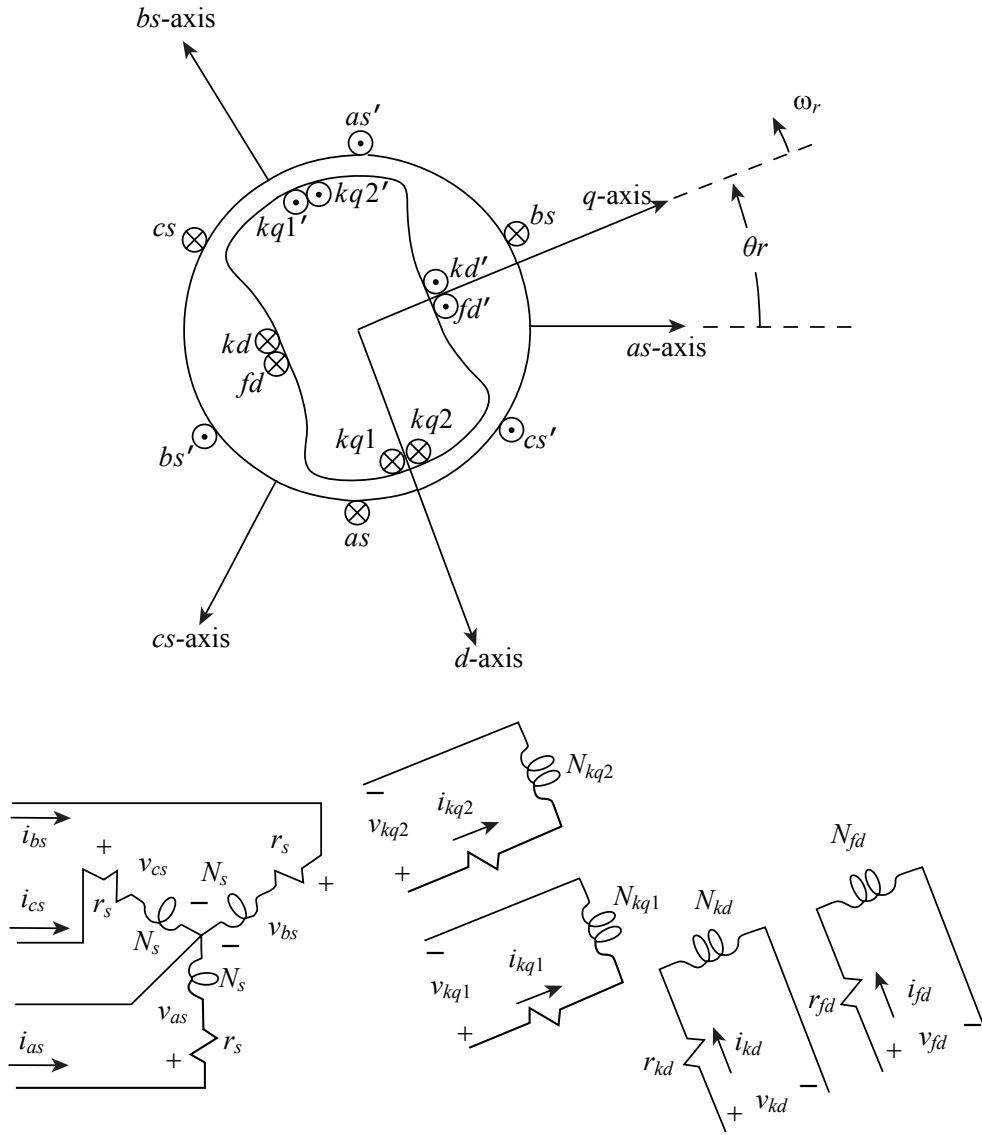


Figure 2.1: Two-pole, three-phase, wye-connected, salient-pole synchronous machine [1]

voltage equations in machine variables can be presented as

$$\mathbf{V}_{abc} = \mathbf{r}_s \mathbf{i}_{abc} + p \boldsymbol{\lambda}_{abc} \quad (2.1)$$

$$\mathbf{V}_{qdr} = \mathbf{r}_r \mathbf{i}_{qdr} + p \boldsymbol{\lambda}_{qdr}, \quad (2.2)$$

where

$$\mathbf{f}_{abc} = \begin{bmatrix} f_{as} \\ f_{bs} \\ f_{cs} \end{bmatrix} \quad (2.3)$$

$$\mathbf{f}_{qdr} = \begin{bmatrix} f_{kq1} \\ f_{kq2} \\ f_{fd} \\ f_{kd} \end{bmatrix} \quad (2.4)$$

$$\mathbf{r}_s = \begin{bmatrix} r_s & & \\ & r_s & \\ & & r_s \end{bmatrix} \quad (2.5)$$

$$\mathbf{r}_r = \begin{bmatrix} r_{kq1} & & & \\ & r_{kq2} & & \\ & & r_{fd} & \\ & & & r_{kd} \end{bmatrix}. \quad (2.6)$$

Variables associated with the stator and rotor windings are denoted by the s and r subscripts, respectively. The directions of positive as , bs , and cs axes are the same as positive flux linkages relative to the assumed positive direction of the stator currents. The flux linkage equations can be presented as

$$\begin{bmatrix} \boldsymbol{\lambda}_{abc} \\ \boldsymbol{\lambda}_{qdr} \end{bmatrix} = \begin{bmatrix} \mathbf{L}_s & \mathbf{L}_{sr} \\ \mathbf{L}_{sr}^T & \mathbf{L}_r \end{bmatrix} \begin{bmatrix} \mathbf{i}_{abc} \\ \mathbf{i}_{qdr} \end{bmatrix}, \quad (2.7)$$

where

$$\mathbf{L}_s = \begin{bmatrix} L_{ls} + L_A - L_B \cos 2\theta_r & -\frac{1}{2}L_A - L_B \cos 2(\theta_r - \frac{\pi}{3}) & -\frac{1}{2}L_A - L_B \cos 2(\theta_r + \frac{\pi}{3}) \\ -\frac{1}{2}L_A - L_B \cos 2(\theta_r - \frac{\pi}{3}) & L_{ls} + L_A - L_B \cos 2(\theta_r - \frac{2\pi}{3}) & -\frac{1}{2}L_A - L_B \cos 2(\theta_r + \pi) \\ -\frac{1}{2}L_A - L_B \cos 2(\theta_r + \frac{\pi}{3}) & -\frac{1}{2}L_A - L_B \cos 2(\theta_r + \pi) & L_{ls} + L_A - L_B \cos 2(\theta_r + \frac{2\pi}{3}) \end{bmatrix} \quad (2.8)$$

$$\mathbf{L}_{sr} = \begin{bmatrix} L_{skq1} \cos \theta_r & L_{skq2} \cos \theta_r & L_{sfd} \sin \theta_r & L_{skd} \sin \theta_r \\ L_{skq1} \cos(\theta_r - \frac{2\pi}{3}) & L_{skq2} \cos(\theta_r - \frac{2\pi}{3}) & L_{sfd} \sin(\theta_r - \frac{2\pi}{3}) & L_{skd} \sin(\theta_r - \frac{2\pi}{3}) \\ L_{skq1} \cos(\theta_r + \frac{2\pi}{3}) & L_{skq2} \cos(\theta_r + \frac{2\pi}{3}) & L_{sfd} \sin(\theta_r + \frac{2\pi}{3}) & L_{skd} \sin(\theta_r + \frac{2\pi}{3}) \end{bmatrix} \quad (2.9)$$

$$\mathbf{L}_r = \begin{bmatrix} L_{lkq1} + L_{mkq1} & L_{kq1kq2} & & \\ L_{kq1kq2} & L_{lkq2} + L_{mkq2} & & \\ & & L_{lfd} + L_{mfd} & L_{fdkd} \\ & & L_{fdkd} & L_{lkd} + L_{mkd} \end{bmatrix} \quad (2.10)$$

$$L_A = \left(\frac{N_s}{2}\right)^2 \pi \mu_0 r l \alpha_1 \quad (2.11)$$

$$L_B = \left(\frac{1}{2}\right) \left(\frac{N_s}{2}\right)^2 \pi \mu_0 r l \alpha_2 \quad (2.12)$$

$$L_{mq} = \left(\frac{3}{2}\right) (L_A - L_B) \quad (2.13)$$

$$L_{md} = \left(\frac{3}{2}\right) (L_A + L_B) \quad (2.14)$$

$$L_{skq1} = \left(\frac{2}{3}\right) \left(\frac{N_{kq1}}{N_s}\right) L_{mq} \quad (2.15)$$

$$L_{skq2} = \left(\frac{2}{3}\right) \left(\frac{N_{kq2}}{N_s}\right) L_{mq} \quad (2.16)$$

$$L_{sfd} = \left(\frac{2}{3}\right) \left(\frac{N_{fd}}{N_s}\right) L_{md} \quad (2.17)$$

$$L_{skd} = \left(\frac{2}{3}\right) \left(\frac{N_{kd}}{N_s}\right) L_{md} \quad (2.18)$$

$$L_{mkq1} = \left(\frac{2}{3}\right) \left(\frac{N_{kq1}}{N_s}\right)^2 L_{mq} \quad (2.19)$$

$$L_{mkq2} = \left(\frac{2}{3}\right) \left(\frac{N_{kq2}}{N_s}\right)^2 L_{mq} \quad (2.20)$$

$$L_{mfd} = \left(\frac{2}{3}\right) \left(\frac{N_{fd}}{N_s}\right)^2 L_{md} \quad (2.21)$$

$$L_{mkd} = \left(\frac{2}{3}\right) \left(\frac{N_{kd}}{N_s}\right)^2 L_{md} \quad (2.22)$$

$$L_{kq1kq2} = \left(\frac{N_{kq2}}{N_{kq1}}\right) L_{mkq1} = \left(\frac{N_{kq1}}{N_{kq2}}\right) L_{mkq2} \quad (2.23)$$

$$L_{fdkd} = \left(\frac{N_{kd}}{N_{fd}}\right) L_{mfd} = \left(\frac{N_{fd}}{N_{kd}}\right) L_{mkd} \quad (2.24)$$

In the above equations, μ_0 is the permeability of free space and equals to $4\pi \times 10^{-7} H/m$, r is the radius to the mean of the air gap, l is the axial length of the air gap of the machine, $(\alpha_1 + \alpha_2)^{-1}$ and $(\alpha_1 - \alpha_2)^{-1}$ are the minimum and the maximum air-gap length, respectively. If the rotor is non-salient, i.e. round, $\alpha_2 = 0$ and $L_B = 0$. The subscript l denotes the leakage inductance. The mutual inductances between stator and rotor windings are denoted by the subscripts $skq1$, $skq2$, sfd , skd .

In order to better analyze, the rotor variables are transformed to the stationary reference frame as

$$i'_j = \left(\frac{2}{3}\right) \left(\frac{N_j}{N_s}\right) i_j \quad (2.25)$$

$$v'_j = \left(\frac{N_s}{N_j}\right) v_j \quad (2.26)$$

$$\lambda'_j = \left(\frac{N_s}{N_j}\right) \lambda_j \quad (2.27)$$

$$r'_j = \left(\frac{3}{2}\right) \left(\frac{N_s}{N_j}\right)^2 r_j \quad (2.28)$$

$$L'_{lj} = \left(\frac{3}{2}\right) \left(\frac{N_s}{N_j}\right)^2 L_{lj}, \quad (2.29)$$

where j can represent $kq1$, $kq2$, fd , or kd .

The voltage equations (2.1), (2.2) and the flux linkage equations (2.7) may now be expressed in stationary reference frame as

$$\begin{bmatrix} \mathbf{v}_{abc} \\ \mathbf{v}'_{qdr} \end{bmatrix} = \begin{bmatrix} r_s \mathbf{I}_3 \\ \mathbf{r}'_r \end{bmatrix} \begin{bmatrix} \mathbf{i}_{abc} \\ \mathbf{i}'_{qdr} \end{bmatrix} + \begin{bmatrix} p\boldsymbol{\lambda}_{abc} \\ p\boldsymbol{\lambda}'_{qdr} \end{bmatrix} \quad (2.30)$$

$$\begin{bmatrix} \boldsymbol{\lambda}_{abc} \\ \boldsymbol{\lambda}'_{qdr} \end{bmatrix} = \begin{bmatrix} \mathbf{L}_s & \mathbf{L}'_{sr} \\ \frac{2}{3}\mathbf{L}'_{srT} & \mathbf{L}'_r \end{bmatrix} \begin{bmatrix} \mathbf{i}_{abc} \\ \mathbf{i}'_{qdr} \end{bmatrix}, \quad (2.31)$$

where

$$\mathbf{L}'_{sr} = \begin{bmatrix} L_{mq} \cos \theta_r & L_{mq} \cos \theta_r & L_{md} \sin \theta_r & L_{md} \sin \theta_r \\ L_{mq} \cos(\theta_r - \frac{2\pi}{3}) & L_{mq} \cos(\theta_r - \frac{2\pi}{3}) & L_{md} \sin(\theta_r - \frac{2\pi}{3}) & L_{md} \sin(\theta_r - \frac{2\pi}{3}) \\ L_{mq} \cos(\theta_r + \frac{2\pi}{3}) & L_{mq} \cos(\theta_r + \frac{2\pi}{3}) & L_{md} \sin(\theta_r + \frac{2\pi}{3}) & L_{md} \sin(\theta_r + \frac{2\pi}{3}) \end{bmatrix} \quad (2.32)$$

$$\mathbf{L}'_r = \begin{bmatrix} L'_{lkq1} + L_{mq} & L_{mq} & & \\ L_{mq} & L'_{lkq2} + L_{mq} & & \\ & & L'_{lfd} + L_{md} & L_{md} \\ & & L_{md} & L'_{lkd} + L_{md} \end{bmatrix} \quad (2.33)$$

The energy stored in the coupling field can be presented as

$$\begin{aligned}
W_f &= \left(\frac{1}{2}\right) \begin{bmatrix} \mathbf{i}_{abcs} \\ \mathbf{i}_{qdr} \end{bmatrix}^T \begin{bmatrix} \boldsymbol{\lambda}_{abcs} - \boldsymbol{\lambda}_{labcs} \\ \boldsymbol{\lambda}_{qdr} - \boldsymbol{\lambda}_{lqdr} \end{bmatrix} \\
&= \left(\frac{1}{2}\right) \begin{bmatrix} \mathbf{i}_{abcs} \\ \mathbf{i}_{qdr} \end{bmatrix}^T \begin{bmatrix} \mathbf{L}_s - L_{ls}\mathbf{I}_3 & \mathbf{L}_{sr} \\ \mathbf{L}_{sr}^T & \mathbf{L}_r - \mathbf{L}_{lr} \end{bmatrix} \begin{bmatrix} \mathbf{i}_{abcs} \\ \mathbf{i}_{qdr} \end{bmatrix} \\
&= \left(\frac{1}{2}\right) \mathbf{i}_{abcs}^T (\mathbf{L}_s - L_{ls}\mathbf{I}_3) \mathbf{i}_{abcs} + \mathbf{i}_{abcs}^T \mathbf{L}_{sr} \mathbf{i}_{qdr} + \left(\frac{1}{2}\right) \mathbf{i}_{qdr}^T (\mathbf{L}_r - \mathbf{L}_{lr}) \mathbf{i}_{qdr} \\
&= \left(\frac{1}{2}\right) \mathbf{i}_{abcs}^T (\mathbf{L}_s - L_{ls}\mathbf{I}_3) \mathbf{i}_{abcs} + \mathbf{i}_{abcs}^T \mathbf{L}'_{sr} \mathbf{i}'_{qdr} + \left(\frac{1}{2}\right) \left(\frac{3}{2}\right) \mathbf{i}'_{qdr}{}^T (\mathbf{L}'_r - \mathbf{L}'_{lr}) \mathbf{i}'_{qdr}. \quad (2.34)
\end{aligned}$$

It is assumed that the magnetic system is linear. Thus

$$W_f = W_c = \left(\frac{1}{2}\right) \mathbf{i}_{abcs}^T (\mathbf{L}_s - L_{ls}\mathbf{I}_3) \mathbf{i}_{abcs} + \mathbf{i}_{abcs}^T \mathbf{L}'_{sr} \mathbf{i}'_{qdr} + \left(\frac{1}{2}\right) \left(\frac{3}{2}\right) \mathbf{i}'_{qdr}{}^T (\mathbf{L}'_r - \mathbf{L}'_{lr}) \mathbf{i}'_{qdr} \quad (2.35)$$

where W_c is the co energy.

The electromagnetic torque can be expressed as

$$\begin{aligned}
T_e &= \left(\frac{P}{2}\right) \frac{\partial W_c}{\partial \theta_r} \\
&= \left(\frac{P}{2}\right) \left(\frac{1}{2} \mathbf{i}_{abcs}^T \frac{\partial (\mathbf{L}_s - L_{ls}\mathbf{I}_3)}{\partial \theta_r} \mathbf{i}_{abcs} + \mathbf{i}_{abcs}^T \frac{\partial \mathbf{L}'_{sr}}{\partial \theta_r} \mathbf{i}'_{qdr} \right) \\
&= \left(\frac{P}{2}\right) \left(\frac{1}{2} \mathbf{i}_{abcs}^T \begin{bmatrix} 2L_B \sin 2\theta_r & 2L_B \sin 2(\theta_r - \frac{\pi}{3}) & 2L_B \sin 2(\theta_r + \frac{\pi}{3}) \\ 2L_B \sin 2(\theta_r - \frac{\pi}{3}) & 2L_B \sin 2(\theta_r - \frac{2\pi}{3}) & 2L_B \sin 2(\theta_r + \pi) \\ 2L_B \sin 2(\theta_r + \frac{\pi}{3}) & 2L_B \sin 2(\theta_r + \pi) & 2L_B \sin 2(\theta_r + \frac{2\pi}{3}) \end{bmatrix} \mathbf{i}_{abcs} \right. \\
&\quad \left. + \mathbf{i}_{abcs}^T \begin{bmatrix} -L_{mq} \sin \theta_r & -L_{mq} \sin \theta_r & L_{md} \cos \theta_r & L_{md} \cos \theta_r \\ -L_{mq} \sin(\theta_r - \frac{2\pi}{3}) & -L_{mq} \sin(\theta_r - \frac{2\pi}{3}) & L_{md} \cos(\theta_r - \frac{2\pi}{3}) & L_{md} \cos(\theta_r - \frac{2\pi}{3}) \\ -L_{mq} \sin(\theta_r + \frac{2\pi}{3}) & -L_{mq} \sin(\theta_r + \frac{2\pi}{3}) & L_{md} \cos(\theta_r + \frac{2\pi}{3}) & L_{md} \cos(\theta_r + \frac{2\pi}{3}) \end{bmatrix} \mathbf{i}'_{qdr} \right), \quad (2.36)
\end{aligned}$$

where

$$L_B = \frac{L_{md} - L_{mq}}{3}. \quad (2.37)$$

Because

$$\begin{aligned}
& \begin{bmatrix} \sin 2\theta_r & \sin 2(\theta_r - \frac{\pi}{3}) & \sin 2(\theta_r + \frac{\pi}{3}) \\ \sin 2(\theta_r - \frac{\pi}{3}) & \sin 2(\theta_r - \frac{2\pi}{3}) & \sin 2(\theta_r + \pi) \\ \sin 2(\theta_r + \frac{\pi}{3}) & \sin 2(\theta_r + \pi) & \sin 2(\theta_r + \frac{2\pi}{3}) \end{bmatrix} \\
&= \begin{bmatrix} \sin 2\theta_r & -\frac{1}{2}\sin 2\theta_r - \frac{\sqrt{3}}{2}\cos 2\theta_r & -\frac{1}{2}\sin 2\theta_r + \frac{\sqrt{3}}{2}\cos 2\theta_r \\ -\frac{1}{2}\sin 2\theta_r - \frac{\sqrt{3}}{2}\cos 2\theta_r & -\frac{1}{2}\sin 2\theta_r + \frac{\sqrt{3}}{2}\cos 2\theta_r & \sin 2\theta_r \\ -\frac{1}{2}\sin 2\theta_r + \frac{\sqrt{3}}{2}\cos 2\theta_r & \sin 2\theta_r & -\frac{1}{2}\sin 2\theta_r - \frac{\sqrt{3}}{2}\cos 2\theta_r \end{bmatrix} \\
&= \begin{bmatrix} 1 & -\frac{1}{2} & -\frac{1}{2} \\ -\frac{1}{2} & -\frac{1}{2} & 1 \\ -\frac{1}{2} & 1 & -\frac{1}{2} \end{bmatrix} \sin 2\theta_r + \frac{\sqrt{3}}{2} \begin{bmatrix} 0 & -1 & 1 \\ -1 & 1 & 0 \\ 1 & 0 & -1 \end{bmatrix} \cos 2\theta_r \quad (2.38)
\end{aligned}$$

and

$$\begin{aligned}
& \begin{bmatrix} -L_{mq}\sin\theta_r & -L_{mq}\sin\theta_r & L_{md}\cos\theta_r & L_{md}\cos\theta_r \\ -L_{mq}\sin(\theta_r - \frac{2\pi}{3}) & -L_{mq}\sin(\theta_r - \frac{2\pi}{3}) & L_{md}\cos(\theta_r - \frac{2\pi}{3}) & L_{md}\cos(\theta_r - \frac{2\pi}{3}) \\ -L_{mq}\sin(\theta_r + \frac{2\pi}{3}) & -L_{mq}\sin(\theta_r + \frac{2\pi}{3}) & L_{ms}\cos(\theta_r + \frac{2\pi}{3}) & L_{ms}\cos(\theta_r + \frac{2\pi}{3}) \end{bmatrix} \\
&= \begin{bmatrix} -L_{mq}\sin\theta_r & -L_{mq}\sin\theta_r & L_{md}\cos\theta_r & L_{md}\cos\theta_r \\ L_{mq}(\frac{1}{2}\sin\theta_r + \frac{\sqrt{3}}{2}\cos\theta_r) & L_{mq}(\frac{1}{2}\sin\theta_r + \frac{\sqrt{3}}{2}\cos\theta_r) & L_{md}(\frac{\sqrt{3}}{2}\sin\theta_r - \frac{1}{2}\cos\theta_r) & L_{md}(\frac{\sqrt{3}}{2}\sin\theta_r - \frac{1}{2}\cos\theta_r) \\ L_{mq}(\frac{1}{2}\sin\theta_r - \frac{\sqrt{3}}{2}\cos\theta_r) & L_{mq}(\frac{1}{2}\sin\theta_r - \frac{\sqrt{3}}{2}\cos\theta_r) & L_{md}(-\frac{\sqrt{3}}{2}\sin\theta_r - \frac{1}{2}\cos\theta_r) & L_{md}(-\frac{\sqrt{3}}{2}\sin\theta_r - \frac{1}{2}\cos\theta_r) \end{bmatrix} \\
&= \begin{bmatrix} -L_{mq} & -L_{mq} & 0 & 0 \\ \frac{1}{2}L_{mq} & \frac{1}{2}L_{mq} & \frac{\sqrt{3}}{2}L_{md} & \frac{\sqrt{3}}{2}L_{md} \\ \frac{1}{2}L_{mq} & \frac{1}{2}L_{mq} & -\frac{\sqrt{3}}{2}L_{md} & -\frac{\sqrt{3}}{2}L_{md} \end{bmatrix} \sin\theta_r \begin{bmatrix} 0 & 0 & L_{md} & L_{md} \\ \frac{\sqrt{3}}{2}L_{mq} & \frac{\sqrt{3}}{2}L_{mq} & -\frac{1}{2}L_{md} & -\frac{1}{2}L_{md} \\ -\frac{\sqrt{3}}{2}L_{mq} & -\frac{\sqrt{3}}{2}L_{mq} & -\frac{1}{2}L_{md} & -\frac{1}{2}L_{md} \end{bmatrix} \cos\theta_r. \quad (2.39)
\end{aligned}$$

Equation (2.36) can be transformed into

$$\begin{aligned}
T_e &= \left(\frac{P}{2}\right) \left(\frac{L_{md} - L_{mq}}{3} \left[\left(i_{as}^2 - \frac{1}{2}i_{bs}^2 - \frac{1}{2}i_{cs}^2 - i_{as}i_{bs} - i_{as}i_{cs} + 2i_{bs}i_{cs} \right) \sin 2\theta_r \right. \right. \\
&\quad \left. \left. + \frac{\sqrt{3}}{2} (i_{bs}^2 - i_{cs}^2 - 2i_{as}i_{bs} + 2i_{as}i_{cs}) \cos 2\theta_r \right] \right. \\
&\quad \left. + L_{mq}(i'_{kq1} + i'_{kq2}) \left[\left(i_{as} - \frac{1}{2}i_{bs} - \frac{1}{2}i_{cs} \right) \sin \theta_r - \frac{\sqrt{3}}{2}(i_{bs} - i_{cs}) \cos \theta_r \right] \right. \\
&\quad \left. - L_{md}(i'_{fd} + i'_{kd}) \left[\frac{\sqrt{3}}{2}(i_{bs} - i_{cs}) \sin \theta_r + \left(i_{as} - \frac{1}{2}i_{bs} - \frac{1}{2}i_{cs} \right) \cos \theta_r \right] \right). \quad (2.40)
\end{aligned}$$

2.1.3 Voltage and Flux Linkage Equations in Arbitrary Reference Frame

Variables

The voltage equations (2.1) can be expressed in the arbitrary reference frame as

$$\mathbf{V}_{qd0s} = \mathbf{r}_s \mathbf{i}_{qd0s} + \omega \begin{bmatrix} 0 & 1 & 0 \\ -1 & 0 & 0 \\ 0 & 0 & 0 \end{bmatrix} \boldsymbol{\lambda}_{qd0s} + p \boldsymbol{\lambda}_{qd0s}. \quad (2.41)$$

Because the rotor circuits are unbalanced, there is no benefit to transform the rotor voltage equations into the arbitrary reference frame. Therefore, the rotor voltage equations are expressed only in the rotor reference frame and written as

$$\mathbf{V}'_{qdr} = \mathbf{r}_r \mathbf{i}'_{qdr} + p \boldsymbol{\lambda}'_{qdr}. \quad (2.42)$$

The superscript r denotes variables expressed in the rotor reference frame.

From the flux linkage equations (2.31), the following equations can be derived

$$\begin{bmatrix} \mathbf{K}_s^{-1} \boldsymbol{\lambda}_{qd0s} \\ \boldsymbol{\lambda}'_{qdr} \end{bmatrix} = \begin{bmatrix} \mathbf{L}_s & \mathbf{L}'_{sr} \\ \frac{2}{3} \mathbf{L}'_{srT} & \mathbf{L}'_r \end{bmatrix} \begin{bmatrix} \mathbf{K}_s^{-1} \mathbf{i}_{qd0s} \\ \mathbf{i}'_{qdr} \end{bmatrix} \quad (2.43)$$

$$\begin{bmatrix} \boldsymbol{\lambda}_{qd0s} \\ \boldsymbol{\lambda}'_{qdr} \end{bmatrix} = \begin{bmatrix} \mathbf{K}_s \mathbf{L}_s \mathbf{K}_s^{-1} & \mathbf{K}_s \mathbf{L}'_{sr} \\ \frac{2}{3} \mathbf{L}'_{srT} \mathbf{K}_s^{-1} & \mathbf{L}'_r \end{bmatrix} \begin{bmatrix} \mathbf{i}_{qd0s} \\ \mathbf{i}'_{qdr} \end{bmatrix}, \quad (2.44)$$

where

$$\mathbf{K}_s \mathbf{L}_s \mathbf{K}_s^{-1} = \begin{bmatrix} L_{ls} + \frac{3}{2} L_A - \frac{3}{2} L_B \cos 2(\theta - \theta_r) & -\frac{3}{2} L_B \sin 2(\theta - \theta_r) & 0 \\ -\frac{3}{2} L_B \sin 2(\theta - \theta_r) & L_{ls} + \frac{3}{2} L_A + \frac{3}{2} L_B \cos 2(\theta - \theta_r) & 0 \\ 0 & 0 & L_{ls} \end{bmatrix} \quad (2.45)$$

$$\mathbf{K}_s \mathbf{L}'_{sr} = \begin{bmatrix} L_{mq} \cos(\theta - \theta_r) & L_{mq} \cos(\theta - \theta_r) & -L_{md} \sin(\theta - \theta_r) & -L_{md} \sin(\theta - \theta_r) \\ L_{mq} \sin(\theta - \theta_r) & L_{mq} \sin(\theta - \theta_r) & L_{md} \cos(\theta - \theta_r) & L_{md} \cos(\theta - \theta_r) \\ 0 & 0 & 0 & 0 \end{bmatrix} \quad (2.46)$$

$$\frac{2}{3} \mathbf{L}'_{sr} \mathbf{K}_s^{-1} = (\mathbf{K}_s \mathbf{L}'_{sr})^T = \begin{bmatrix} L_{mq} \cos(\theta - \theta_r) & L_{mq} \sin(\theta - \theta_r) & 0 \\ L_{mq} \cos(\theta - \theta_r) & L_{mq} \sin(\theta - \theta_r) & 0 \\ -L_{md} \sin(\theta - \theta_r) & L_{md} \cos(\theta - \theta_r) & 0 \\ -L_{md} \sin(\theta - \theta_r) & L_{md} \cos(\theta - \theta_r) & 0 \end{bmatrix}. \quad (2.47)$$

2.1.4 Park's Equations and Equivalent Circuits

It is found that mutual inductances of rotating machinery and self-inductances of salient pole machinery stator windings are functions of rotor position (time-varying). These position-varying inductances make the state variable equations time-varying and complicate the machine analysis. In order to eliminate all rotor position-dependent inductances from the state variable equations and simplify electric machine analyses, R. H. Park transformed the stator variables to the rotor reference frame, which is rotating at the electrical angular velocity of the rotor. Then the voltage equations in rotor reference-frame variables, which are also called Park's equations, are obtained. By doing Park's transformation, the corresponding equations don't depend on the rotor position anymore and become time invariant, and the state variables become constant in the steady state. Therefore, the machine analysis is simplified [16]. Since the transformation of the rotor circuit will not simplify the circuit, the rotor circuit won't be transformed. By setting the speed of the arbitrary reference frame ω equal to the rotor speed ω_r , Park's equations can be obtained from the voltage equations (2.41) as

$$\mathbf{V}_{qd0s}^r = \mathbf{r}_s \mathbf{i}_{qd0s}^r + \omega_r \begin{bmatrix} 0 & 1 & 0 \\ -1 & 0 & 0 \\ 0 & 0 & 0 \end{bmatrix} \boldsymbol{\lambda}_{qd0s}^r + p \boldsymbol{\lambda}_{qd0s}^r. \quad (2.48)$$

$$\mathbf{V}_{qdr}^r = \mathbf{r}_r \mathbf{i}_{qdr}^r + p \boldsymbol{\lambda}_{qdr}^r. \quad (2.49)$$

By setting θ equal to θ_r , the flux linkages equations can be expressed in the rotor reference frame as

$$\begin{bmatrix} \lambda_{qd0s}^r \\ \lambda_{qdr}^{\prime r} \end{bmatrix} = \begin{bmatrix} \mathbf{K}_s^r \mathbf{L}_s \mathbf{K}_s^{r-1} & \mathbf{K}_s^r \mathbf{L}'_{sr} \\ \frac{2}{3} \mathbf{L}'_{sr}{}^T \mathbf{K}_s^{r-1} & \mathbf{L}'_r \end{bmatrix} \begin{bmatrix} \mathbf{i}_{qd0s}^r \\ \mathbf{i}'_{qdr} \end{bmatrix}, \quad (2.50)$$

where

$$\mathbf{K}_s^r \mathbf{L}_s \mathbf{K}_s^{r-1} = \begin{bmatrix} L_{ls} + L_{mq} & 0 & 0 \\ 0 & L_{ls} + L_{md} & 0 \\ 0 & 0 & L_{ls} \end{bmatrix} \quad (2.51)$$

$$\mathbf{K}_s^r \mathbf{L}'_{sr} = \begin{bmatrix} L_{mq} & L_{mq} & 0 & 0 \\ 0 & 0 & L_{md} & L_{md} \\ 0 & 0 & 0 & 0 \end{bmatrix} \quad (2.52)$$

$$\frac{2}{3} \mathbf{L}'_{sr}{}^T \mathbf{K}_s^{r-1} = (\mathbf{K}_s^r \mathbf{L}'_{sr})^T = \begin{bmatrix} L_{mq} & 0 & 0 \\ L_{mq} & 0 & 0 \\ 0 & L_{md} & 0 \\ 0 & L_{md} & 0 \end{bmatrix}. \quad (2.53)$$

Park's voltage equations can be expanded as

$$v_{qs}^r = r_s i_{qs}^r + \omega_r \lambda_{ds}^r + p \lambda_{qs}^r \quad (2.54)$$

$$v_{ds}^r = r_s i_{ds}^r - \omega_r \lambda_{qs}^r + p \lambda_{ds}^r \quad (2.55)$$

$$v_{0s} = r_s i_{0s} + p \lambda_{0s} \quad (2.56)$$

$$v'_{kq1} = r'_{kq1} i'_{kq1} + p \lambda'_{kq1} \quad (2.57)$$

$$v'_{kq2} = r'_{kq2} i'_{kq2} + p \lambda'_{kq2} \quad (2.58)$$

$$v'_{fd} = r'_{fd}i'_{fd} + p\lambda'_{fd} \quad (2.59)$$

$$v'_{kd} = r'_{kd}i'_{kd} + p\lambda'_{kd}. \quad (2.60)$$

By substituting Equation (2.51), Equation (2.52), Equation (2.53), and Equation (2.33), into Equation (2.50), the flux linkages equations can be derived as

$$\lambda_{qs}^r = L_{ls}i_{qs}^r + L_{mq}(i_{qs}^r + i'_{kq1} + i'_{kq2}) \quad (2.61)$$

$$\lambda_{ds}^r = L_{ls}i_{ds}^r + L_{md}(i_{ds}^r + i'_{fd} + i'_{kd}) \quad (2.62)$$

$$\lambda_{0s} = L_{ls}i_{0s} \quad (2.63)$$

$$\lambda'_{kq1} = L'_{lkq1}i'_{kq1} + L_{mq}(i_{qs}^r + i'_{kq1} + i'_{kq2}) \quad (2.64)$$

$$\lambda'_{kq2} = L'_{lkq2}i'_{kq2} + L_{mq}(i_{qs}^r + i'_{kq1} + i'_{kq2}) \quad (2.65)$$

$$\lambda'_{fd} = L'_{lfd}i'_{fd} + L_{md}(i_{ds}^r + i'_{fd} + i'_{kd}) \quad (2.66)$$

$$\lambda'_{kd} = L'_{lkd}i'_{kd} + L_{md}(i_{ds}^r + i'_{fd} + i'_{kd}). \quad (2.67)$$

The equivalent circuits suggested by the voltage and flux linkage equations are shown in Figure 2.2.

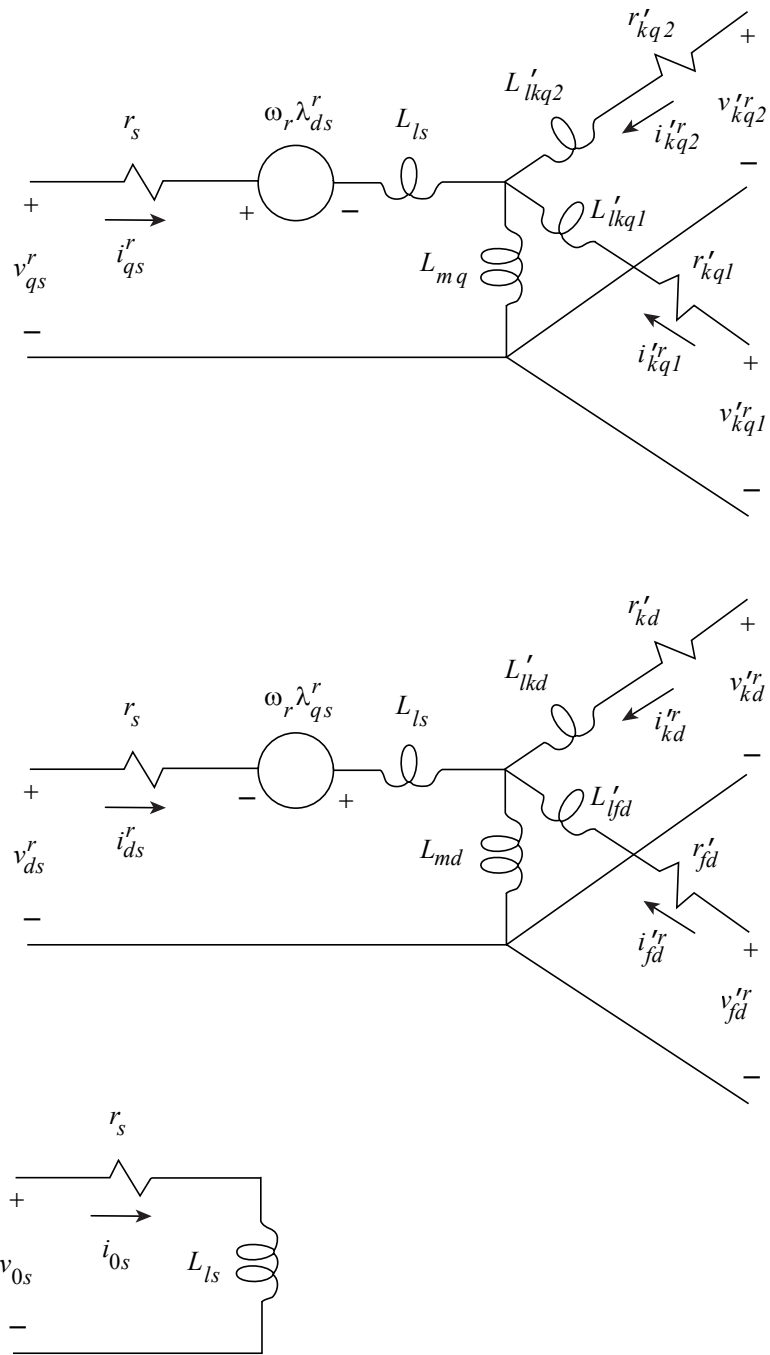


Figure 2.2: Equivalent circuits of a three-phase synchronous machine in the rotor reference frame [1]

Substituting the equations of transformation into Equation (2.36) yields the expression for the electromagnetic torque in rotor reference frame as

$$\begin{aligned}
T_e &= \left(\frac{P}{2}\right) \left(\frac{1}{2} i_{abc}^T \frac{\partial(L_s - L_{ls} I_3)}{\partial \theta_r} i_{abc} + i_{abc}^T \frac{\partial L'_{sr} i'_{qdr}}{\partial \theta_r} \right) \\
&= \left(\frac{P}{2}\right) \left(\frac{1}{2} (K_s^{r-1} i_{qd0s}^r)^T \frac{\partial(L_s - L_{ls} I_3)}{\partial \theta_r} K_s^{r-1} i_{qd0s}^r + (K_s^{r-1} i_{qd0s}^r)^T \frac{\partial L'_{sr} i'_{qdr}}{\partial \theta_r} \right) \\
&= \left(\frac{P}{2}\right) \left(\frac{1}{2} i_{qd0s}^{rT} K_s^{r-1T} \frac{\partial(L_s - L_{ls} I_3)}{\partial \theta_r} K_s^{r-1} i_{qd0s}^r + i_{qd0s}^{rT} K_s^{r-1T} \frac{\partial L'_{sr} i'_{qdr}}{\partial \theta_r} \right), \quad (2.68)
\end{aligned}$$

where

$$\frac{\partial(L_s - L_{ls} I_3)}{\partial \theta_r} = \begin{bmatrix} 2L_B \sin 2\theta_r & 2L_B \sin 2(\theta_r - \frac{\pi}{3}) & 2L_B \sin 2(\theta_r + \frac{\pi}{3}) \\ 2L_B \sin 2(\theta_r - \frac{\pi}{3}) & 2L_B \sin 2(\theta_r - \frac{2\pi}{3}) & 2L_B \sin 2(\theta_r + \pi) \\ 2L_B \sin 2(\theta_r + \frac{\pi}{3}) & 2L_B \sin 2(\theta_r + \pi) & 2L_B \sin 2(\theta_r + \frac{2\pi}{3}) \end{bmatrix} \quad (2.69)$$

$$\frac{\partial L'_{sr}}{\partial \theta_r} = \begin{bmatrix} -L_{mq} \sin \theta_r & -L_{mq} \sin \theta_r & L_{md} \cos \theta_r & L_{md} \cos \theta_r \\ -L_{mq} \sin(\theta_r - \frac{2\pi}{3}) & -L_{mq} \sin(\theta_r - \frac{2\pi}{3}) & L_{md} \cos(\theta_r - \frac{2\pi}{3}) & L_{md} \cos(\theta_r - \frac{2\pi}{3}) \\ -L_{mq} \sin(\theta_r + \frac{2\pi}{3}) & -L_{mq} \sin(\theta_r + \frac{2\pi}{3}) & L_{md} \cos(\theta_r + \frac{2\pi}{3}) & L_{md} \cos(\theta_r + \frac{2\pi}{3}) \end{bmatrix}. \quad (2.70)$$

Thus the torque equation in rotor reference frame, i.e. Equation (2.68), can be reduced to

$$\begin{aligned}
T_e &= \left(\frac{3}{2}\right) \left(\frac{P}{2}\right) \left(L_{md} (i_{ds}^r + i'_{fd} + i'_{kd}) i_{qs}^r - L_{mq} (i_{qs}^r + i'_{kq1} + i'_{kq2}) i_{ds}^r \right) \\
&= \left(\frac{3}{2}\right) \left(\frac{P}{2}\right) (\lambda_{ds}^r r_{qs}^r - \lambda_{qs}^r r_{ds}^r). \quad (2.71)
\end{aligned}$$

The rotor angle is the angular displacement between the rotor and the phase of the terminal voltage. Thus, the rotor angle may be expressed in radian as

$$\delta = \theta_r - \theta_{ev}, \quad (2.72)$$

where θ_{ev} is the electrical angular velocity of the terminal voltage.

The variables in the synchronously rotating reference frame can be transformed into rotor reference frame by using

$$f_{qd0s}^r = {}^e K_s^r f_{qd0s}^e, \quad (2.73)$$

where

$${}^e K_s^r = \begin{bmatrix} \cos \delta & -\sin \delta & 0 \\ \sin \delta & \cos \delta & 0 \\ 0 & 0 & 1 \end{bmatrix} \quad (2.74)$$

The superscript e denotes variables expressed in the the synchronously rotating reference frame.

The electromagnetic torque and the rotor speed may be related as

$$J \frac{d\omega_{rm}}{dt} = T_e - T_l, \quad (2.75)$$

where J is the inertia of the rotor and T_l is the torque load.

If the speed of the synchronously rotating reference frame, i.e. ω_e , is constant, then

$$\begin{aligned} J \frac{d\omega_{rm}}{dt} &= J \left(\frac{2}{P} \right) \frac{d\omega_r}{dt} = J \left(\frac{2}{P} \right) \left(\frac{d\omega_r}{dt} - \frac{d\omega_e}{dt} \right) \\ &= J \left(\frac{2}{P} \right) \left(\frac{d^2\theta_r}{dt^2} - \frac{d^2\theta_{ev}}{dt^2} \right) = J \left(\frac{2}{P} \right) \frac{d^2\delta}{dt^2} = T_e - T_l. \end{aligned} \quad (2.76)$$

2.2 Literature Review

Analytical modeling of synchronous machines is essential for power systems analysis and studies and other important applications such as the study of dc power systems and rotating rectifiers [17–23]. Various models have been proposed from a wide range of perspectives and applications [24–58]. Specifically, many of these models are derived based on Park's transformation [15]. By transformation to the rotor reference frame, the corresponding equations become time invariant, the state variables become constant in the steady state, and the machine analysis is simplified.

Many improvements to synchronous machine models have been offered. Some models have included alternative rotor networks [27, 36, 37, 39, 40, 59, 60], e.g., differential leakage inductance to account for unequal coupling of rotor windings with respect to stator windings. Other models have included magnetizing path saturation in the d -axis [61] or using equivalent isotropic models [45, 62]. The model considered herein, which was proposed in [63], includes arbitrary linear rotor networks and a general magnetizing path saturation representation that includes cross-saturation. This model has been extensively validated in hardware [58, 63–65], and most existing machine models (e.g., the standard qd model, [60, 61, 66]) are special cases of this model.

While the machine model encompasses the mathematical equations used to represent the machine, the formulation is used herein to indicate the particular arrangement of these equations in order to perform time-domain simulation. A given machine model can have multiple formulations that are each better suited for certain types of simulations. One such case is the consideration of machine-rectifier interactions. For such scenarios, the use of traditional voltage-in, current-out (or signal-flow) formulations results in an interface mismatch between the machine and the rectifier, which is more conducive to a circuit representation. This mismatch can be resolved by inserting fictitious circuit elements (e.g., resistors), but this can lead to inaccuracy and to longer simulation run times [67]. Such situations have been studied using phase-domain (PD) circuit formulations [68–73]. In [67], a voltage-behind-reactance (VBR) formulation that achieves direct interfacing between machine models and external networks is derived. This formulation separates the rotor dynamics from the stator circuit representation to achieve better numerical efficiency than PD formulations. In [61], this formulation was extended to models including d -axis saturation. An interesting recent set of formulations have involved constant-parameter VBR formulations, which can greatly decrease run time [74, 75]. These models inherently require additional model approximations and are beyond the scope of the present work.

Multiple formulations of the model considered herein have been derived [63–65]. In

[64], a voltage-in, current-out (qd) formulation is proposed. A stator-only VBR (SVBR) formulation is derived in [63]. A stator and field VBR (SFVBR) formulation was set forth in [65]. Each of these formulations have been successful for certain simulation applications, but these formulations have each entailed complicated derivations with little commonality. Herein, a unified derivation of the model formulations is presented, which avoids the diverse notation, realizations, and transformations found in previous derivations, a field-only VBR (FVBR) formulation that completes the set of formulations for this model is derived, and the relative advantages of each formulation in different simulation applications are demonstrated.

Brushless excitation systems offer higher reliability and require less maintenance than static excitation systems by eliminating brushes, slip rings, circuit breakers, field breakers, and carbon dust [76–78]. These advantages lead to its wide use in large synchronous machines, especially in applications where high reliability is required and maintenance budget is limited [78–80]. Rotating rectifiers are commonly employed in brushless excitation systems, where exciter armature windings and rotating rectifiers are all mounted on the same shaft as main machine field windings [79, 81]. Output voltages of exciters are rectified by rotating rectifiers and fed to main machine field circuits. Because brushless exciters are directly related to main machine field voltages and power system dynamic behavior, accurate and computationally efficient modeling of brushless excitation systems with rotating rectifiers is essential for power electronic simulation and power systems analysis. Specific applications in which accurate and efficient modeling are necessary may involve long simulation times, large numbers of components, and/or repeated simulations with different sets of parameters (e.g., aircraft power systems [82], shipboard power systems [79, 83], and microgrids [84]).

Modeling machine-converter systems has received considerable attention. Although the detailed model of machine-rectifier systems can provide accurate results and design evaluations [85], it is computationally expensive due to repeated switching of the diodes.

Average-value models (AVMs) reduce the modeling complexity and enhance the computational efficiency by “neglecting” or “averaging” the effects of fast switching with respect to the prototypical switching interval [86,87]. In early studies, relationships between ac source variables and rectifier dc variables are derived analytically [88–90]. However, such characteristics are obtained based on idealized ac systems and the assumption that the commutating reactance is constant. In later work, the AVM for converters connected to synchronous machines is proposed [18]. The commutating reactance is set equal to the d -axis subtransient reactance of synchronous machines. Because the commutating reactance should also be related to the q -axis subtransient reactance, the AVM presented in [18] is not accurate. The study in [91] improves the AVM by using a function of both the q - and d -axis subtransient reactances and of the converter firing angle as equivalent commutating reactances. In order to accurately predict the output impedance at higher frequencies, dynamic AVMs are developed in [92]. Analytical derivation methods, which are used in [18, 81, 88–93], are based upon specific switching patterns and have limited utility outside of these operating modes. Also, many of these methods require implicit solutions to nonlinear equations and numerical integration within each time step, which can increase computational cost.

An alternative method for construction of AVMs of rectifiers has been coined the parametric or numerical approach, wherein numerical solutions are adopted in the earlier model development stage to obtain rectifier AVM parameters from detailed simulations [19, 94–97]. In [19], the average behaviors of rectifiers are represented using a set of fixed parameters, which are not able to adaptively evolve according to operating conditions and therefore lead to inaccurate results. An improved AVM with parameters vary dynamically depending on operational conditions is presented in [95]. However, this AVM cannot be directly applied to the rotating rectifier in a brushless excitation system because of some differences between these rectifiers. In particular, the rotating rectifier requires a different reference frame transformation. More importantly, the field winding of the main machine

does not resemble an LC filter (e.g., like seen in [95]); it primarily acts like an RL circuit. This creates a unique interfacing challenge that has not previously been addressed in the literature and is complicated by the saliency of the exciter machine.

Herein, a numerical AVM of the rotating rectifier in a brushless excitation system is proposed. This model averages the periodic switching behavior of the rotating rectifier and integrates these numerical functions with a dynamic model of the exciter machine to allow the nonlinear and dynamic characteristics of the brushless excitation system to be incorporated in simulation models with a traditional voltage-in, current-out formulation of the main machine. This results in accurate and computationally efficient simulations. The proposed model is validated using an experimentally validated machine-exciter system model and the computational efficiency benefits are quantified. It is also shown that the proposed AVM of the brushless excitation system can be combined with a numerical AVM of a stationary rectifier (i.e., [95]) to greatly reduce the computational cost of simulating such a system.

Machine-rectifier systems are generally utilized in the electrical subsystems of electric vehicles, including ships, aircraft, and automobiles, and for the brushless excitation of large synchronous machines. Modeling and simulation of machine-rectifier systems have great significance in the design and analysis of such applications because they can predict the dynamic behavior of each component and the overall system prior to the actual realization in hardware. Accurate and efficient modeling of machine-rectifier systems is particularly beneficial in applications with long run times, iterative simulations with diverse sets of parameters, and/or a high component count, such as microgrids [84], shipboard power systems [79, 83], and aircraft power systems [82].

Different approaches have been proposed to simulate and model machine-rectifier systems. The traditional detailed model of such systems has the ability to predict results accurately and offer design evaluations [85] and can be easily developed utilizing different simulation software packages [98]. However, it requires long simulation times due

to repetitive switching of the diodes. To reduce the computational cost, average-value models (AVMs) have been developed by neglecting the details of each individual switching [86, 87]. Construction methods for AVMs of rectifiers can be generally classified into two categories, i.e., analytical derivation [18, 81, 88–93] and parametric or numerical approaches [19, 94–97, 99]. In analytical derivation methods, analytical relationships between variables on the ac and dc sides are derived. In early studies, such relationships are derived based on strong assumptions (e.g., idealized ac system, constant commutating reactance) [88–90]. In [18], the d -axis subtransient reactance is used to represent the ac-side commutating reactance, which neglects the effect of the q -axis subtransient reactance. In [91], the commutating reactance is determined by a function of the converter firing angle and of both the q - and d -axis subtransient reactances. Subsequently, dynamic AVMs are developed to accurately predict frequency-domain impedance characteristic [92]. Analytical derivation methods are based upon specific operating mode and require significant work to solve nonlinear equations and/or numerical integration, which may significantly reduce the computational efficiency.

As an alternative to analytical derivations, the parametric or numerical approach simplifies the development of AVMs. In parametric or numerical approaches, rectifier AVM parameters are obtained from detailed simulations at an earlier model development stage using numerical solutions [19, 94–97]. The study in [19] uses a set of fixed parameters to model the averaged rectifier behavior. In [95], the AVM is improved by using dynamic parameters which vary depending on operational conditions. The approach in [95] (and subsequently [96, 97]) introduces a low-frequency approximation of the inductor in the dc filter. It was found in [99] that this approximation was not useful for rotating rectifiers in brushless excitation systems because the field winding being fed by the rectifier did not have similar dynamics to the LC dc filters considered in [95] and subsequent work. Therefore, in [99], a low-frequency approximation was introduced to the ac side for such systems. The difference between these two approaches is not really about stationary versus

rotating but about feeding an LC circuit with load versus a field winding that resembles an RL circuit. The parametric or numerical approach has been extended in numerous ways (e.g., ac harmonics and frequency dependency for thyristor-controlled rectifiers are considered in [100]). The fundamental approach is the same, based on numerical averaging of the results of detailed simulations in order to establish a numerical representation of the relationship between the ac and dc variables. However, previous approaches for numerical AVMs introduce low-frequency approximations to avoid improper transfer functions on either the ac or dc side of the rectifier. These approximations can create inaccuracy in highly dynamic situations and can also complicate the interfacing of traditional models of equipment on either the ac or dc side of the rectifier.

Herein, a numerical AVM formulation is proposed that provides a means of directly coupling the AVM with inductive circuitry (e.g., machine on the ac side and dc filter on the dc side). While the proposed formulation uses a model with similar mathematical relationships to existing AVM formulations, it makes direct use of the natural dynamic impedance of the rectifier without the introduction of low-frequency approximations on either the ac or the dc side of the rectifier, a source of significant inaccuracy that is demonstrated in the paper. By using this formulation, direct interface of the AVM that is demonstrated herein is achieved with inductive circuitry on both the ac and dc sides allowing traditional voltage-in, current-out formulations of the circuitry on these sides to be used with the proposed formulation directly. In the proposed alternative formulation, it is not necessary to introduce low-frequency approximations or to invert the voltage-current interfaces on either the ac or dc side for interfacing with an LC circuit with load or a field winding that resembles an RL circuit. Therefore, the proposed formulation is equally valid for the stationary rectifier applications considered in [95–97] and for the rotating rectifier application considered in [99]. Direct interfacing with inductive branches on the ac and dc sides of the rectifier is achieved without introducing low-frequency approximations or algebraic loops. The proposed model is validated against an experimentally validated detailed model

and compared with previous AVM formulations in six cases. The results show that the low-frequency behavior of the system is accurately represented (even in cases in which previous AVM formulations fail to accurately represent this behavior) and that the high computational efficiency associated with existing AVMs is retained. Because the proposed AVM can be directly interfaced with simulation models with traditional voltage-in, current-out formulations of the ac and dc equipment, it can be readily used with existing models of such equipment in commercial simulation toolboxes.

Chapter 3

Unified Model Formulations for Synchronous Machine Model with Saturation and Arbitrary Rotor Network Representation

Numerous models and formulations have been used to study synchronous machines in different applications. Herein, a unified derivation of the various model formulations, which support direct interface to external circuitry in a variety of scenarios, is presented. The work described in this chapter has been published in [16]. A synchronous machine model with magnetizing path saturation including cross-saturation and an arbitrary rotor network representation is considered. This model has been extensively experimentally validated and includes most existing machine models as special cases. Derivations of the standard voltage-in, current-out formulation as well as formulations in which the stator and/or the field windings are represented in a voltage-behind-reactance form are presented in a unified manner, including the derivation of a field-only voltage-behind-reactance formulation. The formulations are compared in a variety of simulation scenarios to show the relative advantages in terms of time steps, run time, and accuracy. It has been demonstrated that selection of the formulation with the most suitable interface for the simulation scenario has better accuracy, fewer time steps, and less run time.

The contributions of this work are: 1) the unified derivation of model formulations for the synchronous machine model, 2) the development of the FVBR formulation, and 3) the demonstration of the relative advantages of the formulations. The remainder of this chapter

is organized as follows. In Section 3.1, the mathematical notation used herein is defined. Section 5.1 details the synchronous machine model in sufficient detail to present the model formulations. The model formulations are included in Section 3.3. Results demonstrating the relative performance of the four synchronous machine formulations are shown and compared in Section 3.4.

3.1 Notation

Matrices and vectors are bold faced. Stator phase variables can be represented in vector form as $\mathbf{f}_{abc} = [f_{as} \ f_{bs} \ f_{cs}]^T$. The symbol f can represent voltage (v), current (i), or flux linkage (λ). Such vector quantities can be transformed into the rotor reference frame using

$$\mathbf{f}_{qd0s} = \mathbf{K}_s(\theta_r)\mathbf{f}_{abc} \quad (3.1)$$

where the transformation matrix [1] is given by

$$\mathbf{K}_s(\theta_r) = \frac{2}{3} \begin{bmatrix} \cos \theta_r & \cos(\theta_r - \frac{2\pi}{3}) & \cos(\theta_r + \frac{2\pi}{3}) \\ \sin \theta_r & \sin(\theta_r - \frac{2\pi}{3}) & \sin(\theta_r + \frac{2\pi}{3}) \\ \frac{1}{2} & \frac{1}{2} & \frac{1}{2} \end{bmatrix}. \quad (3.2)$$

The electrical angular position is given by

$$\theta_r = \frac{P}{2}\theta_{rm}, \quad (3.3)$$

where P is the number of magnetic poles in the machine and θ_{rm} is the mechanical angular position of the machine. Similarly, the electrical angular velocity is given by

$$\omega_r = \frac{P}{2}\omega_{rm}, \quad (3.4)$$

where ω_{rm} is the mechanical angular velocity of the machine. The components of $\mathbf{f}_{qd0s} = [f_{qs} \ f_{ds} \ f_{0s}]^T$ are the q - and d -axis components and the zero-sequence component of the quantity, respectively. When the zero-sequence component is omitted, $\mathbf{f}_{qds} = [f_{qs} \ f_{ds}]^T$.

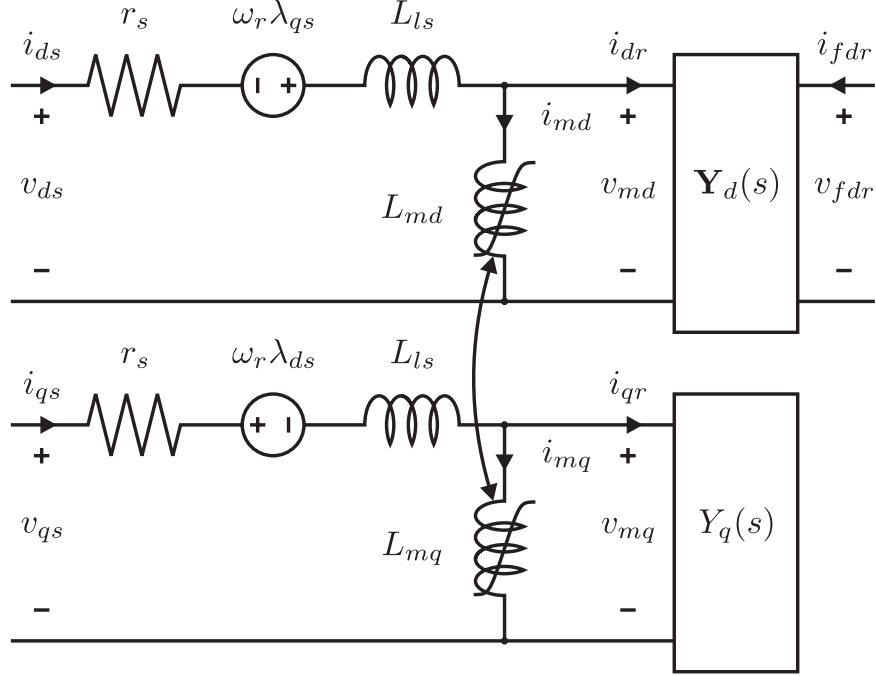


Figure 3.1: Synchronous machine model in rotor reference frame.

The notation $\mathbf{f}_{dq0s} = [f_{ds} \ -f_{qs} \ 0]^T$ is used for speed voltage terms, and $\mathbf{f}_{dqs} = [f_{ds} \ -f_{qs}]^T$ when the zero-sequence component is omitted. Throughout, the operator p denotes differentiation with respect to time.

3.2 Synchronous Machine Model

The synchronous machine model that is considered herein is presented in [58] and shown in Figure 3.1. It can be seen that the model features arbitrary linear networks to represent the rotor circuits and magnetizing path saturation including cross-saturation. The details of the model that are necessary to derive the relevant formulations are presented below.

The stator voltages are given by

$$\mathbf{v}_{abc s} = r_s \mathbf{i}_{abc s} + p \boldsymbol{\lambda}_{abc s}, \quad (3.5)$$

where r_s is the stator resistance. Transforming (3.5) into the rotor reference frame using (5.3) yields

$$\mathbf{v}_{qd0s} = r_s \mathbf{i}_{qd0s} + \omega_r \boldsymbol{\lambda}_{dq0s} + p \boldsymbol{\lambda}_{qd0s}. \quad (3.6)$$

The stator q - and d -axis flux linkages can be divided into a leakage term and a magnetizing term:

$$\boldsymbol{\lambda}_{qds} = L_{ls}\mathbf{i}_{qds} + \boldsymbol{\lambda}_{mqd}, \quad (3.7)$$

where L_{ls} is the stator leakage inductance and $\boldsymbol{\lambda}_{mqd} = [\lambda_{mq} \ \lambda_{md}]^T$ are the magnetizing flux linkages. By Faraday's law, the magnetizing voltages are equal to the time derivatives of the magnetizing flux linkages:

$$\mathbf{v}_{mqd} = p\boldsymbol{\lambda}_{mqd}. \quad (3.8)$$

By substitution of (3.7) into (3.6), the q - and d -axis stator voltages can be expressed as

$$\mathbf{v}_{qds} = r_s\mathbf{i}_{qds} + \omega_r L_{ls}\mathbf{i}_{dqs} + L_{ls}p\mathbf{i}_{qds} + \omega_r\boldsymbol{\lambda}_{mqd} + \mathbf{v}_{mqd}, \quad (3.9)$$

where $\boldsymbol{\lambda}_{mdq} = [\lambda_{md} \ -\lambda_{mq}]^T$. The stator zero-sequence flux linkage can be expressed as

$$\lambda_{0s} = L_{ls}i_{0s}. \quad (3.10)$$

Substitution of (3.10) into (3.6) yields the following expression for the zero sequence stator voltage:

$$v_{0s} = r_s i_{0s} + L_{ls} p i_{0s}. \quad (3.11)$$

The magnetizing currents are related to the magnetizing flux linkages by

$$i_{mq} = \Gamma_{mq}(\hat{\lambda}_m)\lambda_{mq} \quad (3.12)$$

$$i_{md} = \Gamma_{md}(\hat{\lambda}_m)\lambda_{md}, \quad (3.13)$$

where $\Gamma_{mq}(\cdot)$ and $\Gamma_{md}(\cdot)$ are inverse inductance functions related to the representation of saturation,

$$\hat{\lambda}_m = \sqrt{\lambda_{md}^2 + \alpha\lambda_{mq}^2}, \quad (3.14)$$

and α is a saliency-dependent parameter. The relationship between the time derivatives of the magnetizing currents and of the magnetizing flux linkages is given by

$$p\mathbf{i}_{mqd} = \boldsymbol{\Gamma}_{mi}(\boldsymbol{\lambda}_{mqd})p\boldsymbol{\lambda}_{mqd} = \boldsymbol{\Gamma}_{mi}(\boldsymbol{\lambda}_{mqd})\mathbf{v}_{mqd}, \quad (3.15)$$

where the incremental inverse inductance matrix is given by

$$\mathbf{\Gamma}_{mi}(\boldsymbol{\lambda}_{mqd}) = \begin{bmatrix} \frac{d\Gamma_{mq}(\hat{\lambda}_m)}{d\hat{\lambda}_m} \frac{\alpha \lambda_{mq}^2}{\hat{\lambda}_m} + \Gamma_{mq}(\hat{\lambda}_m), & \frac{d\Gamma_{mq}(\hat{\lambda}_m)}{d\hat{\lambda}_m} \frac{\lambda_{mq} \lambda_{md}}{\hat{\lambda}_m} \\ \frac{d\Gamma_{md}(\hat{\lambda}_m)}{d\hat{\lambda}_m} \frac{\alpha \lambda_{mq} \lambda_{md}}{\hat{\lambda}_m}, & \frac{d\Gamma_{md}(\hat{\lambda}_m)}{d\hat{\lambda}_m} \frac{\lambda_{md}^2}{\hat{\lambda}_m} + \Gamma_{md}(\hat{\lambda}_m) \end{bmatrix}. \quad (3.16)$$

Because a lossless coupling field is assumed, a functional constraint of $\Gamma_{md}(\cdot)$ and $\Gamma_{mq}(\cdot)$ is necessary, which renders the incremental inverse inductance matrix symmetric [64].

The rotor circuit is represented in both the q - and d -axes by an arbitrary linear network.

In particular, the d -axis is described by

$$p\mathbf{x}_d = \mathbf{A}_d \mathbf{x}_d + \mathbf{B}_d \begin{bmatrix} v_{md} \\ v_{fdr} \end{bmatrix} \quad (3.17)$$

$$\begin{bmatrix} i_{dr} \\ i_{fdr} \end{bmatrix} = \mathbf{C}_d \mathbf{x}_d, \quad (3.18)$$

and the q -axis is described by

$$p\mathbf{x}_q = \mathbf{A}_q \mathbf{x}_q + \mathbf{b}_q v_{mq} \quad (3.19)$$

$$i_{qr} = \mathbf{c}_q^T \mathbf{x}_q. \quad (3.20)$$

The matrices \mathbf{A}_d , \mathbf{B}_d , and \mathbf{C}_d are a minimal realization of the d -axis rotor network transfer function, denoted by $\mathbf{Y}_d(s)$ in Figure 3.1, and the components of \mathbf{x}_d are state variables associated with this realization. Likewise, the matrix \mathbf{A}_q and the vectors \mathbf{b}_q and \mathbf{c}_q are a minimal realization of the q -axis rotor network transfer function, denoted $Y_q(s)$, and the components of \mathbf{x}_q are its state variables.

It is generally possible by linear transformation to have

$$\mathbf{C}_d = [\mathbf{I}_2 \ \mathbf{0}] \quad (3.21)$$

$$\mathbf{c}_q^T = [1 \ \mathbf{0}^T]. \quad (3.22)$$

A transformation matrix that achieves the form indicated in (3.21) and (3.22) is given by

$$\mathbf{T} = [\mathbf{P} \ \mathbf{N}], \quad (3.23)$$

where $\mathbf{P} = \mathbf{C}^+$ and \mathbf{N} is a matrix formed from columns that span $\text{null}(\mathbf{C})$. This transformation is applied such that the linear system in the new coordinates is described using

$$\tilde{\mathbf{A}} = \mathbf{T}^{-1} \mathbf{A} \mathbf{T} \quad (3.24)$$

$$\tilde{\mathbf{B}} = \mathbf{T}^{-1} \mathbf{A} \quad (3.25)$$

$$\tilde{\mathbf{C}} = \mathbf{C} \mathbf{T} = [\mathbf{I} \ \mathbf{0}]. \quad (3.26)$$

When such a transformation has been applied, it is possible to partition the d -axis linear system as

$$\begin{bmatrix} p i_{dr} \\ p i_{fdr} \\ p \mathbf{x}_{d3} \end{bmatrix} = \begin{bmatrix} a_{d11} & a_{d12} & \mathbf{a}_{d13}^T \\ a_{d21} & a_{d22} & \mathbf{a}_{d23}^T \\ \mathbf{a}_{d31} & \mathbf{a}_{d32} & \mathbf{A}_{d33} \end{bmatrix} \begin{bmatrix} i_{dr} \\ i_{fdr} \\ \mathbf{x}_{d3} \end{bmatrix} + \begin{bmatrix} b_{d11} & b_{d12} \\ b_{d21} & b_{d22} \\ \mathbf{b}_{d31} & \mathbf{b}_{d32} \end{bmatrix} \begin{bmatrix} v_{md} \\ v_{fdr} \end{bmatrix}. \quad (3.27)$$

Likewise, the q -axis system can be partitioned as

$$\begin{bmatrix} p i_{qr} \\ p \mathbf{x}_{q2} \end{bmatrix} = \begin{bmatrix} a_{q11} & \mathbf{a}_{q12}^T \\ \mathbf{a}_{q21} & \mathbf{A}_{q22} \end{bmatrix} \begin{bmatrix} i_{qr} \\ \mathbf{x}_{q2} \end{bmatrix} + \begin{bmatrix} b_{q1} \\ \mathbf{b}_{q2} \end{bmatrix} v_{mq}. \quad (3.28)$$

By Kirchhoff's current law,

$$\mathbf{i}_{qds} = \mathbf{i}_{mqd} + \mathbf{i}_{qdr}. \quad (3.29)$$

Using this current relationship, the magnetizing voltages v_{mqd} can be eliminated from the equations. Differentiating (3.29) with respect to time and substituting (3.15), (3.27) and (3.28) yields

$$\begin{aligned} p \mathbf{i}_{qds} = & \left(\mathbf{\Gamma}_{mi}(\boldsymbol{\lambda}_{mqd}) + \begin{bmatrix} b_{q1} \\ b_{d11} \end{bmatrix} \right) \mathbf{v}_{mqd} \\ & + \begin{bmatrix} a_{q11} \\ a_{d11} \end{bmatrix} \mathbf{i}_{qdr} + \begin{bmatrix} \mathbf{a}_{q12}^T \mathbf{x}_{q2} \\ \mathbf{a}_{d13}^T \mathbf{x}_{d3} \end{bmatrix} \\ & + \begin{bmatrix} 0 \\ a_{d12} \end{bmatrix} i_{fdr} + \begin{bmatrix} 0 \\ b_{d12} \end{bmatrix} v_{fdr}. \end{aligned} \quad (3.30)$$

Substituting (3.30) into (3.9) and solving for \mathbf{v}_{mqd} results in the following:

$$\mathbf{v}_{mqd} = \mathbf{M} \left[\mathbf{v}_{qds} - r_s \mathbf{i}_{qds} - \omega_r L_{ls} \mathbf{i}_{dq0s} - \omega_r \boldsymbol{\lambda}_{mdq} - L_{ls} \left(\begin{bmatrix} a_{q11} & \\ & a_{d11} \end{bmatrix} \mathbf{i}_{qdr} + \begin{bmatrix} \mathbf{a}_{q12}^T \mathbf{x}_{q2} \\ \mathbf{a}_{d13}^T \mathbf{x}_{d3} \end{bmatrix} + \begin{bmatrix} 0 \\ a_{d12} \end{bmatrix} i_{fdr} + \begin{bmatrix} 0 \\ b_{d12} \end{bmatrix} v_{fdr} \right) \right], \quad (3.31)$$

where

$$\mathbf{M} = \left[\mathbf{I}_2 + L_{ls} \left(\boldsymbol{\Gamma}_{mi}(\boldsymbol{\lambda}_{mqd}) + \begin{bmatrix} b_{q1} & \\ & b_{d11} \end{bmatrix} \right) \right]^{-1}. \quad (3.32)$$

The set of voltage equations can be rearranged into forms suitable for each of the model formulations. In particular, certain voltage equations must be represented in a form suitable for circuit representation for each formulation. For the SVBR formulation, solving (3.29) for \mathbf{i}_{qdr} , substituting into (3.30), solving for \mathbf{v}_{mqd} , substituting into (3.9), and combining with (3.11) yields

$$\mathbf{v}_{qd0s} = r_s \mathbf{i}_{qd0s} + \omega_r L_{ls} \mathbf{i}_{dq0s} + L_{ls} p \mathbf{i}_{qd0s} + \hat{\mathbf{R}}_m \mathbf{i}_{qd0s} + \hat{\mathbf{L}}_m p \mathbf{i}_{qd0s} + \mathbf{e}_{qd0s}. \quad (3.33)$$

The matrices and vector in (3.33) are

$$\hat{\mathbf{R}}_m = \begin{bmatrix} \mathbf{L}_{mi} \begin{bmatrix} a_q \\ a_d \end{bmatrix} \\ 0 \end{bmatrix} \quad (3.34)$$

$$\hat{\mathbf{L}}_m = \begin{bmatrix} \mathbf{L}_{mi} \\ 0 \end{bmatrix} \quad (3.35)$$

$$\mathbf{e}_{qd0s} = \begin{bmatrix} \mathbf{e}_{qds} \\ 0 \end{bmatrix}, \quad (3.36)$$

where $a_q = -a_{q11}$, $a_d = -a_{d11}$, and

$$\begin{aligned} \mathbf{L}_{mi} &= \left(\mathbf{\Gamma}_{mi}(\boldsymbol{\lambda}_{mqd}) + \begin{bmatrix} b_{q1} & \\ & b_{d11} \end{bmatrix} \right)^{-1} \\ &= \begin{bmatrix} L_{mqq} & L_{mqd} \\ L_{mqd} & L_{mdd} \end{bmatrix} \end{aligned} \quad (3.37)$$

$$\begin{aligned} \mathbf{e}_{qds} &= \omega_r \boldsymbol{\lambda}_{mdq} \\ &+ \mathbf{L}_{mi} \left(\begin{bmatrix} a_{q11} & \\ & a_{d11} \end{bmatrix} \mathbf{i}_{mqd} - \begin{bmatrix} \mathbf{a}_{q12}^T \mathbf{x}_{q2} \\ \mathbf{a}_{d13}^T \mathbf{x}_{d3} \end{bmatrix} - \begin{bmatrix} 0 \\ a_{d12} \end{bmatrix} i_{fdr} - \begin{bmatrix} 0 \\ b_{d12} \end{bmatrix} v_{fdr} \right). \end{aligned} \quad (3.38)$$

Transforming (3.33) into phase variables yields

$$\mathbf{v}_{abcs} = \mathbf{R}\mathbf{i}_{abcs} + \mathbf{L}p\mathbf{i}_{abcs} + \mathbf{e}_{abcs}. \quad (3.39)$$

The matrices and vector in (3.39) are

$$\mathbf{R} = r_s \mathbf{I}_3 + \mathbf{R}_m \quad (3.40)$$

$$\mathbf{L} = L_{ls} \mathbf{I}_3 + \mathbf{L}_m \quad (3.41)$$

$$\mathbf{e}_{abcs} = \mathbf{K}_s^{-1} \mathbf{e}_{qd0s}, \quad (3.42)$$

where

$$\begin{aligned}
\mathbf{R}_m = & R_a \mathbf{M}_1 + (\sqrt{3}/2)(\omega_r L_a - R_d) \mathbf{M}_2 \\
& + \begin{bmatrix} R_1(\theta_r) & R_1(\theta_r - \pi/3) & R_1(\theta_r + \pi/3) \\ R_1(\theta_r - \pi/3) & R_1(\theta_r + \pi/3) & R_1(\theta_r) \\ R_1(\theta_r + \pi/3) & R_1(\theta_r) & R_1(\theta_r - \pi/3) \end{bmatrix} \\
& + \omega_r \begin{bmatrix} L_2(\theta_r) & L_2(\theta_r - \pi/3) & L_2(\theta_r + \pi/3) \\ L_2(\theta_r - \pi/3) & L_2(\theta_r + \pi/3) & L_2(\theta_r) \\ L_2(\theta_r + \pi/3) & L_2(\theta_r) & L_2(\theta_r - \pi/3) \end{bmatrix} \tag{3.43}
\end{aligned}$$

$$\mathbf{L}_m = L_a \mathbf{M}_1 + \begin{bmatrix} L_1(\theta_r) & L_1(\theta_r - \pi/3) & L_1(\theta_r + \pi/3) \\ L_1(\theta_r - \pi/3) & L_1(\theta_r + \pi/3) & L_1(\theta_r) \\ L_1(\theta_r + \pi/3) & L_1(\theta_r) & L_1(\theta_r - \pi/3) \end{bmatrix} \tag{3.44}$$

$$L_a = (L_{mqq} + L_{mdd})/3 \quad (3.45)$$

$$L_b = (L_{mdd} - L_{mqq})/3 \quad (3.46)$$

$$L_c = 2L_{mqd}/3 \quad (3.47)$$

$$R_a = (a_q L_{mqq} + a_d L_{mdd})/3 \quad (3.48)$$

$$R_b = (a_d L_{mdd} - a_q L_{mqq})/3 \quad (3.49)$$

$$R_c = (a_q + a_d)L_{mqd}/3 \quad (3.50)$$

$$R_d = (a_d - a_q)L_{mqd}/3 \quad (3.51)$$

$$L_1(\phi) = -L_b \cos(2\phi) + L_c \sin(2\phi) \quad (3.52)$$

$$L_2(\phi) = L_1(\phi + \pi/4) \quad (3.53)$$

$$R_1(\phi) = -R_b \cos(2\phi) + R_c \sin(2\phi) \quad (3.54)$$

$$\mathbf{M}_1 = \begin{bmatrix} 1 & -1/2 & -1/2 \\ -1/2 & 1 & -1/2 \\ -1/2 & -1/2 & 1 \end{bmatrix} \quad (3.55)$$

$$\mathbf{M}_2 = \begin{bmatrix} 0 & 1 & -1 \\ -1 & 0 & 1 \\ 1 & -1 & 0 \end{bmatrix}. \quad (3.56)$$

For the FVBR formulation, substituting (3.31) into (3.27) and solving for v_{fdr} results in the following:

$$v_{fdr} = Ri_{fdr} + Lpi_{fdr} + e_{fdr}. \quad (3.57)$$

The scalars in (3.57) are

$$R = r_{sfdr} + \sigma a'_f L_{ls} M'_{dd} \quad (3.58)$$

$$L = L_{sfdr} + \chi \sigma L_{ls} M'_{dd} \quad (3.59)$$

$$\begin{aligned} e_{fdr} = & \sigma [M'_{qd} \ M'_{dd}] \left[\mathbf{v}_{qds} - r_s \mathbf{i}_{qds} - \boldsymbol{\omega}_r L_{ls} \mathbf{i}_{dq_s} - \boldsymbol{\omega}_r \boldsymbol{\lambda}_{mdq} \right. \\ & \left. - L_{ls} \left(\begin{bmatrix} a_{q11} & \\ & a_{d11} \end{bmatrix} \mathbf{i}_{qdr} + \begin{bmatrix} \mathbf{a}_{q12}^T \mathbf{x}_{q2} \\ \mathbf{a}_{d13}^T \mathbf{x}_{d3} \end{bmatrix} \right) \right] \\ & - (L_{sfdr} + \chi \sigma L_{ls} M'_{dd}) (a_{d21} \mathbf{i}_{dr} + \mathbf{a}_{d23}^T \mathbf{x}_{d3}), \end{aligned} \quad (3.60)$$

where

$$\begin{aligned} \mathbf{M}' &= \left[\mathbf{I}_2 + L_{ls} \left(\boldsymbol{\Gamma}_{mi}(\boldsymbol{\lambda}_{mqd}) + \begin{bmatrix} b_{q1} & \\ & b_{d11} - \chi \sigma b_{d22} \end{bmatrix} \right) \right]^{-1} \\ &= \begin{bmatrix} M'_{qq} & M'_{qd} \\ M'_{qd} & M'_{dd} \end{bmatrix} \end{aligned} \quad (3.61)$$

$$\chi = -b_{d12}/b_{d22} \quad (3.62)$$

$$\sigma = -b_{d21}/b_{d22} \quad (3.63)$$

$$a'_f = -a_{d12} - \chi a_{d22} \quad (3.64)$$

$$r_{sfdr} = -a_{d22}/b_{d22} \quad (3.65)$$

$$L_{sfdr} = 1/b_{d22}. \quad (3.66)$$

For the SFVBR formulation, substituting (3.31) into (3.9) and (3.27), solving for \mathbf{v}_{qds}

and v_{fdr} , and combining with (3.11) yields:

$$\begin{aligned}
 \begin{bmatrix} \mathbf{v}_{qd0s} \\ v_{fdr} \end{bmatrix} &= \mathbf{R}'_s \begin{bmatrix} \mathbf{i}_{qd0s} \\ i_{fdr} \end{bmatrix} + \begin{bmatrix} \boldsymbol{\omega}_r L_{ls} \mathbf{i}_{dq0s} \\ 0 \end{bmatrix} \\
 &\quad + \mathbf{L}'_s \begin{bmatrix} p\mathbf{i}_{qd0s} \\ pi_{fdr} \end{bmatrix} + \hat{\mathbf{R}}'_m \begin{bmatrix} \mathbf{i}_{qd0s} \\ i_{fdr} \end{bmatrix} \\
 &\quad + \hat{\mathbf{L}}'_m \begin{bmatrix} p\mathbf{i}_{qd0s} \\ pi_{fdr} \end{bmatrix} + \begin{bmatrix} \mathbf{e}'_{qd0s} \\ e'_{fdr} \end{bmatrix}. \quad (3.67)
 \end{aligned}$$

The matrices, vector, and scalar in (3.67) are

$$\mathbf{R}'_s = \begin{bmatrix} r_s \mathbf{I}_3 & \\ & r_{sfdr} \end{bmatrix} \quad (3.68)$$

$$\mathbf{L}'_s = \begin{bmatrix} L_{ls} \mathbf{I}_3 & \\ & L_{sfdr} \end{bmatrix} \quad (3.69)$$

$$\hat{\mathbf{R}}'_m = \begin{bmatrix} 0 & 0 & 0 & 0 \\ 0 & 0 & 0 & 0 \\ 0 & 0 & 0 & 0 \\ 0 & r_{mfdr} & 0 & 0 \end{bmatrix} + \begin{bmatrix} -a_q L'_{mqq} & -a_d L'_{mqd} & 0 & -a_f L'_{mqd} \\ -a_q L'_{mqd} & -a_d L'_{mdd} & 0 & -a_f L'_{mdd} \\ 0 & 0 & 0 & 0 \\ \sigma a_q L'_{mqd} & \sigma a_d L'_{mdd} & 0 & \sigma a_f L'_{mdd} \end{bmatrix} \quad (3.70)$$

$$\hat{\mathbf{L}}'_m = \begin{bmatrix} L'_{mqq} & L'_{mqd} & 0 & -\chi L'_{mqd} \\ L'_{mqd} & L'_{mdd} & 0 & -\chi L'_{mdd} \\ 0 & 0 & 0 & 0 \\ -\sigma L'_{mqd} & -\sigma L'_{mdd} & 0 & \chi \sigma L'_{mdd} \end{bmatrix} \quad (3.71)$$

$$\mathbf{e}'_{qd0s} = \mathbf{L}'_{mi} \begin{bmatrix} a_{q11} & \\ & a_{d11} \end{bmatrix} \mathbf{i}_{mqd} - \begin{bmatrix} \mathbf{a}_{q12}^T \mathbf{x}_{q2} \\ \mathbf{a}_{d13}^T \mathbf{x}_{d3} \end{bmatrix} \\ - \chi \begin{bmatrix} L'_{mqd} \\ L'_{mdd} \end{bmatrix} (\mathbf{a}_{d23}^T \mathbf{x}_{d3} - a_{d21} i_{md}) + \omega_r \boldsymbol{\lambda}_{mdq} \quad (3.72)$$

$$\mathbf{e}'_{fdr} = \sigma \begin{bmatrix} L'_{mqd} & L'_{mdd} \end{bmatrix} \left(\begin{bmatrix} a_{q11} & \\ & a_{d11} \end{bmatrix} \mathbf{i}_{mqd} - \begin{bmatrix} \mathbf{a}_{q12}^T \mathbf{x}_{q2} \\ \mathbf{a}_{d13}^T \mathbf{x}_{d3} \end{bmatrix} \right) \\ - (L_{sfdr} + \chi \sigma L'_{mdd}) (\mathbf{a}_{d23}^T \mathbf{x}_{d3} - a_{d21} i_{md}), \quad (3.73)$$

where

$$\begin{aligned}\mathbf{L}'_{mi} &= \left(\mathbf{\Gamma}_{mi}(\boldsymbol{\lambda}_{mqd}) + \begin{bmatrix} b_{q1} & \\ & b_{d11} - b_{d12}b_{d21}/b_{d22} \end{bmatrix} \right)^{-1} \\ &= \begin{bmatrix} L'_{mqq} & L'_{mqd} \\ L'_{mqd} & L'_{mdd} \end{bmatrix}\end{aligned}\quad (3.74)$$

$$a'_d = -a_{d11} - \chi a_{d21} \quad (3.75)$$

$$r_{mfdr} = -a_{d21}/b_{d22}. \quad (3.76)$$

Transforming (3.67) into phase variables yields

$$\begin{bmatrix} \mathbf{v}_{abc} \\ v_{fdr} \end{bmatrix} = \mathbf{R}' \begin{bmatrix} \mathbf{i}_{abc} \\ i_{fdr} \end{bmatrix} + \mathbf{L}' \begin{bmatrix} p\mathbf{i}_{abc} \\ pi_{fdr} \end{bmatrix} + \begin{bmatrix} \mathbf{e}'_{abc} \\ e'_{fdr} \end{bmatrix}. \quad (3.77)$$

The matrices and vector in (3.77) are

$$\mathbf{R}' = \mathbf{R}'_s + \mathbf{R}'_m \quad (3.78)$$

$$\mathbf{L}' = \mathbf{L}'_s + \mathbf{L}'_m \quad (3.79)$$

$$\mathbf{e}'_{abc} = \mathbf{K}_s^{-1} \mathbf{e}'_{qd0s}, \quad (3.80)$$

where \mathbf{R}'_m and \mathbf{L}'_m are defined in (3.81) and (3.82).

$$\begin{aligned}
\mathbf{R}'_m = & \begin{bmatrix} R'_a \mathbf{M}_1 \\ \sigma a'_f L'_{mdd} \end{bmatrix} + (\sqrt{3}/2)(\omega_r L'_a - R'_d) \begin{bmatrix} \mathbf{M}_2 \\ 0 \end{bmatrix} \\
& + \begin{bmatrix} R'_1(\theta_r) & R'_1(\theta_r - \pi/3) & R'_1(\theta_r + \pi/3) & R'_2(\theta_r) \\ R'_1(\theta_r - \pi/3) & R'_1(\theta_r + \pi/3) & R'_1(\theta_r) & R'_2(\theta_r - 2\pi/3) \\ R'_1(\theta_r + \pi/3) & R'_1(\theta_r) & R'_1(\theta_r - \pi/3) & R'_2(\theta_r + 2\pi/3) \\ R'_3(\theta_r) & R'_3(\theta_r - 2\pi/3) & R'_3(\theta_r + 2\pi/3) & 0 \end{bmatrix} \\
& + \omega_r \begin{bmatrix} L'_2(\theta_r) & L'_2(\theta_r - \pi/3) & L'_2(\theta_r + \pi/3) & 0 \\ L'_2(\theta_r - \pi/3) & L'_2(\theta_r + \pi/3) & L'_2(\theta_r) & 0 \\ L'_2(\theta_r + \pi/3) & L'_2(\theta_r) & L'_2(\theta_r - \pi/3) & 0 \\ L'_4(\theta_r) & L'_4(\theta_r - 2\pi/3) & L'_4(\theta_r + 2\pi/3) & 0 \end{bmatrix} \tag{3.81}
\end{aligned}$$

$$\begin{aligned}
\mathbf{L}'_m = & \begin{bmatrix} L'_a \mathbf{M}_1 \\ \chi \sigma L'_{mdd} \end{bmatrix} \\
& + \begin{bmatrix} L'_1(\theta_r) & L'_1(\theta_r - \pi/3) & L'_1(\theta_r + \pi/3) & L'_5(\theta_r) \\ L'_1(\theta_r - \pi/3) & L'_1(\theta_r + \pi/3) & L'_1(\theta_r) & L'_5(\theta_r - 2\pi/3) \\ L'_1(\theta_r + \pi/3) & L'_1(\theta_r) & L'_1(\theta_r - \pi/3) & L'_5(\theta_r + 2\pi/3) \\ L'_3(\theta_r) & L'_3(\theta_r - 2\pi/3) & L'_3(\theta_r + 2\pi/3) & 0 \end{bmatrix} \tag{3.82}
\end{aligned}$$

$$L'_a = (L'_{mqq} + L'_{mdd})/3 \quad (3.83)$$

$$L'_b = (L'_{mdd} - L'_{mqq})/3 \quad (3.84)$$

$$L'_c = 2L'_{mqd}/3 \quad (3.85)$$

$$R'_a = (a_q L'_{mqq} + a'_d L'_{mdd})/3 \quad (3.86)$$

$$R'_b = (a'_d L'_{mdd} - a_q L'_{mqq})/3 \quad (3.87)$$

$$R'_c = (a_q + a'_d) L'_{mqd}/3 \quad (3.88)$$

$$R'_d = (a'_d - a_q) L'_{mqd}/3 \quad (3.89)$$

$$L'_1(\phi) = -L'_b \cos(2\phi) + L'_c \sin(2\phi) \quad (3.90)$$

$$L'_2(\phi) = L'_1(\phi + \pi/4) \quad (3.91)$$

$$L_x(\phi) = L'_{mqd} \cos(\phi) + L'_{mdd} \sin(\phi) \quad (3.92)$$

$$L'_3(\phi) = 2\sigma L_x(\phi)/3 \quad (3.93)$$

$$L'_4(\phi) = L'_3(\phi + \pi/2) \quad (3.94)$$

$$L'_5(\phi) = \chi L_x(\phi) \quad (3.95)$$

$$R'_1(\phi) = -R'_b \cos(2\phi) + R'_c \sin(2\phi) \quad (3.96)$$

$$R'_2(\phi) = a'_f L_x(\phi) \quad (3.97)$$

$$R'_3(\phi) = 2/3(\sigma(a_q L'_{mqd} \cos(\phi) + a'_d L'_{mdd} \sin(\phi))) + r_{mfd} \sin(\phi). \quad (3.98)$$

3.3 Model Formulations

Each of the formulations described below has a similar structure. For each formulation there is a set of state variables, which always includes the magnetizing flux linkages λ_{mqd} . The rotor mechanical speed ω_{rm} and (if necessary) the rotor mechanical position θ_{rm} are inputs to the model. Each formulation can be thought to operate in a subset of the following six stages. In the first stage, the initial calculations listed below are performed for each of the formulations.

1. Calculate ω_r from (3.4) and (if necessary) θ_r from (3.3).
2. Calculate $\hat{\lambda}_m$ from (3.14) and $\Gamma_{mq}(\hat{\lambda}_m)$ and $\Gamma_{md}(\hat{\lambda}_m)$ from their definitions.
3. Calculate Γ_{mi} from (3.16).
4. Calculate \mathbf{i}_{mqd} from (3.12) and (3.13).

Depending on the formulation, currents are determined based on the state variables of the model and output to external signal-flow models of connected circuitry in the second stage. In the third stage, the external signal-flow models calculate voltages for such formulations. Depending on the formulation, the parameters of a VBR representation are calculated in the fourth stage. In the fifth stage, the VBR circuit model is combined with circuit models of connected circuitry, and a circuit solver is used to calculate voltages and currents for such formulations. In the final stage, the time derivatives of the state variables are calculated. In this stage, the torque developed by the synchronous machine is calculated by [63]

$$T_e = \frac{3P}{2} \frac{1}{2} (i_{qs}\lambda_{md} - i_{ds}\lambda_{mq}), \quad (3.99)$$

which is used by the prime mover model to calculate the time derivatives of the mechanical state variables (ω_{rm} and (if necessary) θ_{rm}).

3.3.1 *qd* Formulation

For a *qd* formulation, the state variables of the model are λ_{mqd} , \mathbf{i}_{qdr} , i_{fdr} , \mathbf{x}_{d3} , and \mathbf{x}_{q2} . If the zero-sequence components are to be represented, i_{0s} is an additional state variable of the model. Such a formulation requires the initial calculation, current calculation, signal-flow interface, and derivative calculation stages shown in Figure 3.2. In the current calculation stage, the stator currents \mathbf{i}_{qds} (or \mathbf{i}_{qd0s} if the zero-sequence components are to be represented or \mathbf{i}_{abcs} if phase currents are to be used) and field current i_{fdr} are determined. The steps required in this stage are listed below.

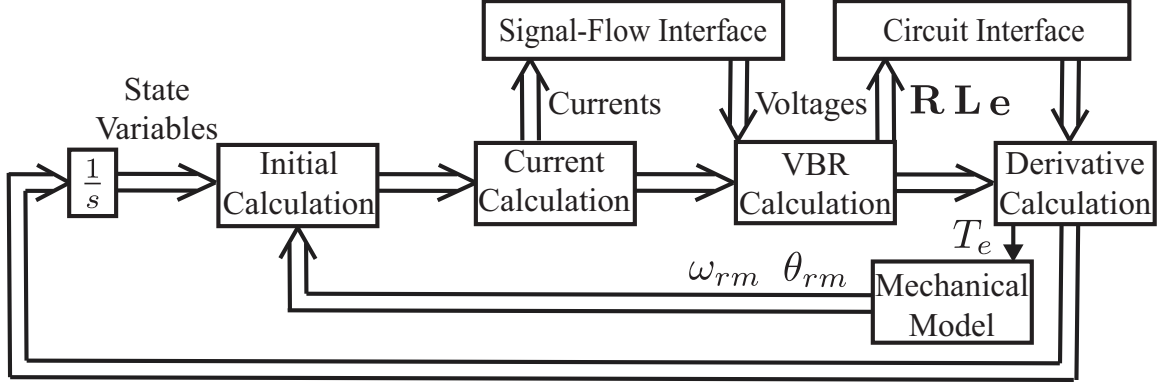


Figure 3.2: Summary of model formulations. The integrators associated with the mechanical state variables are represented within the Mechanical Model block.

1. Calculate \mathbf{i}_{qds} from (3.29). If the zero-sequence components are represented, i_{0s} is a state variable.
2. If necessary, transform \mathbf{i}_{qd0s} to \mathbf{i}_{abcs} .
3. The field current i_{fdr} is a state variable.

In the signal-flow interface stage, an external signal-flow model of circuitry connected to the stator and field is used to calculate the stator voltages \mathbf{v}_{qds} (or \mathbf{v}_{qd0s} or \mathbf{v}_{abcs}) and the field voltage v_{fdr} .

In the derivative calculation stage, the time derivatives of the state variables are calculated. The steps required in this stage are listed below.

1. If necessary, transform \mathbf{v}_{abcs} to \mathbf{v}_{qd0s} .
2. Calculate \mathbf{v}_{mqd} from (3.31).
3. Calculate $p\boldsymbol{\lambda}_{mqd}$ from (3.8).
4. Calculate $p\mathbf{i}_{qdr}$, $p i_{fdr}$, $p\mathbf{x}_{d3}$, and $p\mathbf{x}_{q2}$ from (3.27) and (3.28). If the zero-sequence components are represented, calculate $p i_{0s}$ from (3.11).

3.3.2 SVBR Formulation

For an SVBR formulation, the state variables of the model are λ_{mqd} , i_{fdr} , \mathbf{x}_{d3} , and \mathbf{x}_{q2} . Such a formulation requires the initial calculation, current calculation, signal-flow interface, VBR calculation, circuit interface, and derivative calculation stages shown in Figure 3.2. In the current calculation stage, the field current i_{fdr} is a state variable.

In the signal-flow interface stage, an external signal-flow model of circuitry connected to the field is used to calculate the field voltage v_{fdr} .

In the VBR calculation stage, the stator circuit parameters \mathbf{R} , \mathbf{L} , and \mathbf{e}_{abcs} are calculated from (3.40)–(3.42).

In the circuit interface stage, the stator VBR circuit model is combined with circuit models of circuitry connected to the stator, and a circuit solver is used to calculate \mathbf{v}_{abcs} and \mathbf{i}_{abcs} .

In the derivative calculation stage, the time derivatives of the state variables are calculated. The steps required in this stage are listed below.

1. Transform \mathbf{v}_{abcs} and \mathbf{i}_{abcs} to \mathbf{v}_{qd0s} and \mathbf{i}_{qd0s} , respectively.
2. Calculate \mathbf{i}_{qdr} from (3.29).
3. Calculate \mathbf{v}_{mqd} from (3.31).
4. Calculate $p\lambda_{mqd}$ from (3.8).
5. Calculate pi_{fdr} , $p\mathbf{x}_{d3}$, and $p\mathbf{x}_{q2}$ from (3.27) and (3.28).

3.3.3 FVBR Formulation

For an FVBR formulation, the state variables of the model are λ_{mqd} , \mathbf{i}_{qdr} , \mathbf{x}_{d3} and \mathbf{x}_{q2} . If the zero-sequence components are to be represented, i_{0s} is an additional state variable of the model. Such a formulation requires the initial calculation, current calculation, signal-flow interface, VBR calculation, circuit interface, and derivative calculation stages shown

in Figure 3.2. In the current calculation stage, the stator currents \mathbf{i}_{qds} (or \mathbf{i}_{qd0s} if the zero-sequence components are to be represented or \mathbf{i}_{abcs} if phase currents are to be used) are determined. The steps required in this stage are listed below.

1. Calculate \mathbf{i}_{qds} from (3.29). If the zero-sequence components are represented, i_{0s} is a state variable.
2. If necessary, transform \mathbf{i}_{qd0s} to \mathbf{i}_{abcs} .

In the signal-flow interface stage, an external signal-flow model of circuitry connected to the stator is used to calculate the stator voltages \mathbf{v}_{qds} (or \mathbf{v}_{qd0s} or \mathbf{v}_{abcs}). If necessary, \mathbf{v}_{abcs} is transformed to \mathbf{v}_{qd0s} .

In the VBR calculation stage, the field circuit parameters R , L , and e_{fdr} are calculated from (3.58)–(3.60).

In the circuit interface stage, the field VBR circuit model is combined with a circuit model of circuitry connected to the field, and a circuit solver is used to calculate v_{fdr} and i_{fdr} .

In the derivative calculation stage, the time derivatives of the state variables are calculated. The steps required in this stage are listed below.

1. Calculate \mathbf{v}_{mqd} from (3.31).
2. Calculate $p\boldsymbol{\lambda}_{mqd}$ from (3.8).
3. Calculate $p\mathbf{i}_{qdr}$, $p\mathbf{x}_{d3}$, and $p\mathbf{x}_{q2}$ from (3.27) and (3.28). If the zero-sequence components are represented, calculate pi_{0s} from (3.11).

3.3.4 SFVBR Formulation

For an SFVBR formulation, the state variables of the model are $\boldsymbol{\lambda}_{mqd}$, \mathbf{x}_{d3} , and \mathbf{x}_{q2} . Such a formulation requires the initial calculation, the VBR calculation, circuit interface, and

derivative calculation stages shown in Figure 3.2. In the VBR calculation stage, the circuit parameters \mathbf{R}' , \mathbf{L}' , \mathbf{e}'_{abc} and e'_{fdr} can be calculated from (3.78)–(3.80) and (3.73).

In the circuit interface stage, the circuit parameters are combined with circuit representations of the interconnected equipment. This system is solved using a circuit solver to calculate \mathbf{v}_{abc} , \mathbf{i}_{abc} , v_{fdr} , and i_{fdr} .

The steps required in the derivative calculation stage to calculate the time derivatives of the state variables are below.

1. Transform \mathbf{v}_{abc} and \mathbf{i}_{abc} to \mathbf{v}_{qd0s} and \mathbf{i}_{qd0s} , respectively.
2. Calculate \mathbf{i}_{qdr} from (3.29).
3. Calculate \mathbf{v}_{mqd} from (3.31).
4. Calculate $p\boldsymbol{\lambda}_{mqd}$ from (3.8).
5. Calculate $p\mathbf{x}_{d3}$ and $p\mathbf{x}_{q2}$ from (3.27) and (3.28).

3.4 Formulation Comparison

In this section, the four model formulations are compared for four distinct cases. The machine model represents the 59-kW, 560-V, four-pole machine characterized in [58], where its parameters may be found. This model of the machine has been extensively validated in hardware in [63–65]. The simulations are performed using MATLAB R2014a Simulink's ode45 integration algorithm with a maximum time step of 83.3 ms, a relative tolerance of 10^{-6} , and the default absolute tolerance, which is the maximum value that the state variable has assumed over the course of simulation times the relative tolerance [101]. Circuit elements are represented using the Automated State Model Generator, a software package that automatically establishes a state-space model based on the circuit topology [102]. In each case, initial conditions corresponding to steady-state are selected, and each simulation lasts 83.3 ms (5 cycles). The model formulations are all derived from a common set of model

equations, but the case studies are selected such that each is most conducive to a particular formulation. For each case, the SFVBR, which makes no model interface approximations, is simulated at a maximum time step of $1 \mu\text{s}$. For each formulation and each case, the rms errors of the i_{as} and i_{fdr} waveforms with respect to the reference waveforms are calculated. These values are normalized by the rms value of the non-average component of the reference waveforms. Also, the run time associated with each formulation and case is recorded by averaging over 20 simulations. The simulations are performed on Intel(R) Core(TM) i7-3770 CPU @3.40 GHz and 8.00 GB RAM.

In Case I, the field winding is excited by a 30-V source, the stator is connected to an infinite 560-V bus, the machine is rotating at 1800 r/min, and the initial rotor angle is $\pi/8$ rad. The rotor speed increases linearly to 1912.5 r/min over 8.3 ms starting at 20 ms and then decreases linearly back to 1800 r/min at the same rate. This results in the rotor angle increasing to $3\pi/16$ rad. This case can be studied without introducing any model interface approximations because it is consistent with voltage-in, current-out representations of both the stator and field windings. The time steps, run time, and error results for Case I (and all of the cases) are shown in Table 5.3. It can be seen that each formulation has negligible error in both the stator and field currents because none of the formulations require interface approximations. Because the qd formulation is simpler and does not involve time-varying circuit elements, it has the fewest time steps and fastest run time. In terms of time steps, there is about a factor of four penalty for simulating in abc variables on the stator when it is unnecessary (SVBR and SFVBR vs. qd and FVBR). There is relatively little cost to using the circuit model of the field even when it is not required (qd vs. FVBR), which can also be seen in Case II below.

In Case II, the field winding is also excited by a 30-V source, but the stator supplies a rectifier load with LC filter and constant-current dc load of 48 A shown in Figure 3.3. The filter inductance and capacitance are 2.5 mH and 1.4 mF, respectively, and the machine is rotating at 1800 r/min. In such a situation, an interface mismatch between stator

Table 3.1: Case Results

Case	Formulation	Time steps	Run time (s)	i_{aserr} (%)	i_{fderr} (%)
Case I	qd	580	0.30	0.00	0.00
	SVBR	2098	0.54	0.00	0.00
	FVBR	591	0.39	0.00	0.00
	SFVBR	2105	0.66	0.00	0.00
Case II	qd	187388	4.55	1.99	5.37
	SVBR	6613	0.74	0.00	0.00
	FVBR	187928	6.50	1.99	5.37
	SFVBR	6608	0.95	0.00	0.00
Case III	qd	9498	0.56	0.08	0.25
	qd (400 Ω)	12943	0.64	0.04	0.12
	SVBR	11103	1.10	0.08	0.25
	FVBR	6094	0.59	0.00	0.00
	SFVBR	7026	1.08	0.00	0.00
Case IV	qd	202545	5.20	2.30	4.16
	SVBR	26868	1.90	0.03	0.71
	FVBR	205599	7.90	2.31	4.71
	SFVBR	10082	1.35	0.00	0.00

and rectifier load exists for the qd and FVBR formulations. This mismatch is resolved by adding 530- Ω (approximately 100 pu) resistances in parallel with the stator windings. Response to a step increase in field voltage is considered. At $t = 33.3$ ms, the field voltage is stepped to 45 V. It can be seen in Table 5.3 that the SVBR and SFVBR formulations have negligible error because they require no interface approximations. The qd and FVBR formulations exhibit errors in the stator current due to the interface approximation, but this also results in considerable error in the field current. The reference waveforms and detailed views of the waveforms predicted by each formulation are shown in Figure 5.7 and show both these errors and the relatively high number of time steps required by these methods. These methods also require considerably longer run times due to the stiffness introduced by the artificial resistance at the stator. The SVBR formulation had the fastest run time due to lack of artificial stiffness and simplicity relative to the SFVBR formulation. There is

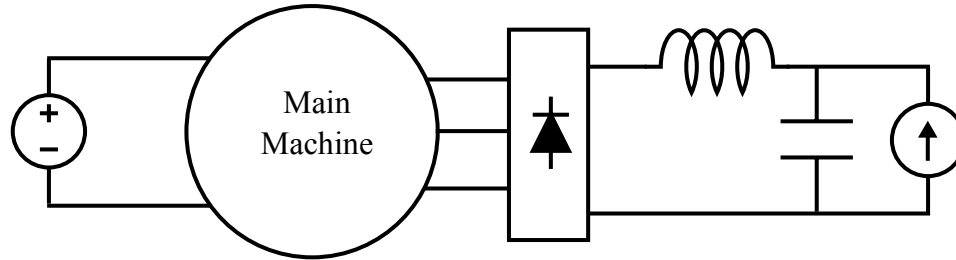


Figure 3.3: Case II arrangement.

about a factor of twenty penalty in number of required time steps for not using the stator circuit interface when required (qd and FVBR vs. SVBR and SFVBR), and this can also be seen in the comparison between the FVBR and SFVBR formulations of Case IV below.

In Case III, the field winding is supplied through a diode rectifier by a 37-V, 120-Hz three-phase source with a series commutating inductance of 2.31 mH and the stator is connected to an infinite 560-V bus shown in Figure 3.5. The machine is rotating at 1800 r/min and the rotor angle is $\pi/8$ rad. In such a situation, an interface mismatch between field and rectifier source exists for the qd and SVBR formulations. This mismatch is resolved by adding a 200- Ω (approximately 100 times the field resistance) resistance in parallel with the field winding. At $t = 20$ ms, one of the upper diodes in the rectifier is shorted. The results are shown in Figure 5.9. It can be seen in the figure and in Table 5.3 that the FVBR and SFVBR formulations have negligible error in both the stator and field currents because neither of the formulations require interface approximations. The qd and SVBR formulations exhibit errors in the field current due to the interface approximation, but this also results in non-negligible error in the stator current. It is observed that the errors associated with interface mismatches at the field result in relatively smaller errors than interface mismatches at the stator (as in Case II). The run time cost associated with the interface mismatches is also smaller. This is attributed to the relatively slow dynamics associated with the field winding relative to the stator windings. In fact, the qd formulation has the smallest run time despite the introduction of a large resistance. However, if the artificial resistance is doubled to 400 Ω , the qd formulation errors are halved (remaining non-negligible) and

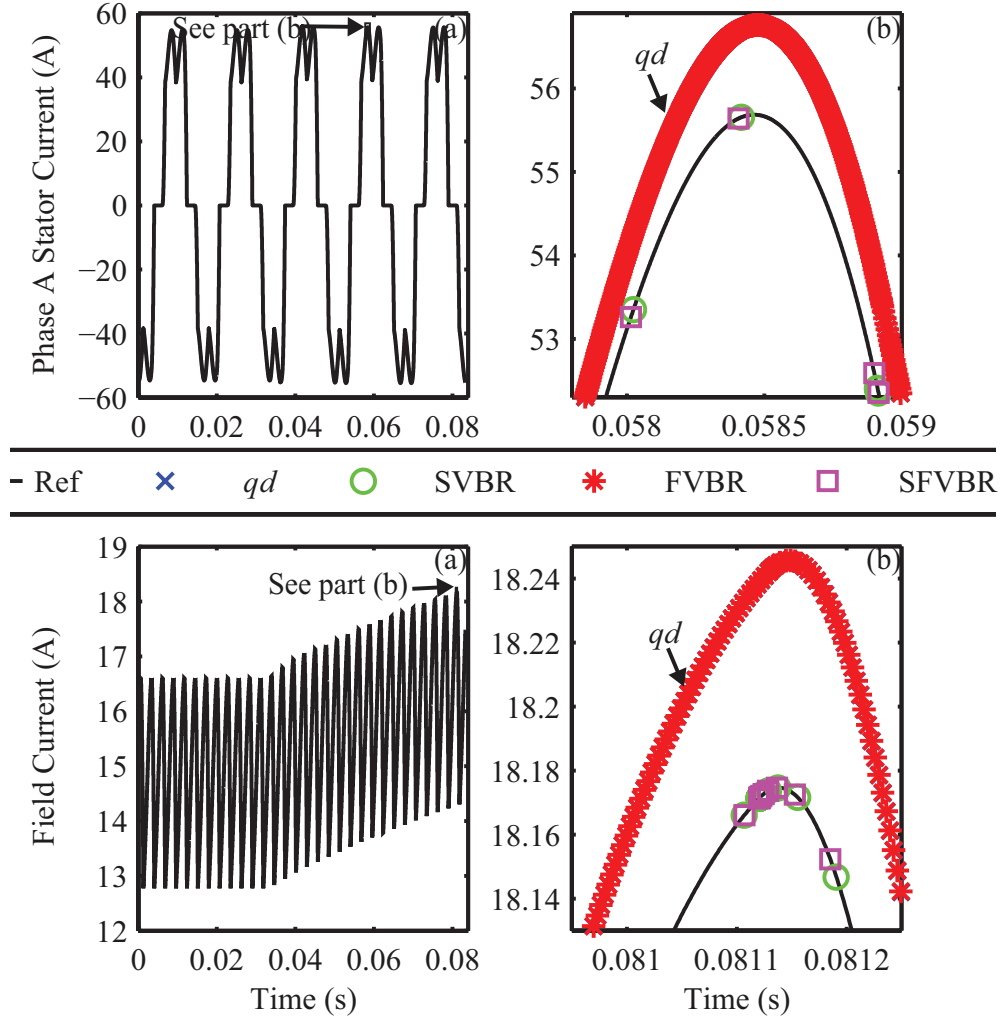


Figure 3.4: Case II results.

the run time exceeds that of the FVBR formulation. The FVBR formulation requires the fewest time steps. There is approximately a factor of two penalty for not using the field circuit representation in this case (qd and SVBR vs. FVBR and SFVBR). In this case, the penalty for simulating in abc variables on the stator when it is not required (SFVBR vs. FVBR) is not as great as in Case I because of the sustained current transient on the stator side.

In Case IV, the field winding is supplied through a diode rectifier as in Case III, and the stator is used to supply a rectifier load as in Case II shown in Figure 3.7. The same interface

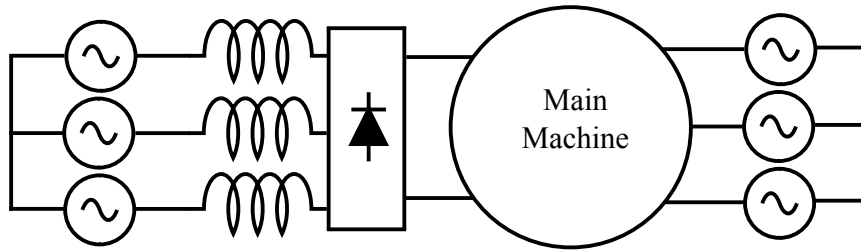


Figure 3.5: Case III arrangement.

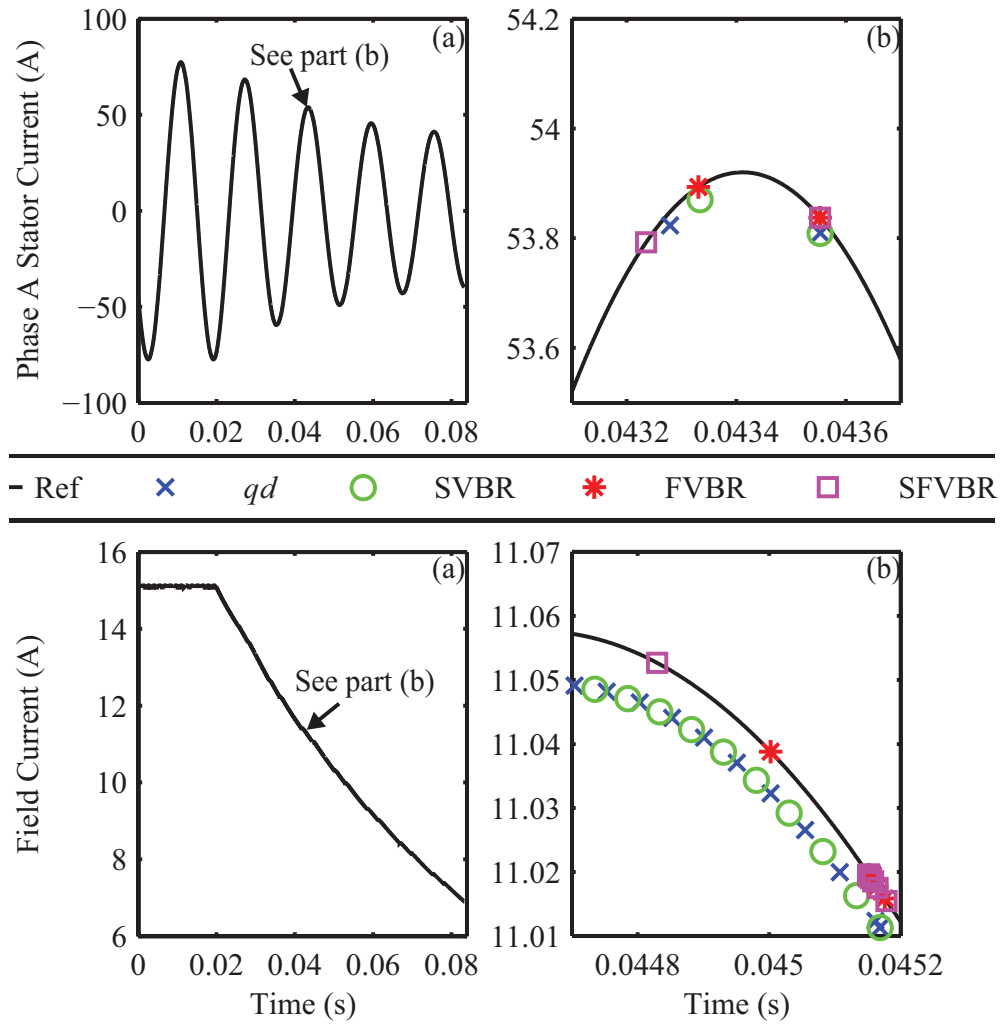


Figure 3.6: Case III results.

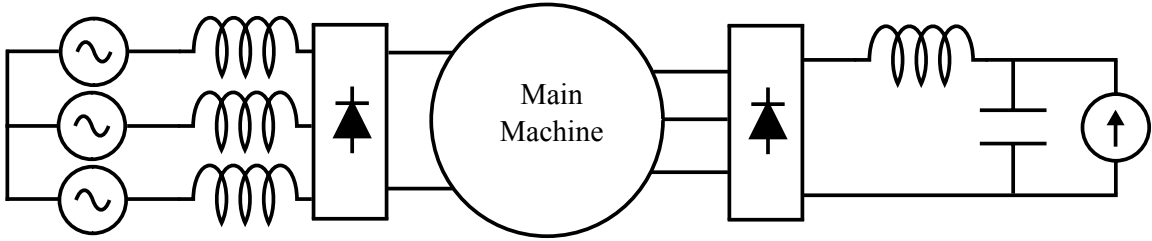


Figure 3.7: Case IV arrangement.

mismatches occur, so the artificial resistances described above are used at the stator for the qd and FVBR formulations and at the field for the qd and SVBR formulations. At $t = 28$ ms, the dc load is stepped from 48 A to 36 A. The results are shown in Figure 5.10. Only the SFVBR formulation has negligible error in both the stator and field currents. It also has the fewest required time steps and the fastest run time. There is about a factor of twenty penalty for not using the stator circuit interface when required (FVBR vs. SFVBR), which corresponds with the results from Case II. It is noted that the SVBR formulation has smaller errors, fewer time steps, and faster run time than the other two formulations, which further indicates that the penalty for inserting artificial resistance at the field is less severe than that for inserting resistance at the stator.

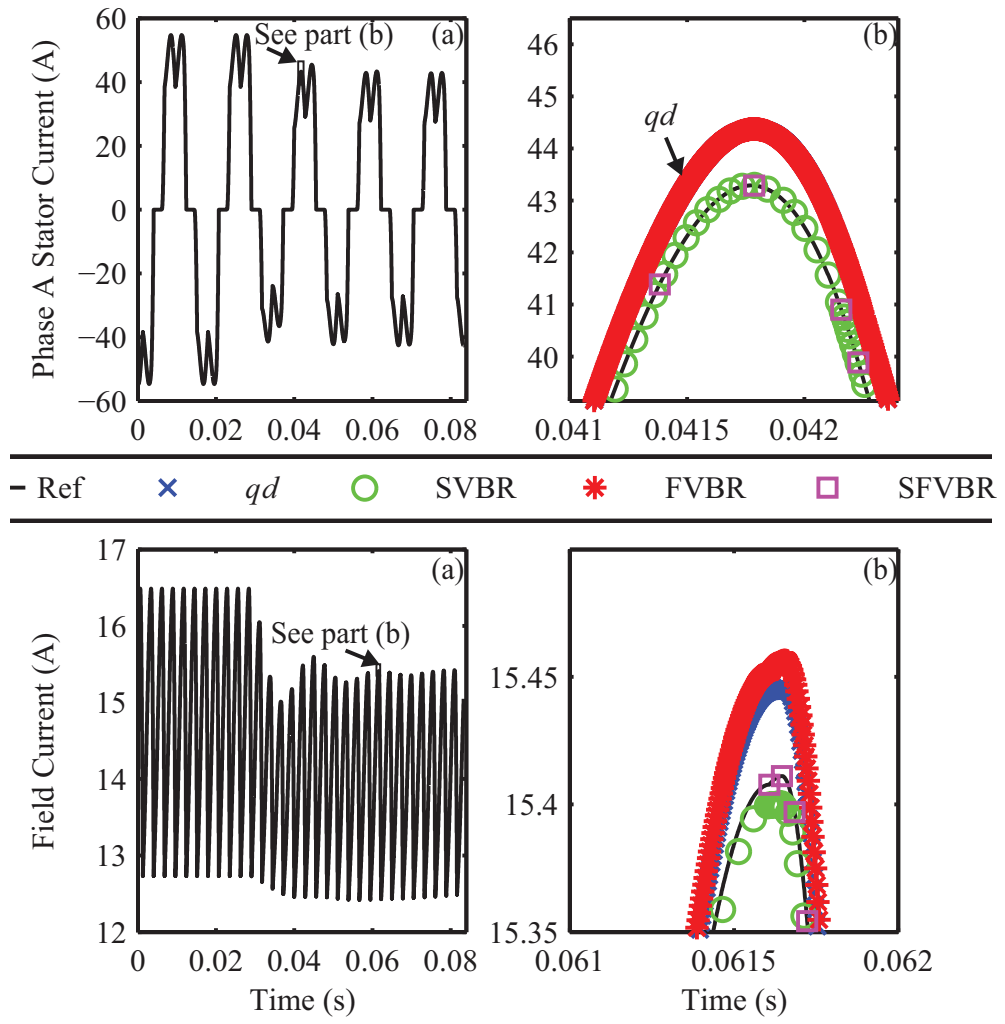


Figure 3.8: Case IV results.

Chapter 4

Numerical Average-Value Modeling of Rotating Rectifiers in Brushless Excitation Systems

Brushless excitation systems are widely used for synchronous machines. As a critical part of the system, rotating rectifiers have significant impact on the system behavior. This chapter presents a numerical average-value model (AVM) for rotating rectifiers in brushless excitation systems, where the essential numerical functions are extracted from the detailed simulations and vary depending on the loading conditions. The work described in this chapter has been published in [99]. Open-circuit voltages of the brushless exciter armature are used to calculate the dynamic impedance that represents the loading condition. The model is validated by comparison with an experimentally validated detailed model of the brushless excitation system in three distinct cases. It has been demonstrated that the proposed AVM can provide accurate simulations in both transient and steady states with fewer time steps and less run time compared with detailed models of such systems and that the proposed AVM can be combined with AVM models of other rectifiers in the system to reduce the overall computational cost.

The remainder of this chapter is organized as follows. The proposed model is described in Section 5.1. The characterization of the rectifier is described in Section 5.2. The model is validated by comparison with an experimentally validated detailed model of the brushless excitation system in Section 5.3.

4.1 Average-Value Model of Brushless Excitation System

Numerical average-value modeling has been successfully applied in a variety of cases involving machine-converter interactions. These techniques are adapted to the rotating rectifier in a brushless excitation system below.

4.1.1 Notation

The electrical rotor speed and position of the exciter machine are

$$\omega_r = \frac{P}{2} \omega_{rm} \quad (4.1)$$

$$\theta_r = \frac{P}{2} \theta_{rm}, \quad (4.2)$$

respectively, where ω_{rm} and θ_{rm} are the mechanical rotor speed and position, respectively, and P is the number of exciter machine poles. The variables associated with the rotor of the exciter machine are denoted $\mathbf{f}_{abc r} = [f_{ar} \ f_{br} \ f_{cr}]^T$ where f can be used to indicate voltage (v), current (i), or flux linkage (λ). These variables can be transformed into the stationary reference frame by use of the transformation

$$\mathbf{f}_{qd0r} = \mathbf{K}_r \mathbf{f}_{abc r}, \quad (4.3)$$

where

$$\mathbf{K}_r = \frac{2}{3} \begin{bmatrix} \cos \theta_r & \cos(\theta_r + \frac{2\pi}{3}) & \cos(\theta_r - \frac{2\pi}{3}) \\ -\sin \theta_r & -\sin(\theta_r + \frac{2\pi}{3}) & -\sin(\theta_r - \frac{2\pi}{3}) \\ \frac{1}{2} & \frac{1}{2} & \frac{1}{2} \end{bmatrix} \quad (4.4)$$

and $\mathbf{f}_{qd0r} = [f_{qr} \ f_{dr} \ f_{0r}]^T$ are the transformed variables. The zero sequence f_{0r} is negligible. The transformed variables can also be expressed in space-phasor notation: $\vec{f} = f_{qr} + jf_{dr}$ for rotating armature variables transformed to the stationary reference frame. Differentiation with respect to time is indicated by the operator p .

Main machine variables are transformed to the qd reference frame using Park's transformation.

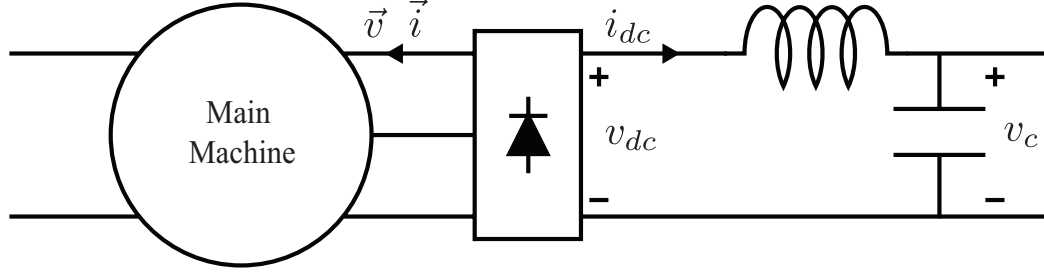


Figure 4.1: Stationary rectifier system.

4.1.2 Rectifier relationships

The proposed numerical average-value model of the brushless excitation system is based on [95]. In [95], the average behavior of the stationary rectifier depicted in Figure 4.1 is represented by the following relationships:

$$\|\vec{v}\| = \alpha_s(z_s)v_{dc} \quad (4.5)$$

$$i_{dc} = \beta_s(z_s)\|\vec{i}\| \quad (4.6)$$

$$\angle\vec{v} = \angle\vec{i} + \phi_s(z_s) + \pi, \quad (4.7)$$

where $\|\cdot\|$ denotes the 2-norm of a vector, \vec{v} and \vec{i} are space phasors associated with the stationary armature variables transformed to the reference frame fixed in the rotor, $\alpha_s(\cdot)$, $\beta_s(\cdot)$, and $\phi_s(\cdot)$ are algebraic functions of the loading condition, the phase offset of π accounts for the fact that the current space phasor \vec{i} is into the machine and thus out of the rectifier, and z_s is a “conveniently defined” dynamic impedance that represents the loading condition and is defined as

$$z_s = \frac{v_c}{\|\vec{i}\|}. \quad (4.8)$$

Similar relationships are utilized for the rotating rectifier in the brushless excitation system shown in Figure 4.2, but these relationships are modified to account for the differences between the stationary and rotating rectifiers. The rotating rectifier is on the rotor and requires a different reference frame transformation, i.e., (5.5). Additionally, the field winding of the main machine does not resemble the LC filter studied in [95]. In particular,

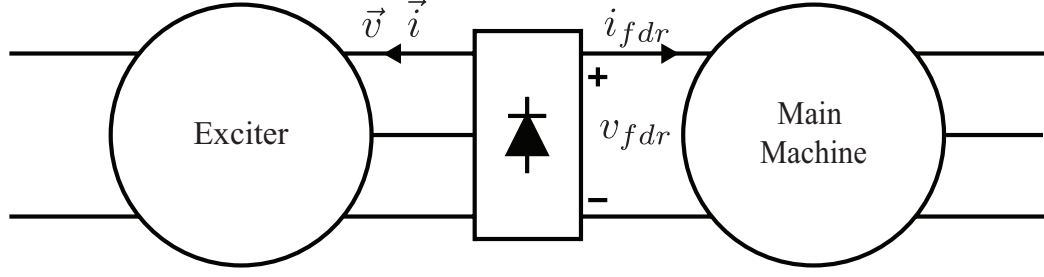


Figure 4.2: Rotating rectifier system.

the average behavior of the rectifier is represented by the following relationships:

$$v_{fdr} = \alpha(z) \|\vec{v}\| \quad (4.9)$$

$$\|\vec{i}\| = \beta(z) i_{fdr} \quad (4.10)$$

$$\angle \vec{v} = \angle \vec{i} + \phi(z) + \pi, \quad (4.11)$$

where z is a dynamic impedance that represents the loading condition. The dynamic impedance considered in [95] was selected because it is readily available in simulation as the capacitor voltage of the LC filter is a state variable. The field winding of the main machine does not exhibit such a voltage. Therefore, an alternative dynamic impedance is employed:

$$z = \frac{\|\mathbf{e}_{qdr}\|}{i_{fdr}}, \quad (4.12)$$

where \mathbf{e}_{qdr} are the open-circuit voltages of the brushless exciter armature as described below.

4.1.3 Brushless exciter model

The brushless exciter machine can be described in the rotor reference frame as

$$v_{qr} = r_r i_{qr} - \omega_r \lambda_{dr} + p \lambda_{qr} \quad (4.13)$$

$$v_{dr} = r_r i_{dr} + \omega_r \lambda_{qr} + p \lambda_{dr} \quad (4.14)$$

$$v'_{fds} = r'_{fds} i'_{fds} + p \lambda'_{fds}, \quad (4.15)$$

where

$$\lambda_{qr} = L_{lr}i_{qr} + L_{mq}i_{qr} \quad (4.16)$$

$$\lambda_{dr} = L_{lr}i_{dr} + L_{md}(i_{dr} + i'_{fds}) + \lambda_{md0} \quad (4.17)$$

$$\lambda'_{fds} = L'_{l'fds}i'_{fds} + L_{md}(i_{dr} + i'_{fds}) + \lambda_{md0}, \quad (4.18)$$

the primed variables represent field variables referred to the rotor, r_r and r'_{fds} are the rotor and (referred) field resistances, L_{lr} and $L'_{l'fds}$ are the rotor and (referred) field leakage inductance, L_{mq} and L_{md} are the q - and d -axis magnetizing inductances, and λ_{md0} is an affine term added to the d -axis magnetizing flux to represent the effects of magnetic hysteresis.

The brushless exciter machine model can be expressed in the stationary reference frame as

$$v_{qr} = r_r i_{qr} - \omega_r L_d i_{dr} + L_q p i_{qr} + e_{qr} \quad (4.19)$$

$$v_{dr} = r_r i_{dr} + \omega_r L_q i_{qr} + L'_d p i_{dr} + e_{dr}, \quad (4.20)$$

where

$$L_q = L_{lr} + L_{mq} \quad (4.21)$$

$$L_d = L_{lr} + L_{md} \quad (4.22)$$

$$L'_d = L_{lr} + \frac{L'_{l'fds} L_{md}}{L'_{l'fds} + L_{md}} \quad (4.23)$$

$$e_{qr} = -\omega_r (L_{md} i'_{fds} + \lambda_{md0}) \quad (4.24)$$

$$e_{dr} = \frac{L_{md}}{L'_{l'fds} + L_{md}} (v'_{fds} - r'_{fds} i'_{fds}). \quad (4.25)$$

It can be seen that $\mathbf{e}_{qdr} = [e_{qr} \ e_{dr}]^T$ are the open-circuit voltages of the brushless exciter armature. Furthermore, substituting (4.17) into (4.14), (4.18) into (4.15), and solving for the time derivative of the field current results in the following:

$$p i'_{fds} = \frac{L_d (v'_{fds} - r'_{fds} i'_{fds}) - L_{md} (v_{dr} - r_r i_{dr} - \omega_r L_q i_{qr})}{L_d L'_{l'fds} - L_{md}^2}. \quad (4.26)$$

4.1.4 Differentiator approximation

Both the armature windings of the exciter machine and the field winding of the main machine are most easily represented using voltage-in, current-out formulations, which corresponds to the case of the stationary rectifier where the main machine and the LC filter are most conveniently represented using voltage-in, current-out formulations. It is noted in [95] that this formulation is problematic because of the representation given in (5.12)–(5.14). In [95], this issue is resolved by using a current-in, voltage-out formulation of the LC filter. In doing this, the inductor in the LC filter acts as a differentiator and has an improper transfer function; this differentiator is replaced with a low-frequency approximation with a proper transfer function. Herein, an alternative approach is pursued that is consistent with the fact that the open-circuit voltages calculated in (4.24) and (4.25) are used to calculate the dynamic impedance z in (5.15).

In the proposed approach, the armature windings of the exciter machine are represented using a current-in, voltage-out formulation. It can be seen from (4.19) and (4.20) that such an approach also entails differentiators. Using a similar approach to that used in [95], a low-frequency approximation with proper transfer function is proposed. In particular,

$$p\mathbf{x} = \mathbf{A}\mathbf{x} + \mathbf{B} \begin{bmatrix} i_{qr} \\ i_{dr} \end{bmatrix} \quad (4.27)$$

$$\begin{bmatrix} pi_{qr} \\ pi_{dr} \end{bmatrix} \approx \mathbf{C}\mathbf{x} + \mathbf{D} \begin{bmatrix} i_{qr} \\ i_{dr} \end{bmatrix}, \quad (4.28)$$

where \mathbf{A} , \mathbf{B} , \mathbf{C} , and \mathbf{D} are 2×2 matrices associated with the realization of the approximation and \mathbf{x} is a vector of two state variables associated with the realization. It is convenient to

express the rows of \mathbf{C} and the elements of \mathbf{D} as

$$\mathbf{C} = \begin{bmatrix} \mathbf{c}_1^T \\ \mathbf{c}_2^T \end{bmatrix} \quad (4.29)$$

$$\mathbf{D} = \begin{bmatrix} d_{11} & d_{12} \\ d_{21} & d_{22} \end{bmatrix}. \quad (4.30)$$

This realization is an appropriate low-frequency approximation of the differentiators in (4.19) and (4.20) if

$$\lim_{s \rightarrow 0} \frac{\mathbf{C}(s\mathbf{I} - \mathbf{A})^{-1}\mathbf{B} + \mathbf{D}}{s} = \mathbf{I}, \quad (4.31)$$

where \mathbf{I} is the 2×2 identity matrix.

It is shown below that specifying a certain structure for \mathbf{D} can facilitate the model integration. For a given \mathbf{D} , the condition in (4.31) is satisfied if the remaining matrices are expressed as

$$\mathbf{A} = -\mathbf{\Lambda} \quad (4.32)$$

$$\mathbf{B} = \mathbf{V}^{-1} \quad (4.33)$$

$$\mathbf{C} = -\mathbf{V}\mathbf{\Lambda}^2, \quad (4.34)$$

where $\mathbf{D} = \mathbf{V}\mathbf{\Lambda}\mathbf{V}^{-1}$ and $\mathbf{\Lambda}$ is a diagonal matrix. The eigenvalues of \mathbf{A} , i.e., the negatives of the eigenvalues of \mathbf{D} , are associated with the bandwidth of the differentiator approximation and should be situated sufficiently far into the left half plane.

4.1.5 Model integration

By substitution of (4.28) into (4.19) and (4.20), the rotor voltages can be approximated as

$$\begin{aligned}
 v_{qr} &\approx r_r i_{qr} - \omega_r L_d i_{dr} + e_{qr} + L_q \mathbf{c}_1^T \mathbf{x} \\
 &\quad + L_q d_{11} i_{qr} + L_q d_{12} i_{dr} \\
 &= r_r i_{qr} - \omega_r L_d i_{dr} + u_q \\
 &\quad + L_q d_{11} i_{qr} + L_q d_{12} i_{dr}
 \end{aligned} \tag{4.35}$$

$$\begin{aligned}
 v_{dr} &\approx r_r i_{dr} + \omega_r L_q i_{qr} + e_{dr} + L_d'' \mathbf{c}_2^T \mathbf{x} \\
 &\quad + L_d'' d_{21} i_{qr} + L_d'' d_{22} i_{dr} \\
 &= r_r i_{dr} + \omega_r L_q i_{qr} + u_d \\
 &\quad + L_d'' d_{21} i_{qr} + L_d'' d_{22} i_{dr},
 \end{aligned} \tag{4.36}$$

where

$$u_q = e_{qr} + L_q \mathbf{c}_1^T \mathbf{x} \tag{4.37}$$

$$u_d = e_{dr} + L_d'' \mathbf{c}_2^T \mathbf{x}. \tag{4.38}$$

It can be seen that (4.35) and (4.36) transform into

$$v_{qr} \approx R i_{qr} - X i_{dr} + u_q \tag{4.39}$$

$$v_{dr} \approx R i_{dr} + X i_{qr} + u_d \tag{4.40}$$

if the following conditions hold:

$$R = r_r + L_q d_{11} = r_r + L_d'' d_{22} \tag{4.41}$$

$$X = \omega_r L_d - L_q d_{12} = \omega_r L_q + L_d'' d_{21} \tag{4.42}$$

for some constants R and X . Furthermore, if approximately constant speed is assumed, i.e.,

$\omega_r \approx \omega_r^*$, where ω_r^* is the nominal speed, then

$$X \approx X^* = \omega_r^* L_d - L_q d_{12} = \omega_r^* L_q + L_d'' d_{21} \tag{4.43}$$

and is approximately constant. These conditions can be made to hold by choice of \mathbf{D} . For example, \mathbf{D} can be defined as

$$\mathbf{D} = \begin{bmatrix} \frac{R-r_r}{L_q} & \frac{\omega_r^* L_d - X^*}{L_q} \\ \frac{X^* - \omega_r^* L_q}{L_d''} & \frac{R-r_r}{L_d''} \end{bmatrix}. \quad (4.44)$$

By choice of a sufficiently large R the eigenvalues of \mathbf{D} can be placed sufficiently far into the right half plane. It is noted that \mathbf{D} is selected based on a constant speed assumption and that variation from the nominal speed will introduce error in the exciter representation.

With such a suitable differentiator approximation, the voltage equations can be expressed in space-phasor form as

$$\vec{v} \approx Z\vec{i} + \vec{u}, \quad (4.45)$$

where $Z = R + jX$ and $\vec{u} = u_q + ju_d$. In this form, the model can be integrated. The magnitude of the exciter machine currents can be found from (5.13). The voltage equation (4.45) can be combined with (4.11) and expressed as

$$\|\vec{v}\| e^{j(\angle \vec{i} + \phi(z))} \approx -Z\|\vec{i}\| e^{j\angle \vec{i}} - \vec{u}. \quad (4.46)$$

This relationship can be used to calculate

$$\|\vec{v}\| \approx \sqrt{\|\vec{u}\|^2 - \text{Im}^2[Z\|\vec{i}\|e^{-j\phi(z)}] - \text{Re}[Z\|\vec{i}\|e^{-j\phi(z)}]} \quad (4.47)$$

$$\angle \vec{i} \approx \angle \frac{-\vec{u}}{\|\vec{v}\| e^{j\phi(z)} + Z\|\vec{i}\|}. \quad (4.48)$$

Finally, (4.9) can be used to determine the main machine field voltage.

4.1.6 Model summary

The proposed model is depicted graphically in Figure 5.2 and summarized in the steps below.

1. The main machine field current i_{fdr} is calculated by the model of the main machine.

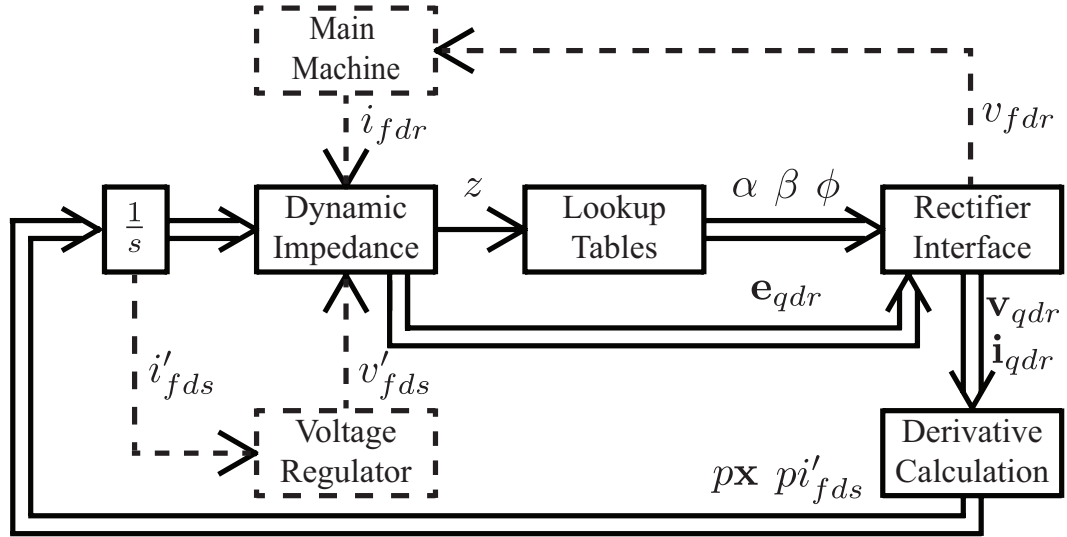


Figure 4.3: Summary of model formulation (dashed lines represent external interfaces to/from the proposed model).

2. The exciter field current i'_{fds} is a state variable and used in the voltage regulator model.
3. The exciter machine field voltage v'_{fds} is calculated by the model of the voltage regulator.
4. The open-circuit voltages of the exciter machine e_{qdr} are calculated using (4.24) and (4.25)
5. The dynamic impedance z is calculated using (5.15).
6. The magnitude of the exciter machine currents $\|\vec{i}\|$ is calculated using (5.13).
7. The magnitude of the exciter machine voltages $\|\vec{v}\|$ and the angle of the exciter machine currents $\angle \vec{i}$ are calculated using (4.47) and (4.48), respectively.
8. The main machine field voltage v_{fdr} is calculated using (4.9) and used in the model of the main machine.
9. The derivatives of the state variables associated with the differentiator approximation px are calculated using (4.27).

10. The time derivative of the exciter field current $p i'_{fds}$ is calculated using (4.26).

4.2 Rectifier Characterization

In order to use the proposed model, the numerical functions $\alpha(\cdot)$, $\beta(\cdot)$, and $\phi(\cdot)$ must be extracted from the detailed simulations. The extraction of such functions has been discussed in [96]. In particular, it is found that because the functions describe algebraic relationships that are assumed to hold continuously, these functions can be extracted from transient simulations rather than requiring numerous steady-state simulations. This is important in the case of the rotating rectifier in a brushless excitation system because the steady-state dynamic impedance z varies over a very narrow range. Transient simulations are necessary to characterize the performance of the rectifier over a wide loading range.

The system considered herein is shown in Figure 4.2. The main machine is a four-pole, 59 kVA, 560 V synchronous generator with the model and parameters presented in [64] and [58]. This machine model has been extensively validated against experimental measurements [63–65]. For detailed simulation, it is modeled using the field-only voltage-behind-reactance (FVBR) formulation [16]. The exciter machine formulation, an armature-only voltage-behind-reactance (AVBR) formulation, described below is used to perform detailed simulations. The parameters of the machine are found in Table 4.1 [65]. The voltage equation is

$$\mathbf{v}_{abcr} = \mathbf{R}\mathbf{i}_{abcr} + \mathbf{L}p\mathbf{i}_{abcr} + \mathbf{e}_{abcr}. \quad (4.49)$$

The resistance matrix is

$$\mathbf{R} = r_r \mathbf{I}_3 + p\mathbf{L}_r - \frac{2}{3} \frac{\mathbf{L}'_{rfdsp}\mathbf{L}'_{rfdspT}}{L'_{fds}}, \quad (4.50)$$

where

$$\mathbf{L}_r = \begin{bmatrix} L_{lr} + L_A & -\frac{1}{2}L_A & -\frac{1}{2}L_A \\ -\frac{1}{2}L_A & L_{lr} + L_A & -\frac{1}{2}L_A \\ -\frac{1}{2}L_A & -\frac{1}{2}L_A & L_{lr} + L_A \end{bmatrix} - L_B \begin{bmatrix} \cos(2\theta_r) & \cos(2(\theta_r + \frac{\pi}{3})) & \cos(2(\theta_r - \frac{\pi}{3})) \\ \cos(2(\theta_r + \frac{\pi}{3})) & \cos(2(\theta_r + \frac{2\pi}{3})) & \cos(2(\theta_r - \pi)) \\ \cos(2(\theta_r - \frac{\pi}{3})) & \cos(2(\theta_r - \pi)) & \cos(2(\theta_r - \frac{2\pi}{3})) \end{bmatrix} \quad (4.51)$$

$$\mathbf{L}'_{rfds} = -L_{md} \begin{bmatrix} \sin \theta_r \\ \sin(\theta_r + \frac{2\pi}{3}) \\ \sin(\theta_r - \frac{2\pi}{3}) \end{bmatrix} \quad (4.52)$$

$$L'_{fds} = L'_{lfds} + L_{md} \quad (4.53)$$

$$L_A = \frac{L_{md} + L_{mq}}{3} \quad (4.54)$$

$$L_B = \frac{L_{md} - L_{mq}}{3}. \quad (4.55)$$

The inductance matrix is

$$\mathbf{L} = \mathbf{L}_r - \frac{2}{3} \frac{\mathbf{L}'_{rfds} \mathbf{L}'_{rfds}{}^T}{L'_{fds}}. \quad (4.56)$$

The voltage vector is

$$\mathbf{e}_{abcr} = -\omega_r \lambda_{md0} \begin{bmatrix} \cos \theta_r \\ \cos(\theta_r + \frac{2\pi}{3}) \\ \cos(\theta_r - \frac{2\pi}{3}) \end{bmatrix} + \frac{\mathbf{L}'_{rfds}}{L'_{fds}} v'_{fds} + (p \mathbf{L}'_{rfds} - \frac{\mathbf{L}'_{rfds} r'_{fds}}{L'_{fds}}) i'_{fds}. \quad (4.57)$$

The detailed simulations is performed using MATLAB R2016a Simulink's ode23tb integration algorithm with a maximum time step of 10.85 μ s and default values for the relative and absolute tolerances. Circuit elements are represented using the Automated State Model Generator, a software package that automatically establishes a state-space model based on the circuit topology and switch states [102].

Table 4.1: Brushless Exciter Parameters

P	8	N_r/N_{fds}	0.07
r_r	0.121 Ω	L_{lr}	0.49 mH
r_{fds}	4.69 Ω	$L_{l_{fds}}$	0.117 mH
L_{mq}	1.82 mH	L_{md}	3.49 mH
λ_{md0}	5.69 mVs		

For the characterization of the rectifier, the main machine is loaded with a balanced three-phase resistive load that draws rated power at rated voltage. Initial conditions are set corresponding to a zero-flux state. The shaft is rotated at a constant $2\pi 30$ rad/s (1800 RPM), and the frequency of the switching ripple in the rotor quantities is 720 Hz. The field voltage of the exciter is ramped from -0.8 V (corresponding to zero flux linkage) to 8 V in 3.33 s (200 cycles) and then ramped back down to -0.8 V in the following 3.33 s (200 cycles). Averaging the waveforms from the detailed simulation over 60-Hz windows every $1/720$ s yields the values shown in Figure 4.4. The least-squares spline approximation SPAP2 algorithm is used to select support points, and it can be seen in Figure 4.4 that these data are well represented using cubic splines with relatively few support points, which are given in Table 4.2. Furthermore, both the $\alpha(\cdot)$ and $\phi(\cdot)$ functions have discontinuities occurring at approximately 2.97 Ω . For values of dynamic impedance smaller than this, the values of both $\alpha(\cdot)$ and $\phi(\cdot)$ are zero.

4.3 Model Validation

In this section, the brushless excitation system AVM is validated with the detailed model in three distinct cases. All simulations are performed using MATLAB R2016a Simulink's ode23tb integration algorithm with the automatic maximum time step, a relative tolerance of 10^{-6} , and the default absolute tolerance. Circuit elements are represented using the Automated State Model Generator [102]. In order to place the eigenvalues of \mathbf{D} sufficiently far into the right half plane, R and X^* are selected to be $r_r + \sqrt{L_q L_d''} \times 10^5$ rad/s and $\omega_r^* \sqrt{L_q L_d}$, respectively. In each case, initial conditions corresponding to steady state are selected, and

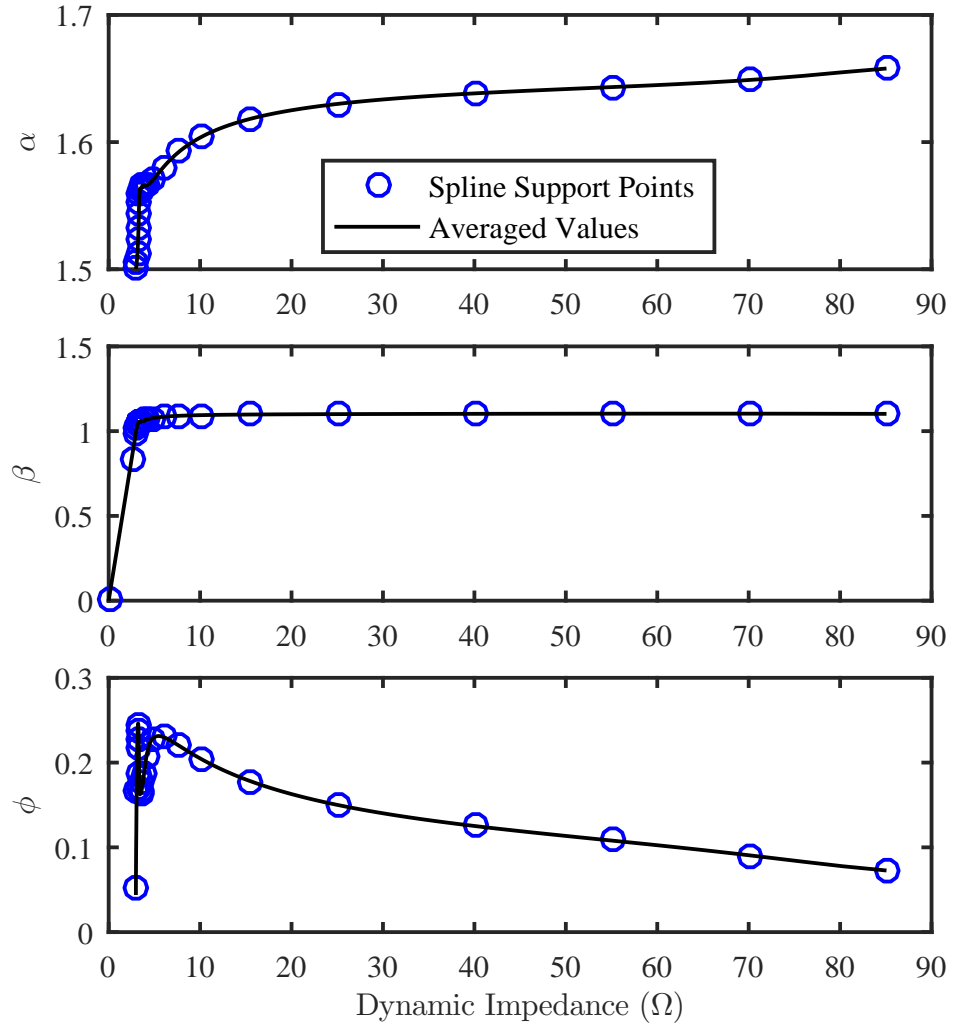


Figure 4.4: Functions $\alpha(\cdot)$, $\beta(\cdot)$, and $\phi(\cdot)$.

each simulation lasts 0.5 s (30 cycles). Also, the run time associated with each model and case is recorded by averaging over 20 simulations. The simulations are performed on an Intel Core i7-3770 CPU running at 3.40 GHz with 8.00 GB of RAM. For comparison, the analytical AVM presented in [81] is also simulated in these cases.

In Case I, the main machine field winding is supplied through a rotating rectifier, which is connected to an exciter with 10-V field voltage. The stator is connected to an infinite 560-V bus. The machine is rotating constantly at $2\pi 30$ rad/s, and the initial rotor angle is 22° . Under this condition, the generator is supplying 46 kW at a power factor of 0.8 lagging. At $t = 1/60$ s, the field voltage of the exciter is stepped down to 8 V, resulting in the

Table 4.2: Support Points for Functions $\alpha(\cdot)$, $\beta(\cdot)$, and $\phi(\cdot)$

z	$\alpha(\cdot)$	$\beta(\cdot)$	$\phi(\cdot)$
0.000	0.000	0.000	0.000
2.529	0.842	0.842	0.000
2.976	1.500	0.990	0.051
3.059	1.505	1.016	0.167
3.141	1.512	1.035	0.228
3.223	1.524	1.047	0.246
3.269	1.534	1.051	0.237
3.299	1.543	1.053	0.216
3.334	1.553	1.053	0.187
3.378	1.559	1.054	0.171
3.454	1.562	1.055	0.163
3.594	1.565	1.058	0.167
3.738	1.565	1.060	0.176
3.864	1.565	1.063	0.187
4.122	1.566	1.068	0.206
4.829	1.570	1.077	0.228
5.973	1.580	1.085	0.230
7.707	1.592	1.091	0.220
10.034	1.604	1.094	0.205
15.480	1.618	1.098	0.178
25.106	1.630	1.100	0.150
40.098	1.638	1.102	0.125
55.089	1.643	1.103	0.108
70.080	1.649	1.103	0.091
85.072	1.658	1.102	0.073

power factor increasing to 0.9 lagging and the reactive power delivered being decreased by 38%. For the detailed simulation, the FVBR formulation of the main machine is used with the detailed representation of the rotating rectifier and the AVBR formulation of the exciter machine. For the analytical AVM simulation, the qd formulation of the main machine is used with an analytical AVM of the brushless excitation system with a reduced-order exciter machine representation [81]. For the numerical AVM simulation, the qd formulation of the main machine is used with the AVM of the brushless excitation system. The time steps and run time for all of the cases are given in Table 5.3. The armature and field currents and voltages of both the exciter and main machine are shown in Figure 4.5 and

Table 4.3: Model Computational Efficiency

Case	Simulation	Time steps	Run time (s)
Case I	Detailed	160179	4.05
	Analytical AVM	1626	4.21
	Numerical AVM	1664	0.24
Case II	Detailed	149575	3.90
	Analytical AVM	12043	26.89
	Numerical AVM	4129	0.26
Case III	Detailed	186778	8.41
	Analytical AVM	143918	323.82
Numerical	Stationary AVM	201952	5.98
	Rotating AVM	180903	6.73
	Full AVM	4347	0.39

Figure 4.6. It can be seen in the figure that the proposed numerical AVM faithfully represents the low-frequency behavior of the main machine and brushless excitation system. The waveforms predicted by the numerical AVM lie within the switching envelope of the waveforms predicted by the detailed model. The deviations of the analytical AVM from the detailed model and numerical AVM are fairly small and largely due to assumptions made in the derivation of the analytical model. Furthermore, it can be seen in Table 5.3, the number of time steps required by the numerical AVM is slightly greater than that required for the analytical AVM, but the run time is reduced by a factor of 15. Both the numbers of time steps and the run time required by the simulation algorithm are drastically reduced compared with the detailed model; the number of time steps is reduced by a factor of 96, and the run time is reduced by a factor of 17.

In Case II, the main machine field winding is supplied through a rotating rectifier, and the stator is connected to an infinite 560-V bus and starts from the same conditions as in Case I. At $t = 1/60$ s, a voltage sag occurs, and the magnitude of the output voltage drops to 95% of the initial value. The same machine formulations and rectifier representations used in Case I are used for the detailed and AVM simulations. The waveforms predicted by the AVM model and the detailed model are compared in Figure 4.7 and Figure 4.8. As with Case I, the AVM model waveforms are situated within the switching envelope of the de-

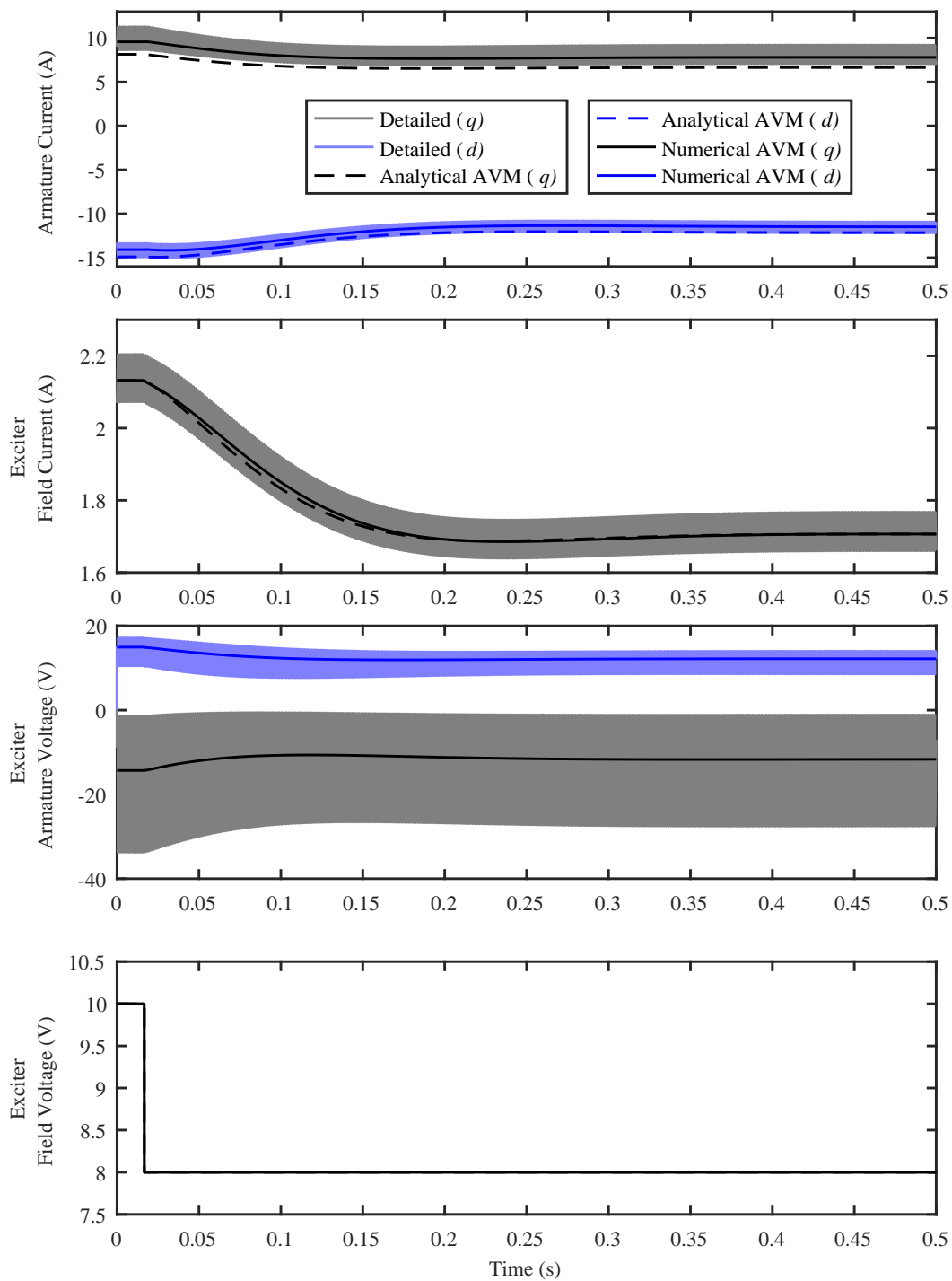


Figure 4.5: Case I (excitation voltage step change) results.

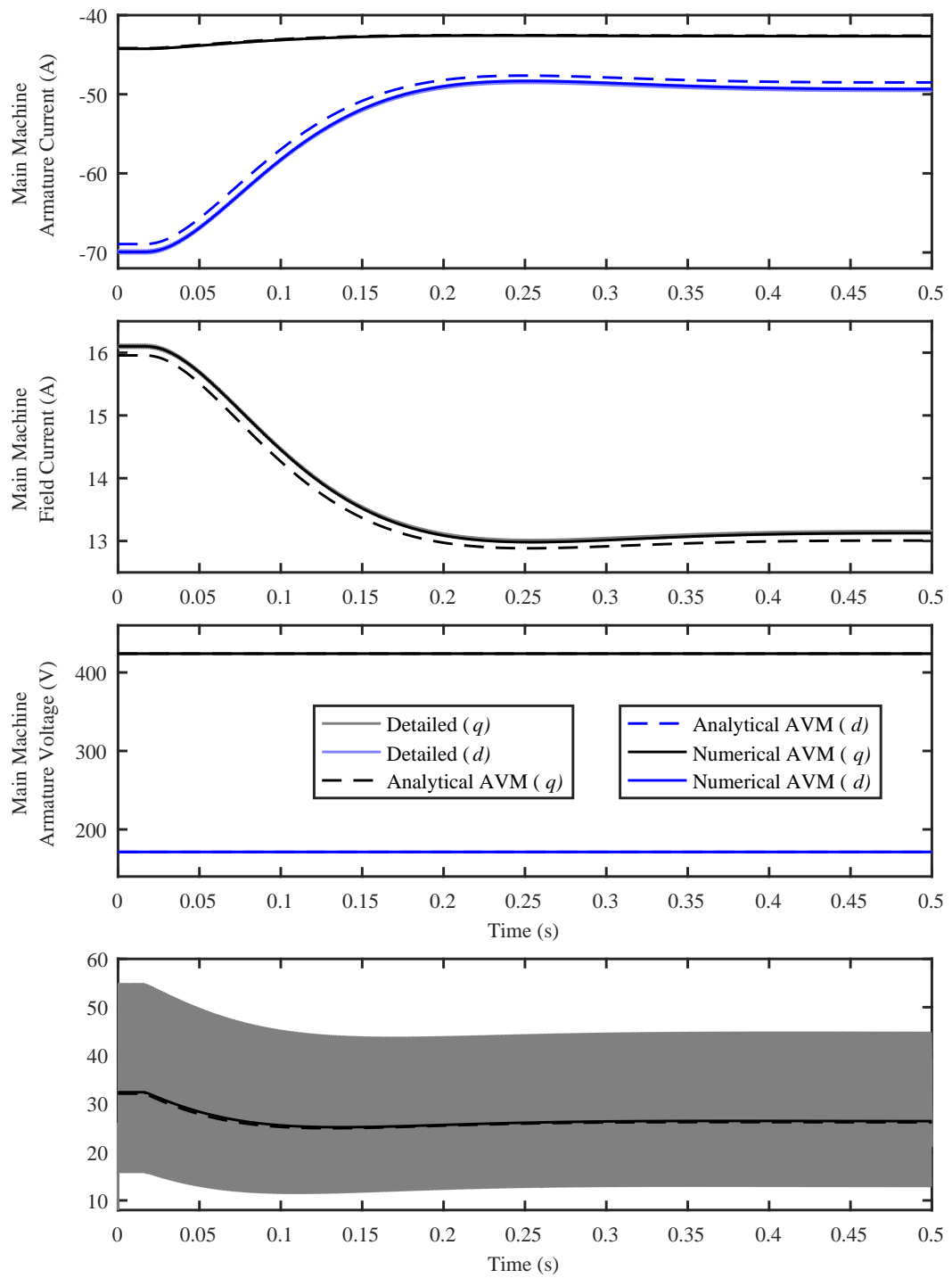


Figure 4.6: Case I (excitation voltage step change) results.

tailed model waveforms, and the AVM model is capable of representing the low-frequency behavior of the system. The analytical AVM demonstrates similarly small deviations from the detailed model and numerical AVM. In Table 5.3, it can be seen that similarly drastic reductions in computational cost are obtained. The number of time steps is reduced by a factor of 36, and the run time is reduced by a factor of 15. When compared with the analytical AVM, the number of time steps is reduced by a factor of 3, and the run time is reduced by a factor of 104.

In Case III, the main machine field winding is supplied through a rotating rectifier, which is connected to an exciter with 7.27-V field voltage. The stator is used to supply a rectifier load with LC filter and resistive load of 11.1Ω shown in Figure 5.8.

The filter inductance and capacitance are 2.5 mH and 1.4 mF, respectively, and the machine is rotating at $2\pi 30$ rad/s. At $t = 1/60$ s, the resistive load is stepped from 11.1Ω to 34.4Ω . This case corresponds to the experimental results used to validate the machine model in [58]. For the detailed simulation, the detailed representation of the stationary rectifier load, the SFVBR formulation of the main machine, the detailed representation of the rotating rectifier, and the AVBR formulation of the exciter machine are used. As this case includes two rectifiers, it is possible to perform averaging with either or both of these rectifiers. For the stationary AVM simulation, the numerical AVM of the stationary rectifier load, the FVBR formulation of the main machine, the detailed representation of the rotating rectifier, and the AVBR formulation of the exciter machine are used. The numerical AVM of the stationary rectifier load is implemented as described in [95] and parameterized using the SVBR formulation of the main machine excited with constant dc voltage and loaded with a varying resistive load as described in [96]. For the rotating AVM simulation, the detailed representation of the stationary rectifier load, the SVBR formulation of the main machine, and the numerical AVM of the brushless excitation system are used. For the full AVM simulation, the numerical AVM of the stationary rectifier load, the qd formulation of the main machine, and the numerical AVM of the brushless excitation system are used. For

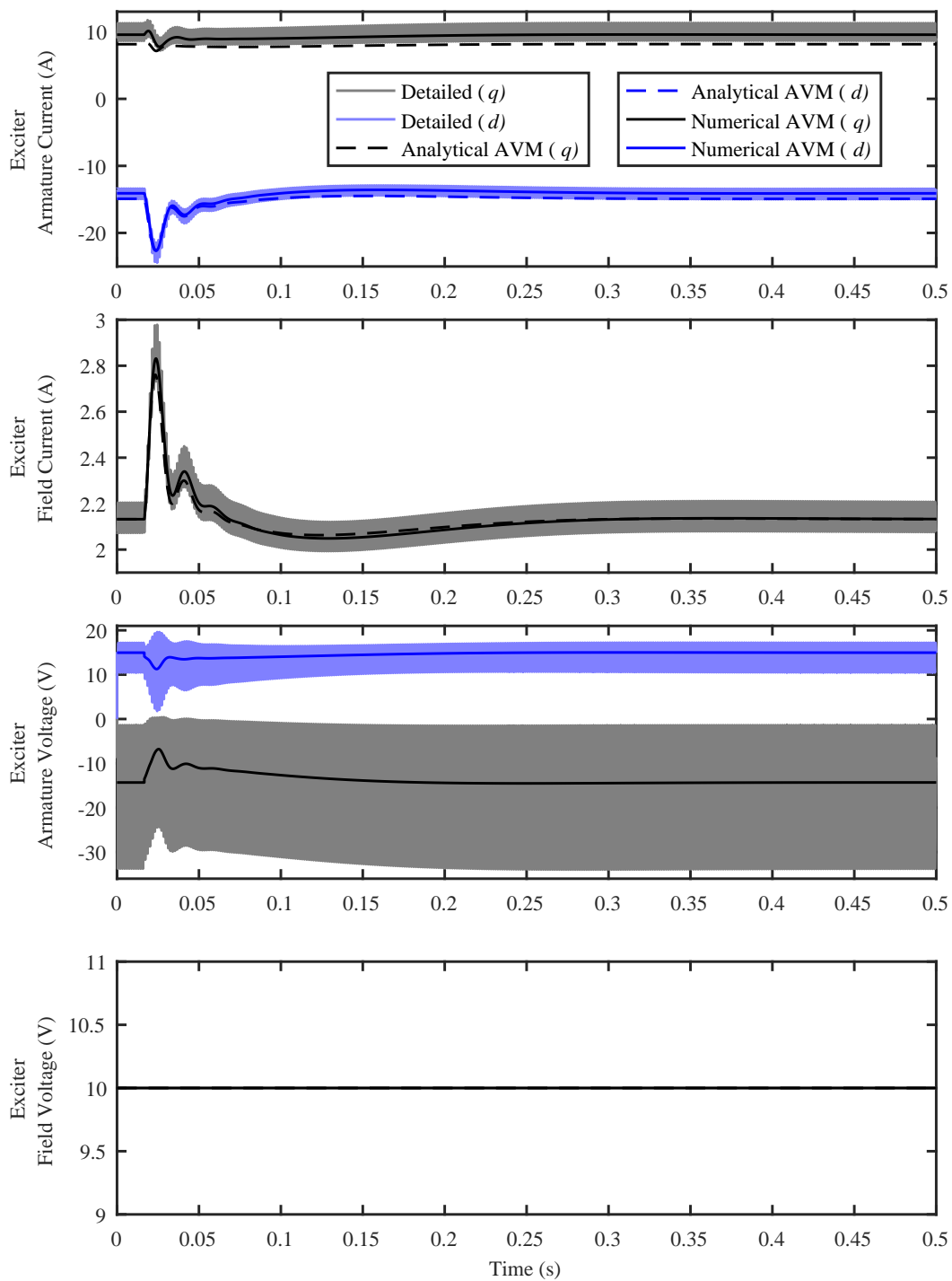


Figure 4.7: Case II (terminal voltage step change) results.

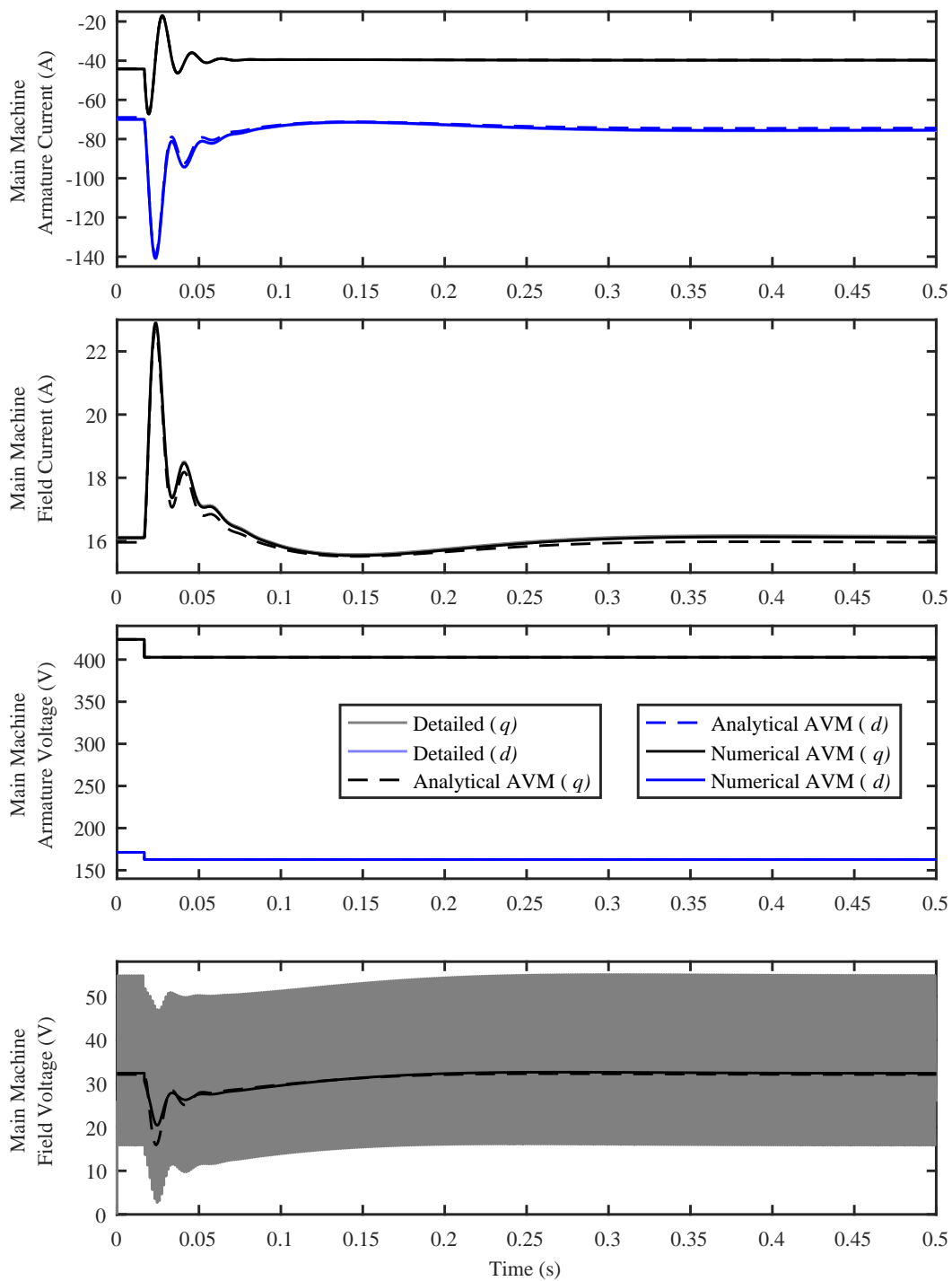


Figure 4.8: Case II (terminal voltage step change) results.

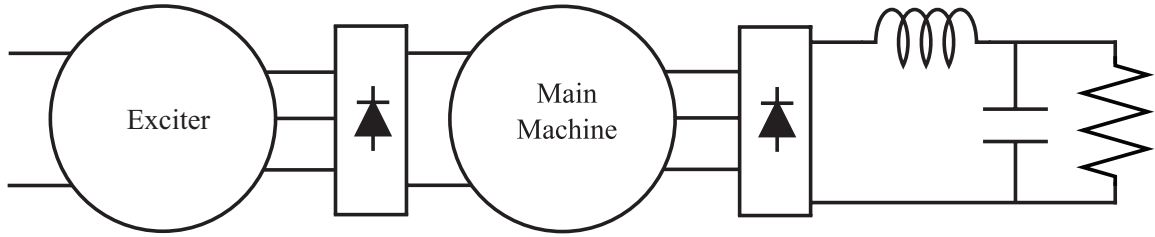


Figure 4.9: Case III circuit.

the analytical AVM simulation, the detailed representation of the stationary rectifier load, the SVBR formulation of the main machine, and an analytical AVM of the brushless excitation system with a reduced-order exciter machine representation are used; this corresponds most closely to the rotating AVM simulation. The currents and voltages predicted by the AVM model and the detailed model are shown in Figure 4.10 and Figure 4.11. Because of the complexity of the waveforms in this case, the q -axis armature current of the exciter is examined more carefully in Figure 5.9. In this case, the two rectifiers produce harmonics at two different specific frequencies because of the difference in the number of poles in the main and exciter machines. The rotating rectifier produces harmonics at 720 Hz and multiples thereof, and the stationary rectifier produces harmonics at 360 Hz and multiples thereof, which includes smaller components at multiples of 720 Hz. Each AVM averages out the harmonics that correspond to the rectifier in question. The partial AVMs, models that only represent one of the rectifiers with an AVM, retain the harmonics associated with the other rectifier. The results of the detailed model and full AVM are shown in the top plot, and it can be seen that the full AVM is capable of representing the low-frequency behavior of the system. In the middle plot, the steady-state behavior of the four models is shown. It can be seen that the full AVM waveform is dc, that the stationary AVM waveform appears periodic with a frequency of 720 Hz, and that the rotating AVM appears periodic with a frequency of 360 Hz. The detailed model waveform clearly contains components at each of these frequencies. This corresponds to the interpretation that the stationary AVM removes the 360-Hz components associated with the stationary rectifier while retaining the 720-Hz components associated with the rotating rectifier and that the rotating AVM does the op-

posite. A fast Fourier transform (FFT) of these waveforms confirms this interpretation as can be seen in the bottom plot of Figure 5.9. The full AVM only retains the dc component, and the partial AVMs retain the harmonics associated with the rectifier that is not averaged by the AVM. It can be seen that both of the partial AVMs have much less improvement in computational cost. The number of time steps for the stationary AVM is actually greater than that required for the detailed model, and the rotating AVM only reduces this number by 3%. The run times of the stationary and rotating AVMs are only reduced by 29% and 20%, respectively. However, the full AVM results in a factor of 43 decrease in time steps and a factor of 22 decrease in run time. The computational cost benefits of the AVM are only realized fully when all of the rectifiers in the system are represented by an AVM. Because of the high computational cost of each time step in the analytical AVM, the use of a partial analytical AVM is very costly in such a scenario.

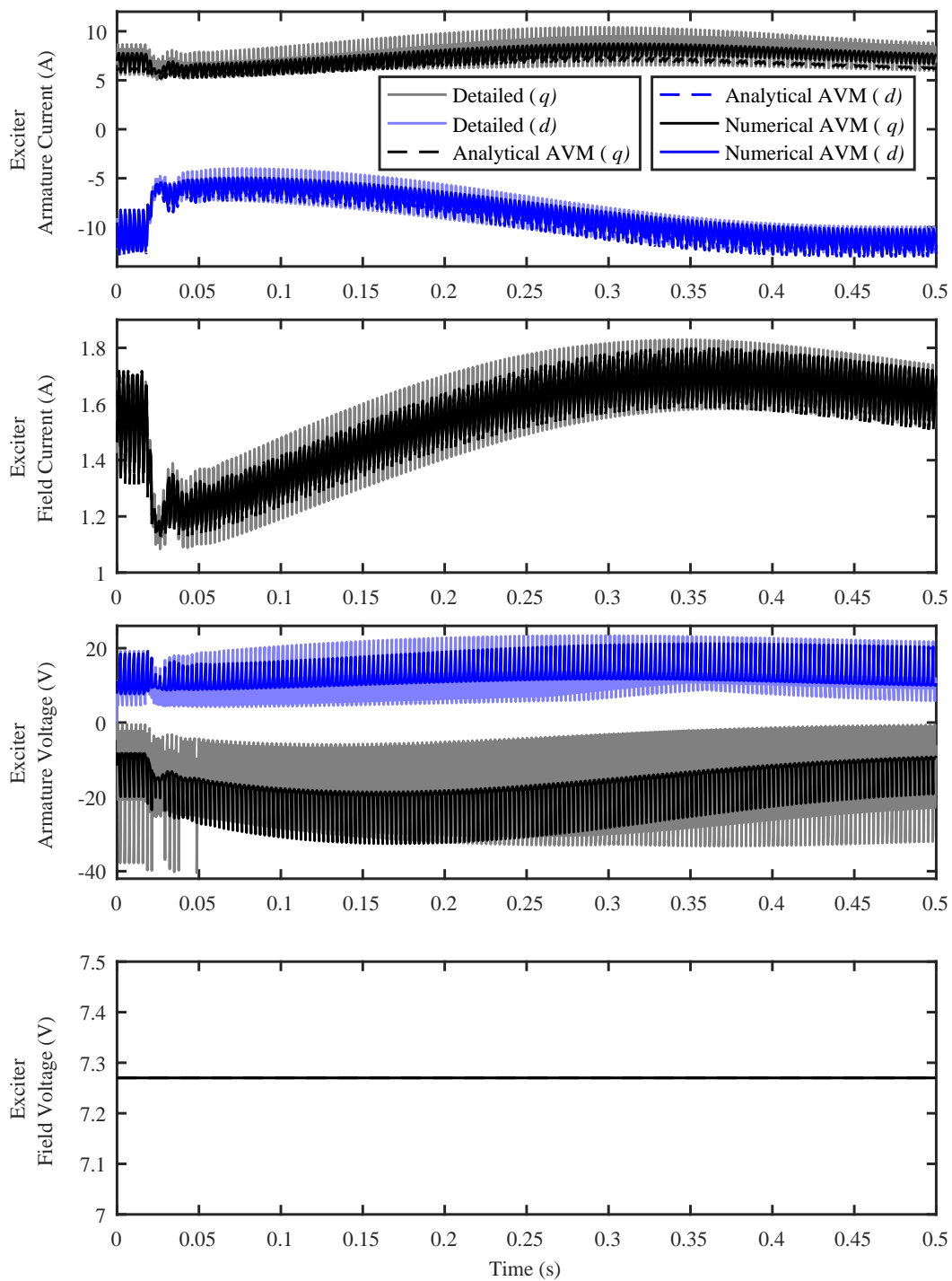


Figure 4.10: Case III (rectifier load step change) results.

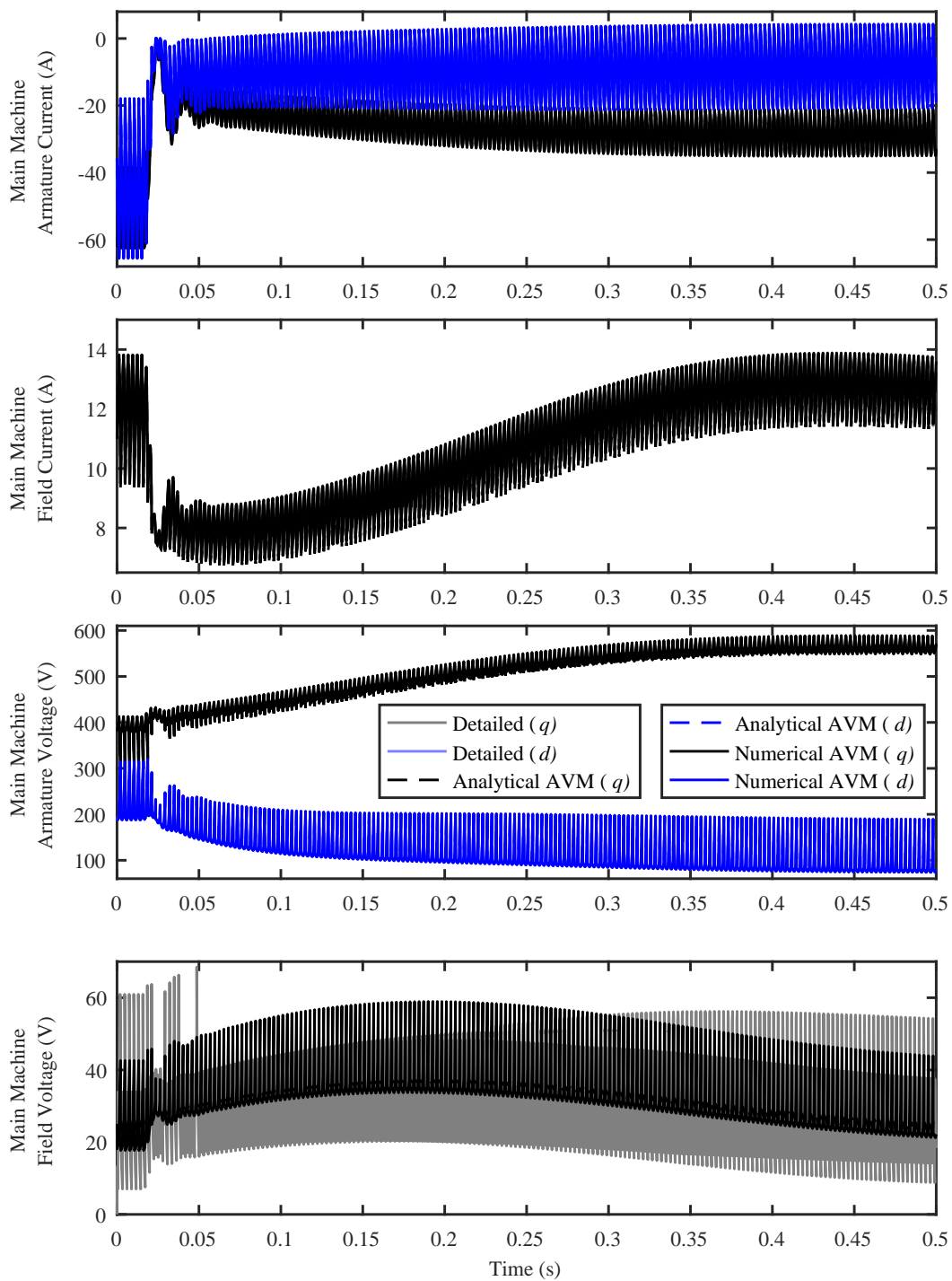


Figure 4.11: Case III (rectifier load step change) results.

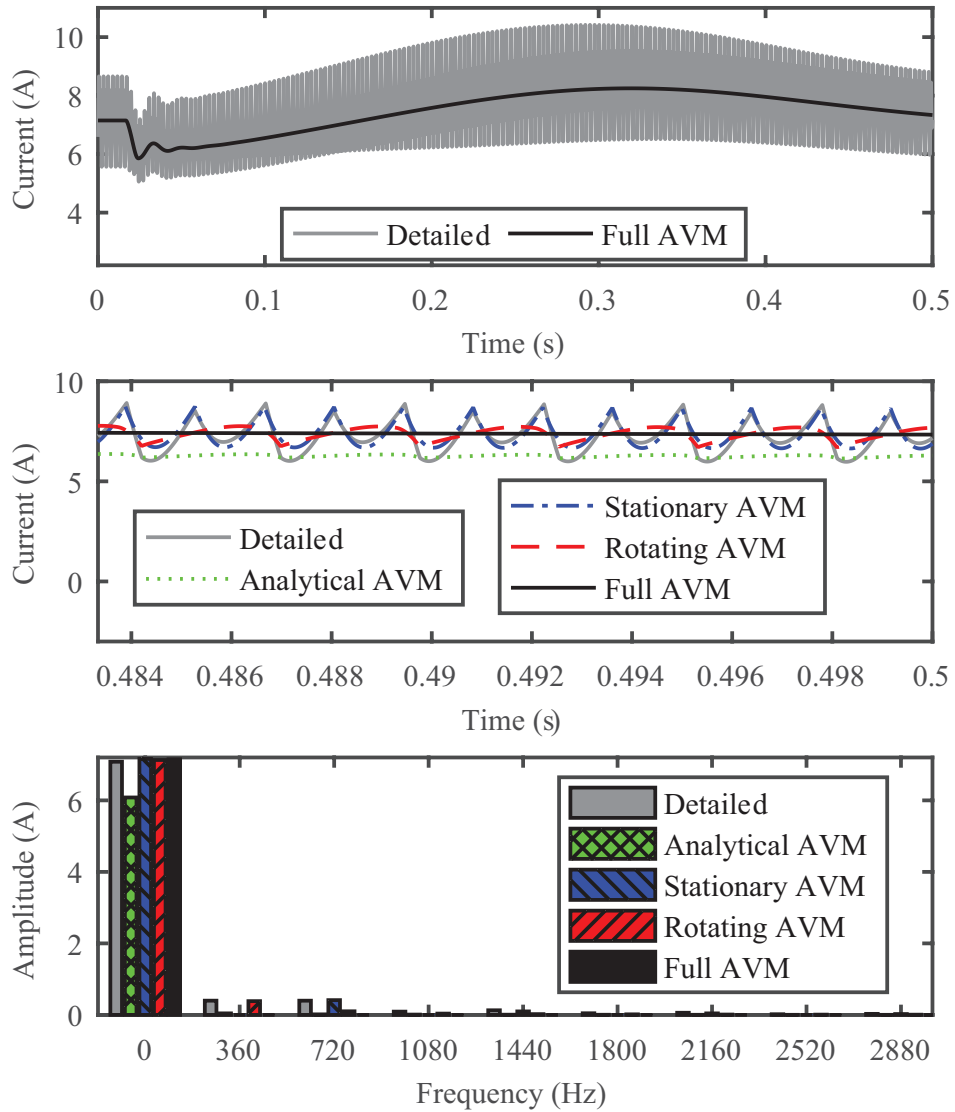


Figure 4.12: Case III (rectifier load step change) results (exciter armature q -axis current during transient and steady-state conditions and FFT results). The stationary, rotating, and full AVM each represent numerical AVMs.

Chapter 5

Formulation of Rectifier Numerical Average-Value Model for Direct Interface with Inductive Circuitry

The computational cost for the simulation of detailed models of machine-rectifier systems is expensive because of repetitive diodes switching. Average-value models (AVMs) of machine-rectifier systems have been developed that can alleviate the computational burden by neglecting the details of the switching of each individual diode while retaining the average characteristics. This paper proposes an alternative formulation of numerical AVMs of machine-rectifier systems, which makes direct use of the natural dynamic impedance of the rectifier without introducing low-frequency approximations or algebraic loops. By using this formulation, direct interface of the AVM is achieved with inductive circuitry on both the ac and dc sides allowing traditional voltage-in, current-out formulations of the circuitry on these sides to be used with the proposed formulation directly. This numerical AVM formulation is validated against an experimentally validated detailed model and compared with previous AVM formulations. It is demonstrated that the proposed AVM formulation accurately predicts the system's low-frequency behavior during both steady and transient states, including in cases where previous AVM formulations cannot predict accurate results. Both run times and numbers of time steps needed by the proposed AVM formulation are comparable to those of existing AVM formulations and significantly decreased compared with the detailed model.

The organization of this chapter is as below. Section 5.1 describes the proposed model, while Section 5.2 explains the rectifier characterization procedure. The model validation and comparison are presented in Section 5.3.

5.1 Average-Value Model of Machine-Rectifier Systems

An alternative approach for applying parametric or numerical AVMs is presented below that reformulates the relationships between variables on the ac and dc side of the rectifier to avoid introducing low-frequency approximations or inverting the voltage-current interfaces on either the ac or dc side, or creating algebraic loops.

5.1.1 Notation

Matrices and vectors are bold faced. The electrical angular speed and position of the machine are

$$\boldsymbol{\omega}_r = \frac{P}{2} \boldsymbol{\omega}_{rm} \quad (5.1)$$

$$\boldsymbol{\theta}_r = \frac{P}{2} \boldsymbol{\theta}_{rm}, \quad (5.2)$$

respectively, where $\boldsymbol{\omega}_{rm}$ and $\boldsymbol{\theta}_{rm}$ are the mechanical angular velocity and position of the machine, respectively, and P is the number of magnetic poles in the machine. The armature variables associated with a machine with a stationary armature can be expressed in vector form as $\mathbf{f}_{abc_s} = [f_{as} \ f_{bs} \ f_{cs}]^T$, where f may represent voltage (v), current (i), or flux linkage (λ). Such stationary armature variables are able to be transformed into the rotor reference frame [1] using

$$\mathbf{f}_{qd0s} = \mathbf{K}_s \mathbf{f}_{abc_s}, \quad (5.3)$$

where

$$\mathbf{K}_s = \frac{2}{3} \begin{bmatrix} \cos \boldsymbol{\theta}_r & \cos(\boldsymbol{\theta}_r - \frac{2\pi}{3}) & \cos(\boldsymbol{\theta}_r + \frac{2\pi}{3}) \\ \sin \boldsymbol{\theta}_r & \sin(\boldsymbol{\theta}_r - \frac{2\pi}{3}) & \sin(\boldsymbol{\theta}_r + \frac{2\pi}{3}) \\ \frac{1}{2} & \frac{1}{2} & \frac{1}{2} \end{bmatrix} \quad (5.4)$$

and $\mathbf{f}_{qd0s} = [f_{qs} \ f_{ds} \ f_{0s}]^T$ represents the q - and d -axis, and the zero-sequence components of the quantity. For systems considered herein, the zero-sequence component will be zero and can be ignored. Stationary variables transformed to the rotating reference frame are also able to be represented in space-phasor notation: $\vec{f}_{qds} = f_{qs} - jf_{ds}$.

The armature variables associated with a machine with a rotating armature are denoted $\mathbf{f}_{abcr} = [f_{ar} \ f_{br} \ f_{cr}]^T$. Such rotating armature variables are able to be transformed into the stationary reference frame using

$$\mathbf{f}_{qd0r} = \mathbf{K}_r \mathbf{f}_{abcr}, \quad (5.5)$$

where

$$\mathbf{K}_r = \frac{2}{3} \begin{bmatrix} \cos \theta_r & \cos(\theta_r + \frac{2\pi}{3}) & \cos(\theta_r - \frac{2\pi}{3}) \\ -\sin \theta_r & -\sin(\theta_r + \frac{2\pi}{3}) & -\sin(\theta_r - \frac{2\pi}{3}) \\ \frac{1}{2} & \frac{1}{2} & \frac{1}{2} \end{bmatrix} \quad (5.6)$$

and $\mathbf{f}_{qd0r} = [f_{qr} \ f_{dr} \ f_{0r}]^T$ represent the transformed variables. For systems considered herein, the zero-sequence component will be zero and can be ignored. Rotating armature variables transformed to the stationary reference frame are also able to be represented in space-phasor notation: $\vec{f}_{qdr} = f_{qr} + jf_{dr}$.

The operator p indicates the differentiation with respect to time, and $\|\cdot\|$ denotes the magnitude of a complex number or the 2-norm of a vector.

5.1.2 Rectifier relationships

The method presented for modeling the relationships in the rectifier shown in Figure 5.1 are based on [95] and [99]. In [95], the relationships that represent the average behavior of the stationary rectifier are:

$$\|\vec{v}\| = \alpha_s(z_s) v_{dc} \quad (5.7)$$

$$i_{dc} = \beta_s(z_s) \|\vec{i}\| \quad (5.8)$$

$$\angle \vec{v} = \angle \vec{i} + \phi_s(z_s) + \pi, \quad (5.9)$$

where \vec{v} and \vec{i} are the stationary armature variables on the ac side transformed to the rotating reference frame in space phasor form, $\alpha_s(\cdot)$, $\beta_s(\cdot)$, and $\phi_s(\cdot)$ are the essential numerical functions, π is the phase offset since the current \vec{i} is out of the rectifier, and z_s is a “conveniently defined” dynamic impedance, which is defined in [95] as

$$z_s = \frac{v_C}{\|\vec{i}\|}, \quad (5.10)$$

where v_C is the capacitor voltage of the LC filter. In [95], the dynamic impedance z_s was selected because v_C is a state variable and z_s is readily available in simulation.

For rotating rectifiers in brushless excitation systems, similar relationships to (5.7)–(5.9) are used in [99]. Because the main machine field winding is different from the LC filter and does not have a capacitor voltage, an alternative dynamic impedance is used:

$$z_r = \frac{\|\mathbf{e}_{qdr}\|}{i_{fdr}}, \quad (5.11)$$

where \mathbf{e}_{qdr} is the brushless exciter armature open-circuit voltages and i_{fdr} is the current into the main machine field winding.

The natural formulations of both the machine on the ac side and the inductor on the dc side in both cases would be a voltage-in, current-out formulation in which the rectifier model would input the ac and dc currents and calculate the ac and dc voltages. Such models involve proper state models, but they are not directly consistent with the relationships (5.7)–(5.9). To address the inconsistency, low-frequency approximations are introduced in both [95] and [99] to transform either the dc or ac model to a current-in, voltage-out formulation. It is argued, for example in [103], that such approximations do not significantly effect the behavior of the model.

The proposed reformulation of numerical AVMs for machine-rectifier systems uses similar relationships for the ac and dc voltages and currents. These relationships are modified in order to model rectifiers without using the low-pass filter [95, 96] and the differentiator approximation [99]. The relationships represent the average behavior of the rectifier

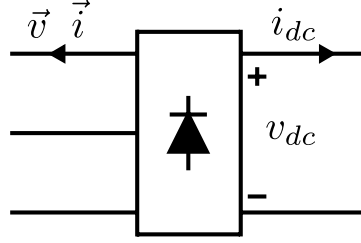


Figure 5.1: Rectifier.

shown in Figure 5.1 are:

$$\|\vec{v}\| = \alpha(z)v_{dc} \quad (5.12)$$

$$i_{dc} = \beta(z)\|\vec{i}\| \quad (5.13)$$

$$\angle\vec{v} = \angle\vec{i} + \phi(z) + \pi. \quad (5.14)$$

Instead of a “conveniently defined” dynamic impedance set some distance from the rectifier in [95, 96, 99], a natural dynamic impedance is employed:

$$z = \frac{v_{dc}}{\|\vec{i}\|}, \quad (5.15)$$

where v_{dc} is the terminal voltage of the rectifier. The proposed numerical AVM of machine-rectifier systems includes both stationary rectifiers and rotating rectifiers in the brushless excitation systems.

5.1.3 Model summary

The proposed AVM formulation is graphically described in Figure 5.2 and summarized in the steps below.

1. The input current of the rectifier $\|\vec{i}\|$ is calculated by the ac model. For the stationary rectifier, the ac model is the main machine armature. For the rotating rectifier, the ac model is the exciter armature.
2. The rectifier dc current i_{dc} is calculated by the dc model. For the stationary rectifier, i_{dc} is the filter current. For the rotating rectifier, i_{dc} is the main machine field current.

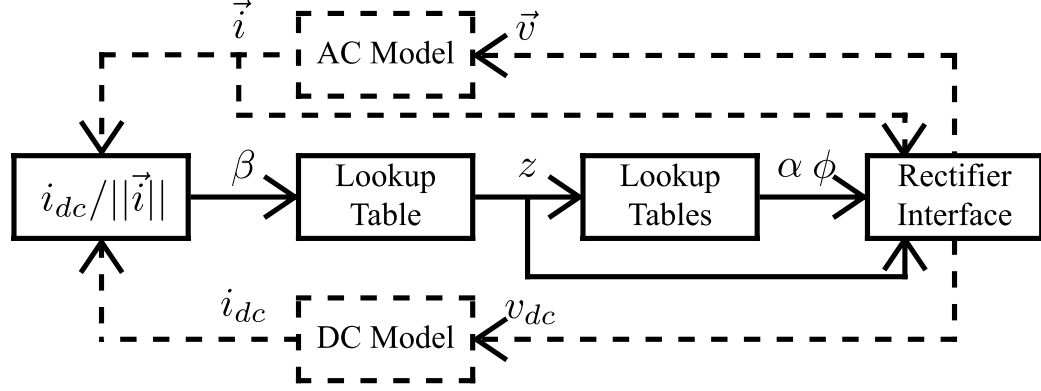


Figure 5.2: Summary of model formulation (dashed lines represent external interfaces from/to the proposed model).

3. The numerical function $\beta(\cdot)$ is calculated using (5.13).
4. The dynamic impedance z is obtained by inverting the numerical function $\beta(\cdot)$.
5. The numerical functions $\alpha(\cdot)$ and $\phi(\cdot)$ are obtained through lookup tables.
6. The magnitude $\|\vec{v}\|$ and angle $\angle\vec{v}$ of the ac voltage are calculated using (5.12) and (5.14), respectively, and the ac voltage \vec{v} is used in the ac model.
7. The rectifier dc voltage v_{dc} is calculated using (5.15) and used in the dc model.

5.2 Rectifier Characterization

The essential numerical functions $\alpha(\cdot)$, $\beta(\cdot)$, and $\phi(\cdot)$ are able to be extracted from the detailed simulations numerically, which has been discussed in [96]. Based on the assumption that algebraic relationships formulated by those functions are continuous, the rectifier characterization over a wide loading range can be done by transient simulations instead of repeated steady-state simulations. For both characterizations of stationary and rotating rectifiers, the ode23tb integration algorithm in MATLAB R2016a Simulink is used in the detailed simulations. The maximum time step is set to be 0.1 μ s. The values of relative and absolute tolerances are set to their default values. Automated State Model Genera-

tor (ASMG), which can automatically establish state-space models based upon topological states of the circuits, is used to represent circuit elements [102].

A four-pole synchronous generator rated for 59 kVA, 560 V at 1800 r/min is considered here as the main machine. Its model and parameters are adopted from studies in [64] and [58], and these models have been validated with multiple experimental measurements [63–65]. For the stationary rectifier characterization, the stator-only voltage-behind-reactance (SVBR) formulation [16] is used to model the main machine. The main machine is connected to a rectifier, which supplies a resistive load through an LC filter with a 2.5-mH inductance and a 1.4-mF capacitance. The resistive load exponentially increases from 0.01 Ω to 100 Ω in 1 s. The main machine field winding is connected to a 30-V voltage source. Initial conditions corresponding to a zero-flux state are selected. The resultant waveforms exhibit switching ripple at 360 Hz. The waveforms are averaged over 60-Hz windows every 1/360 s, and the values are plotted in Figure 5.3.

For the rotating rectifier characterization, the field-only voltage-behind-reactance (FVBR) formulation [16] is used to model the main machine. A balanced three-phase resistive load is connected to the main machine and draws rated power at rated voltage. The armature-only voltage-behind-reactance (AVBR) formulation of the exciter machine and its parameters are provided in [16]. Initial conditions corresponding to a zero-flux state are selected. The initial value of the exciter field voltage is -0.8 V. In the first 3.33 s, the exciter field voltage linearly increases to 8 V and then linearly decreases to the initial value in the next 3.33 s. The resultant waveforms exhibit switching ripple at 720 Hz. The waveforms are averaged over 60-Hz windows every 1/720 s, and the values are plotted in Figure 5.4.

Relatively few support points are selected using the least-squares spline approximation SPAP2 algorithm, and cubic splines can accurately represent these data as shown in Figure 5.3 and Figure 5.4. The support points for stationary and rotating rectifiers functions $\alpha(\cdot)$, $\beta(\cdot)$, and $\phi(\cdot)$ are found in Table 5.1 and Table 5.2, respectively.

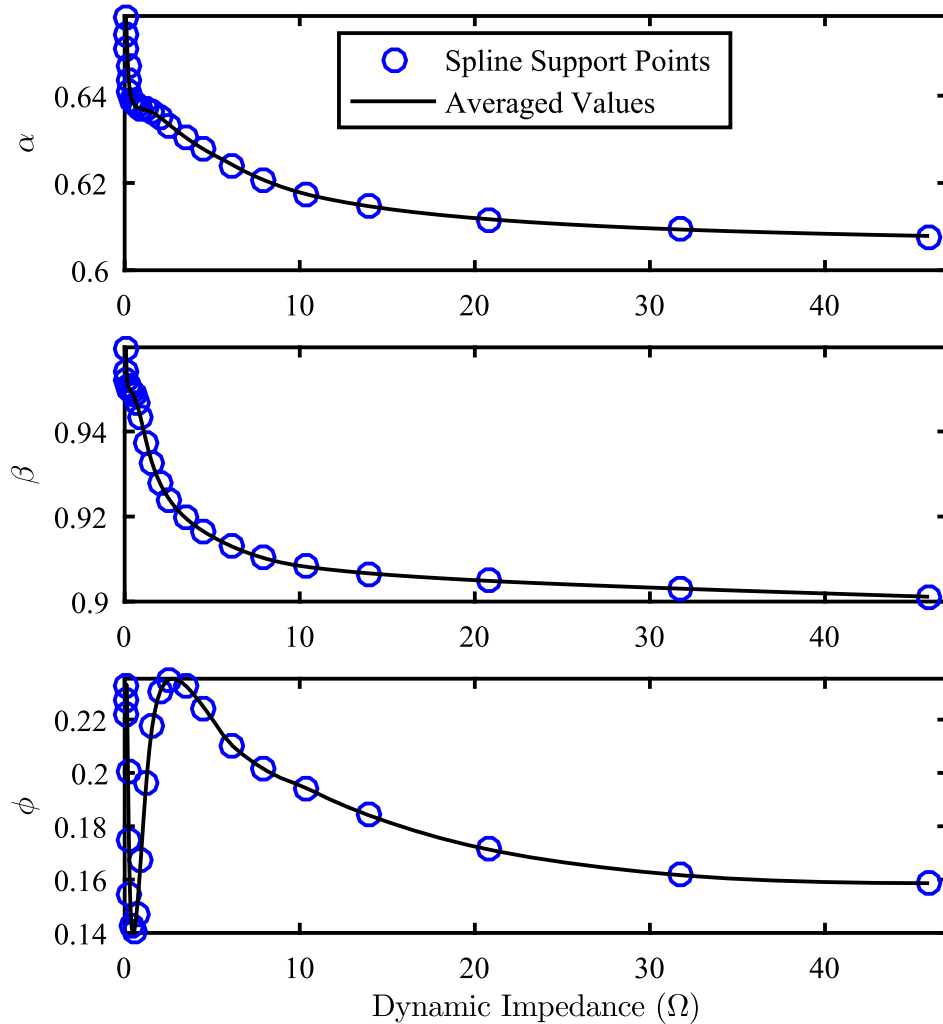


Figure 5.3: Stationary functions $\alpha(\cdot)$, $\beta(\cdot)$, and $\phi(\cdot)$.

5.3 Model Validation

The proposed AVM formulation of machine-rectifier systems is validated against the detailed model and compared with previous AVM formulations in this section. The ode23tb integration algorithm is adopted with the default absolute tolerance and the automatic maximum time step in MATLAB R2016a Simulink. The relative tolerance is set to be 10^{-6} . ASMG is used to represent circuit elements. Each simulation starts at steady state and lasts 1 s (60 cycles). The run time is averaged over 20 simulations for each model and case. A Dell Optiplex 7010 computer with an Intel Core i7-3770 3.40 GHz processor and 8.00 GB

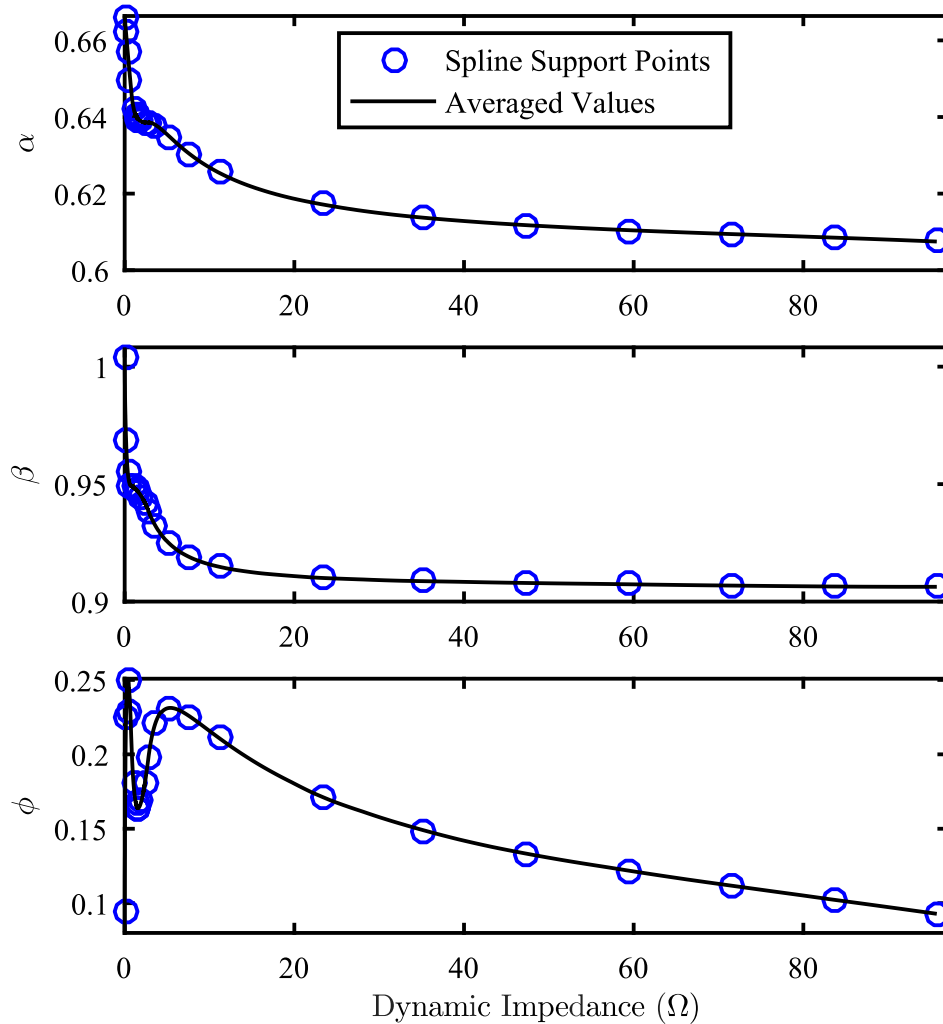


Figure 5.4: Rotating functions $\alpha(\cdot)$, $\beta(\cdot)$, and $\phi(\cdot)$.

of RAM is used to perform all the simulations.

5.3.1 Main machine and stationary rectifier load

In Case I, the main machine field winding is connected to a 25-V voltage source as shown in Figure 5.5. The stator is connected to a rectifier which feeds a 12 Ω resistive load via the *LC* filter. At $t = 1/60$ s, the excitation voltage is stepped up to 150% of the initial value. The SVBR formulation of the main machine and the detailed representation of the rectifier load are used in the detailed simulation. The *qd* formulation of the main machine and the previous AVM formulation of the stationary rectifier are adopted with a current-in,

Table 5.1: Support Points for Stationary Rectifier Functions $\alpha(\cdot)$, $\beta(\cdot)$, and $\phi(\cdot)$

z (Ω)	α	β	ϕ
0.075	0.658	0.960	0.228
0.115	0.654	0.954	0.233
0.149	0.651	0.952	0.222
0.189	0.647	0.951	0.201
0.241	0.644	0.950	0.175
0.309	0.641	0.950	0.154
0.396	0.639	0.949	0.143
0.507	0.638	0.949	0.140
0.675	0.638	0.947	0.147
0.922	0.637	0.943	0.168
1.233	0.637	0.938	0.196
1.579	0.636	0.933	0.218
2.012	0.635	0.928	0.230
2.597	0.633	0.924	0.235
3.433	0.631	0.920	0.233
4.564	0.628	0.916	0.224
6.116	0.624	0.913	0.211
7.962	0.621	0.910	0.202
10.413	0.617	0.908	0.194
13.990	0.615	0.907	0.184
20.801	0.612	0.905	0.171
31.760	0.609	0.903	0.162
45.949	0.608	0.901	0.159

voltage-out formulation of the LC filter in the previous AVM simulation. The inductor in the LC filter operates as a differentiator with an improper transfer function. This improper transfer function is represented with a low-frequency approximation, and the time constant associated with the approximation is set to be 10 μ s [95]. The qd formulation of the main machine and the proposed AVM formulation of the rectifier are used in the proposed AVM simulation. In all cases, the time steps and the run times are listed in Table 5.3. Figure 5.6 shows the armature voltages and currents and the field current of the main machine. The main machine's low-frequency behavior is accurately represented by both the previous and proposed AVMs in this case. Both sets of waveforms predicted by the AVMs are essentially identical and follow the tendency of detailed model waveforms. Furthermore, it can be seen

Table 5.2: Support Points for Rotating Rectifier Functions $\alpha(\cdot)$, $\beta(\cdot)$, and $\phi(\cdot)$

z (Ω)	α	β	ϕ
0.000	0.666	1.003	0.094
0.163	0.662	0.969	0.224
0.352	0.657	0.956	0.251
0.653	0.650	0.950	0.229
1.032	0.643	0.949	0.181
1.360	0.640	0.948	0.167
1.477	0.640	0.947	0.164
1.542	0.640	0.947	0.164
1.625	0.639	0.947	0.164
1.951	0.639	0.945	0.169
2.368	0.639	0.942	0.180
2.795	0.639	0.939	0.198
3.603	0.638	0.932	0.221
5.232	0.635	0.925	0.231
7.684	0.630	0.919	0.225
11.172	0.625	0.915	0.211
23.252	0.617	0.910	0.172
35.332	0.614	0.909	0.149
47.411	0.612	0.908	0.133
59.491	0.610	0.907	0.122
71.571	0.609	0.907	0.112
83.651	0.609	0.906	0.102
95.731	0.608	0.906	0.093

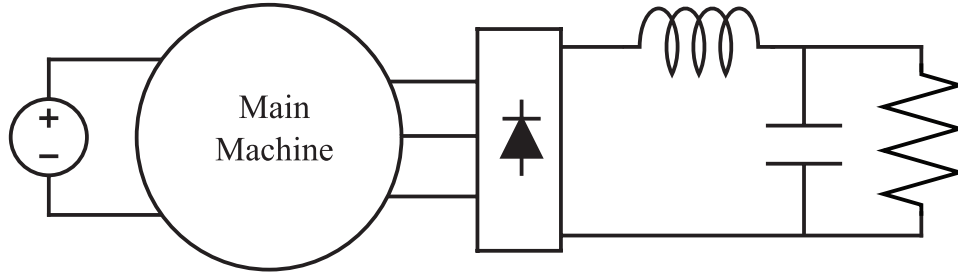


Figure 5.5: Case I and Case II arrangement.

in Table 5.3, both the run time and the number of time steps required by the proposed AVM are comparable with those required for the previous AVM. The run time are reduced by 97%, and the number of time steps is reduced by 99% compared with the detailed model.

The same excitation of the main machine, rectifier load and initial conditions used in

Table 5.3: Model Computational Efficiency

Case	Simulation	Time steps	Run time (s)
Case I	Detailed	337978	7.62
	Previous AVM	3959	0.23
	Proposed AVM	3999	0.23
Case II	Detailed	67182	1.70
	Previous AVM	6661	0.26
	Proposed AVM	5258	0.25
Case III	Detailed	293059	7.36
	Previous AVM	3805	0.26
	Proposed AVM	4108	0.24
Case IV	Detailed	244518	5.82
	Previous AVM	6141	0.28
	Proposed AVM	7361	0.25
Case V	Detailed	372815	16.40
	Previous AVM	2710	0.26
	Proposed AVM	2548	0.24
Case VI	Detailed	246953	10.59
	Previous AVM	8947	0.35
	Proposed AVM	8716	0.32

Case I are used in Case II as shown in Figure 5.5. At $t = 1/60$ s, a bolted fault across the capacitor occurs at the dc side. For Case II, the same machine formulations and rectifier representations as in Case I are used in the detailed simulation and AVM simulations. Figure 5.7 shows the comparisons of the waveforms obtained from the proposed AVM, the previous AVM, and the detailed model. One can find that resultant waveforms from the proposed AVM follow the overall tendency of the waveforms obtained from the detailed model. It can be concluded that the proposed AVM is capable of representing the system's low-frequency responses. In contrast, it can be observed that the previous AVM exhibits significant deviations from the behavior predicted by the detailed model during the transition. The cause of these deviations is the use of different dynamic impedances and the introduction of low-frequency approximations in the previous AVM. As can be seen in Table 5.3, the computational cost, i.e., the run time and the number of time steps, of the proposed AVM is slightly less than that of the previous AVM. The run time and the number of time steps are reduced by 85% and 92% compared with the detailed model, respectively.

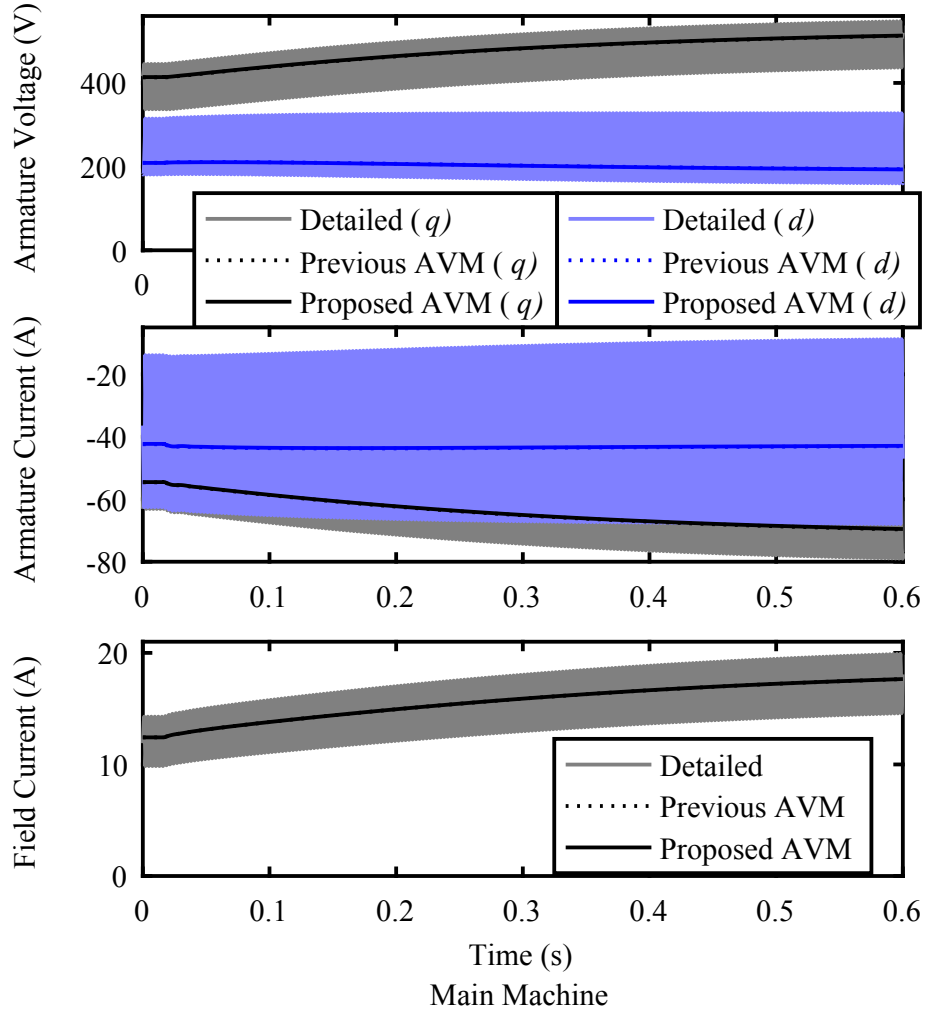


Figure 5.6: Case I (excitation voltage step change) results.

The computational cost of the detailed model in Case II is lower than in Case I because the dc fault causes the rectifier diodes to stop switching on and off.

5.3.2 Exciter, rotating rectifier, main machine, and infinite bus

In Case III, the field winding of the main machine is connected to a rotating rectifier, which is fed by an exciter with 7.5-V field voltage as shown in Figure 5.8. The stator is used to supply power to an infinite 560-V bus. The rotor angle of the machine is $\pi/8$ rad. At $t = 1/60$ s, the rotor speed linearly increases from 1800 r/min to 1912.5 r/min over $1/120$ s and then linearly decreases back to the original value over $1/120$ s. As a consequence,

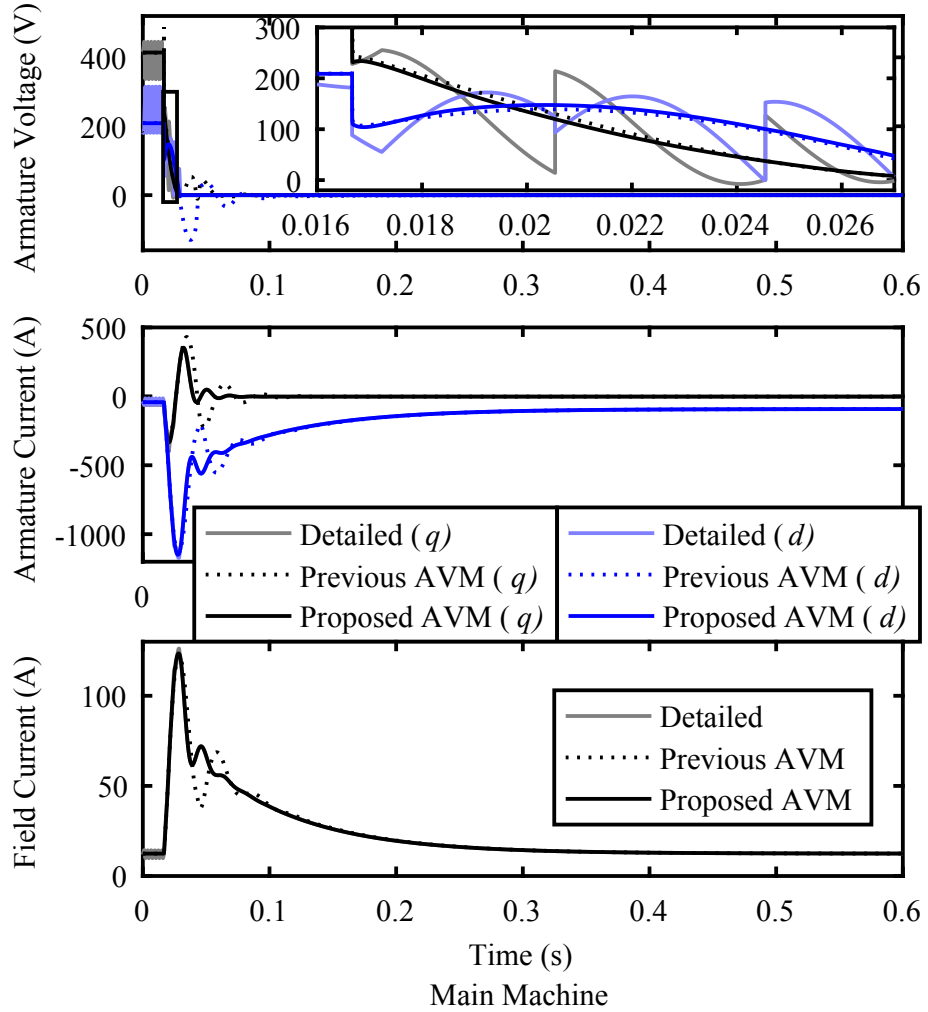


Figure 5.7: Case II (dc fault) results.

the rotor angle increases to $3\pi/16$ rad. The FVBR formulation of the main machine, the armature-only voltage-behind-reactance (AVBR) formulation of the brushless exciter machine presented in [16] and the detailed representation of the rotating rectifier are used in the detailed simulation. The qd formulation of the main machine, the previous AVM formulation of the exciter machine and rotating rectifier presented in [99] are used in the previous AVM simulation. The exciter machine is represented using a low-frequency approximation described in [99] with poles located at -1.4×10^5 rad/s and -0.7×10^5 rad/s. The qd formulation of the main machine, the qd formulation of the exciter and the proposed AVM formulation of the rectifier are used in the proposed AVM simulation. Fig-

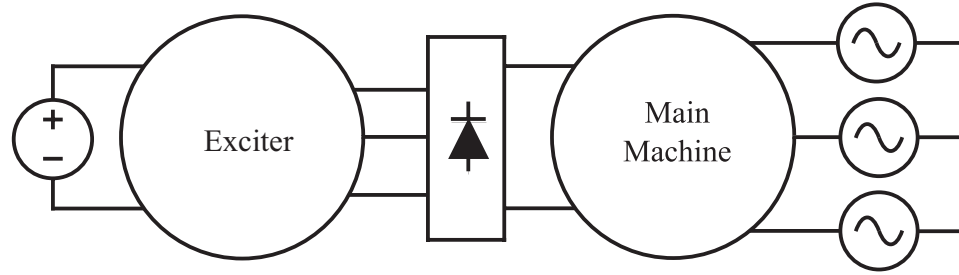


Figure 5.8: Case III and Case IV arrangement.

Figure 5.9 shows the armature currents and the field voltage and current of the main machine. The waveforms are predicted accurately by the proposed AVM even when the rotor speed changes significantly. In contrast, there are significant deviations exhibited in the previous AVM waveforms from the detailed model waveforms and the proposed AVM waveforms during the transient state in this case. Comparing the computational cost with the previous AVM shown in Table 5.3, though the number of time steps is slightly greater, the run time is slightly smaller. The run time and the number of time steps are reduced by 97% and 99% compared with the detailed model, respectively.

The same arrangement of the exciter, rotating rectifier, main machine, infinite 560-V bus and initial conditions used in Case III are used in Case IV as shown in Figure 5.8. At $1/60$ s, a three-phase bolted fault occurs at the ac side, i.e., the armature voltages of the main machine are stepped down to 0 V. Case IV uses the same rectifier representations and machine formulations for the detailed and AVM simulations as Case III. Figure 5.10 shows the armature voltages and currents and the field current of the exciter machine. It shows that the waveforms obtained from the proposed AVM follow the waveforms obtained from the detailed model very well, but the previous AVM cannot capture the rapid decline of the voltages or the low-frequency oscillations observed in the currents. From Table 5.3, it can be seen that the proposed AVM again has comparable number of time steps and run time with the previous AVM. The run time is reduced by 96%, and the number of time steps is reduced by 97% compared with the detailed model.

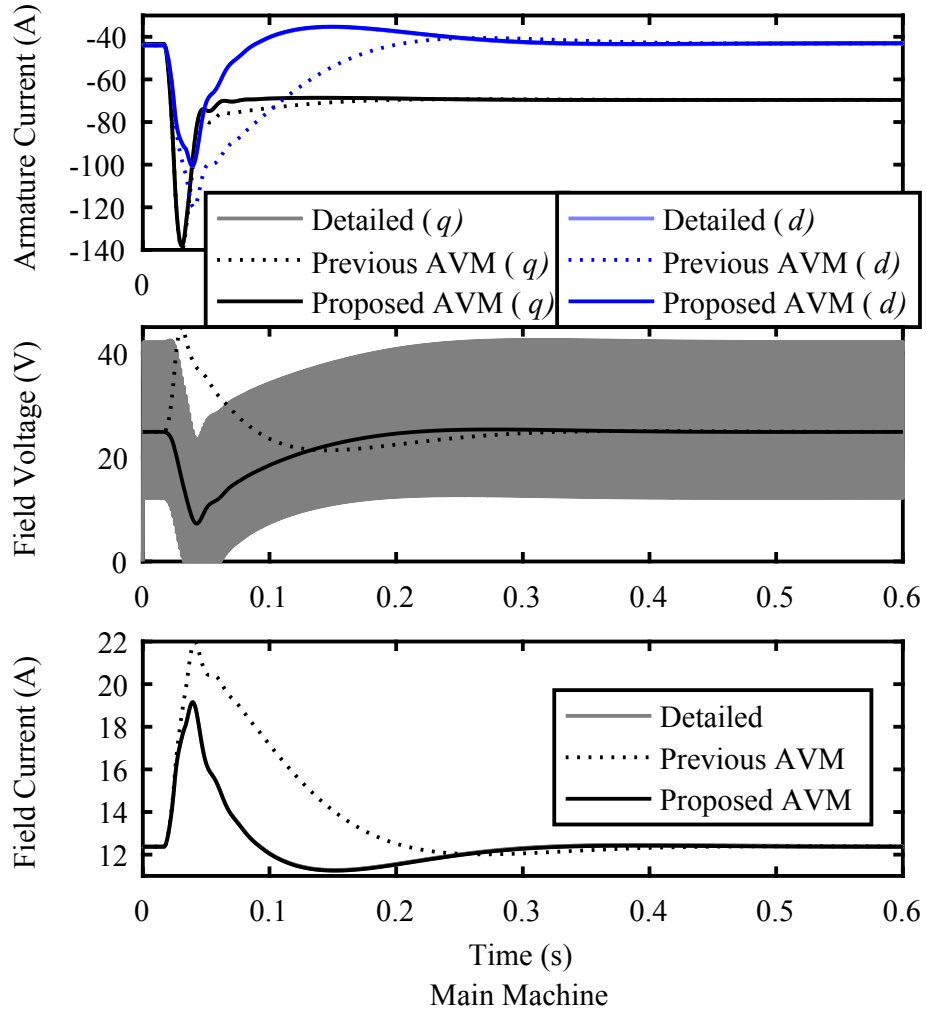


Figure 5.9: Case III (rotor angle change) results.

5.3.3 Exciter, rotating Rectifier, main machine, and stationary rectifier load

In Case V, the field winding of the main machine is connected to a rotating rectifier, which is fed by an exciter with 7.5-V field voltage shown in Figure 5.11. The stator is connected to a rectifier which feeds a 12Ω resistive load via an LC filter. At $1/60$ s, the excitation voltage of the exciter drops to 6 V. The SFVBR formulation of the main machine, the detailed representation of the rectifier load, the AVBR formulation of the brushless exciter machine, and the detailed representation of the rotating rectifier are use in the detailed sim-

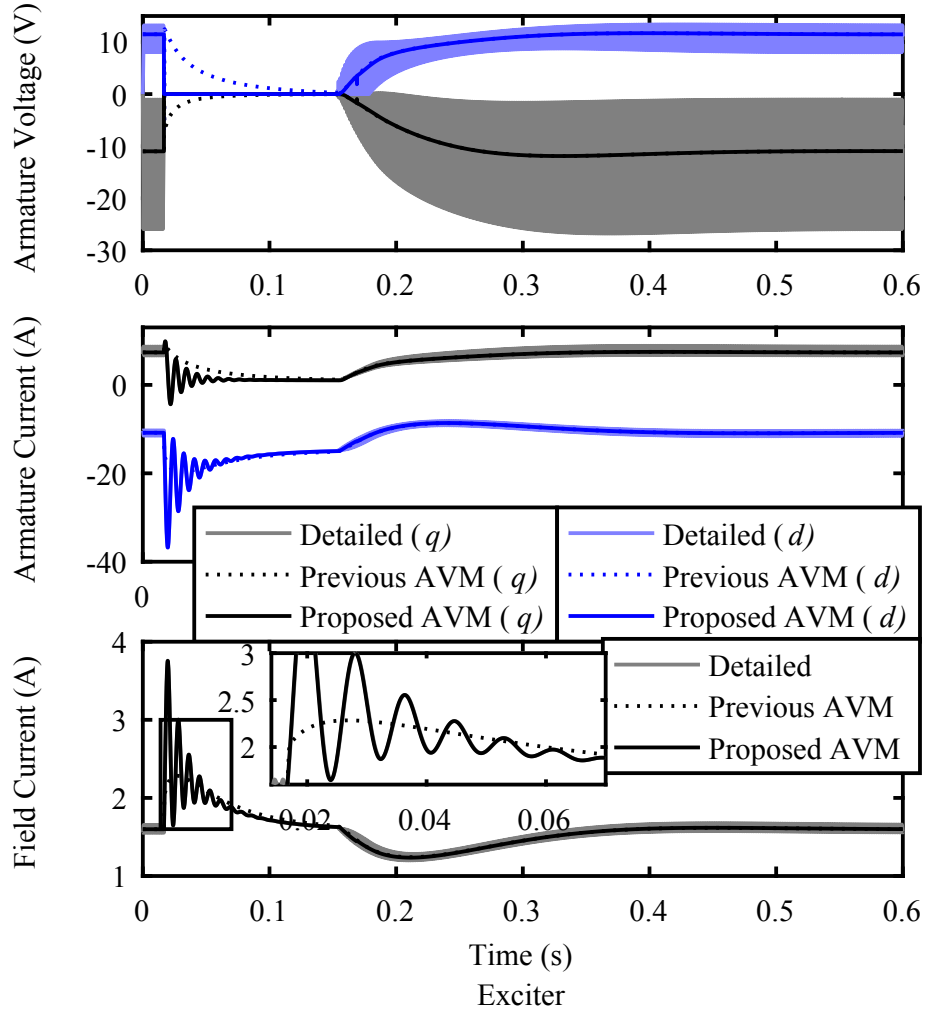


Figure 5.10: Case IV (ac fault) results.

ulation. The qd formulation of the main machine, the previous AVM formulation of the stationary rectifier presented in [95], and the previous AVM formulation of the exciter machine and rotating rectifier presented in [16] are used in the previous AVM simulation. The qd formulations of the main and exciter machines, the proposed AVM formulations of the stationary and rotating rectifiers are used in the proposed AVM simulation. The armature voltages and currents and the field current of the exciter machine are plotted in Figure 5.12. As with Case I, the figure shows that the waveforms obtained from the proposed AVM are identical to the waveforms obtained from the previous AVM and faithfully follow the trace predicted by the detailed model. The proposed AVM performs similarly to the previous

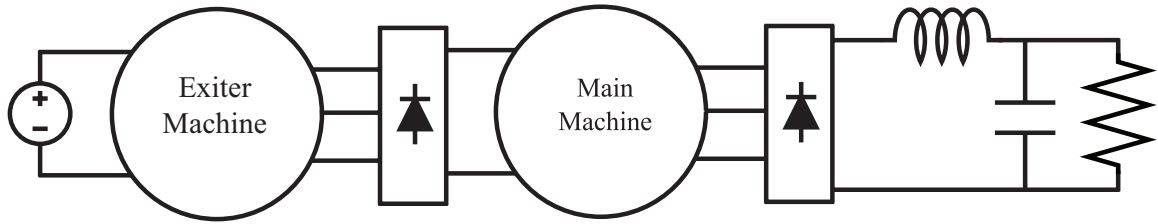


Figure 5.11: Case V and Case VI arrangement.

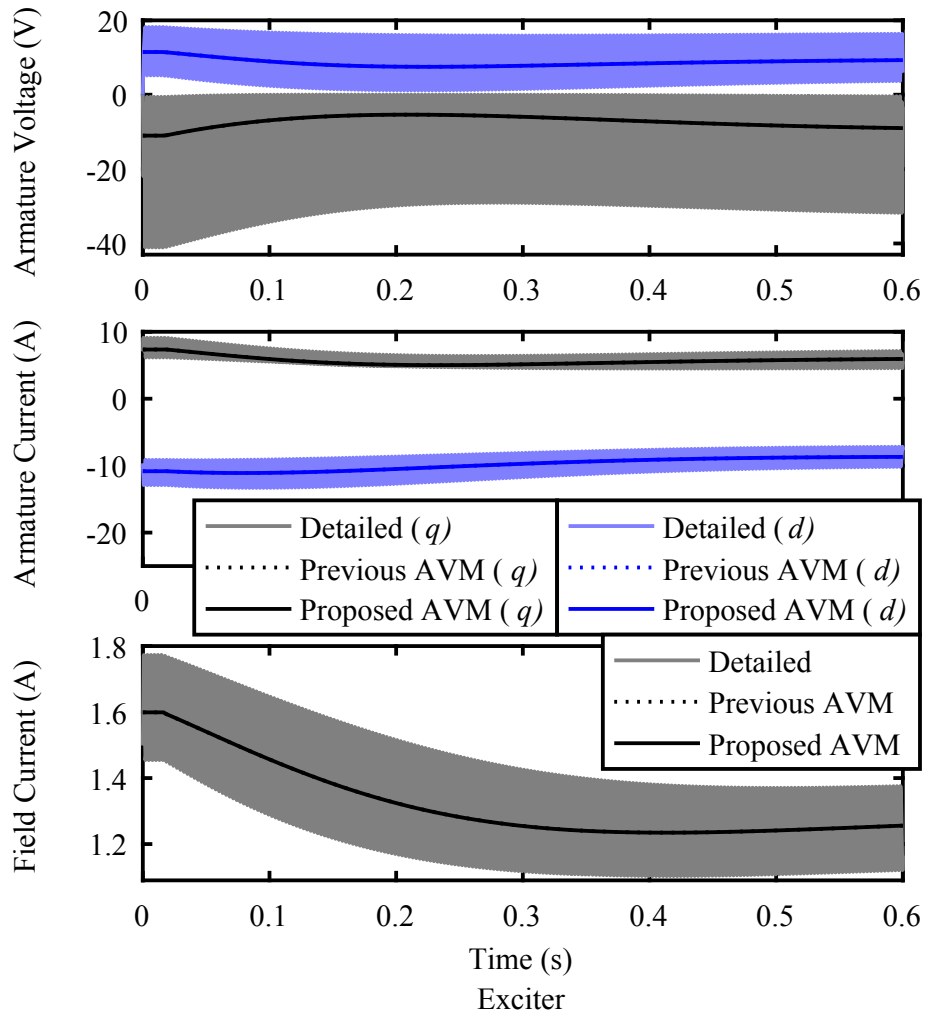


Figure 5.12: Case V (excitation voltage step change) results.

AVM and significantly improves the computational efficiency with respect to the detailed model as shown in Table 5.3. Both the run time and the number of time steps required by the proposed AVM are reduced by 99% compared with the detailed model.

The same arrangement of the exciter, rotating rectifier, main machine, stationary recti-

fier load and initial conditions used in Case V are used in Case VI as shown in Figure 5.11. At $t = 1/60$ s, a bolted fault across the capacitor occurs at the dc side. Case VI uses the same machine formulations and rectifier representations as in Case V in the detailed and AVM simulations. Figure 5.13 shows the field voltage and the output voltage and current of the main machine. It is shown that the waveforms obtained from the proposed AVM follow the waveforms obtained from the detailed model very well. It is also shown in Figure 5.13 that the previous AVM had significant discrepancies on the dc side of the stationary rectifier. The waveforms shown in Figure 5.7 for Case II are not shown for this case, but the previous AVM also demonstrated the same discrepancies in this case. As with the other cases, it can be seen in Table 5.3 that the proposed AVM has a comparable computational cost with the previous AVM and that its computational costs are much smaller than those associated with the detailed model. The run time and the number of time steps are reduced by 97% and 96% compared with the detailed model, respectively.

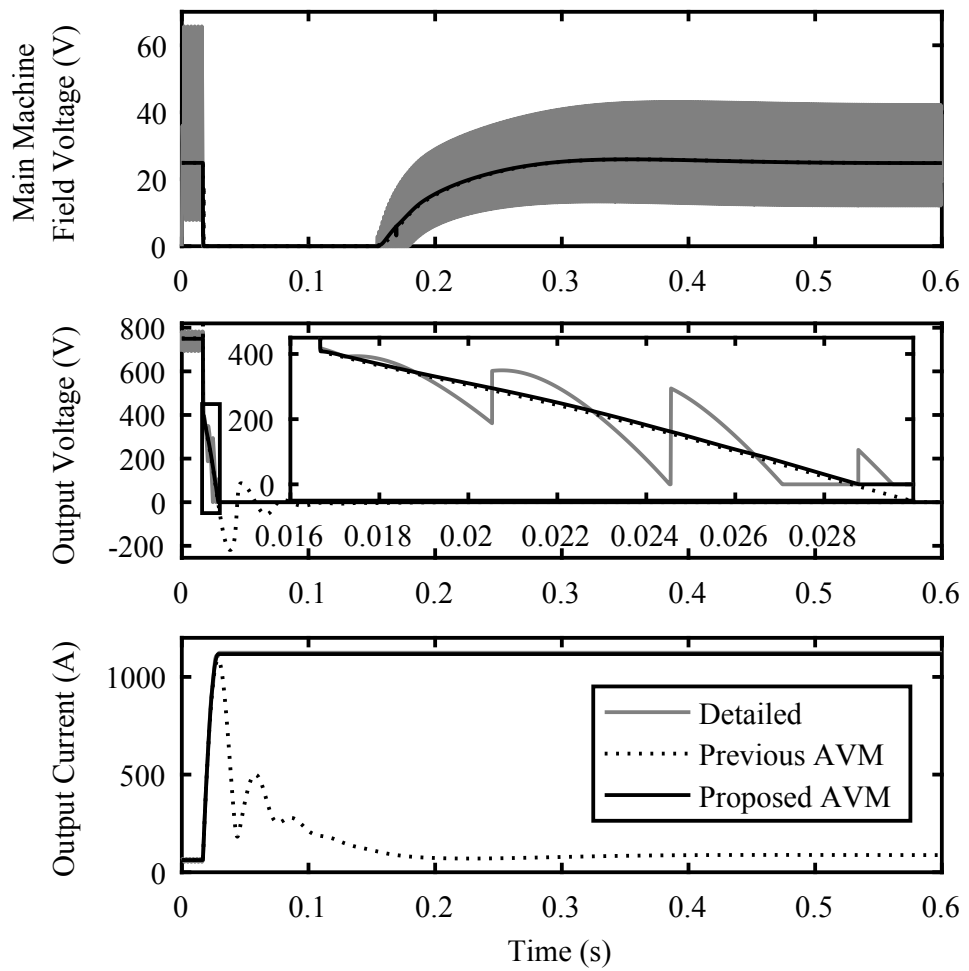


Figure 5.13: Case VI (dc fault) results.

Chapter 6

Conclusion and Future Work

6.1 Conclusion

The derivation of various formulations of a synchronous machine model that includes arbitrary linear networks to represent rotor circuits and magnetizing path saturation including cross-saturation has been unified. This machine model is significant because it has been extensively experimentally validated and includes most existing machine models as special cases. An FVBR formulation of this model has been derived as well. The benefits in terms of run time and accuracy of each formulation have been examined. In particular, it has been found that the formulation with the most conducive interface for the simulation application produces more accurate results with fewer required time steps and less run time but that having a suitable stator interface is particularly important.

A numerical AVM for rotating rectifiers in brushless excitation systems is developed, wherein open-circuit voltages of the brushless exciter armature are used to calculate the dynamic impedance that represents the loading condition. This model averages the periodic switching behavior of the rotating rectifier. Numerical functions describing relationships between averaged dc variables and exciter ac variables in rotating rectifiers are extracted from detailed simulations and vary depending on the loading conditions. The proposed AVM model is validated with the detailed model and compared with an analytical AVM model. It is shown to accurately represent the low-frequency behavior of the system and to have high computational efficiency.

An alternative formulation of numerical AVMs of machine-rectifier systems is proposed, which can directly interface with branches on the ac and dc sides of the rectifier without introducing low-frequency approximations or algebraic loops. The key numerical functions are similar to those used in previous AVM formulations and are extracted from detailed simulations over varying loading conditions. The natural dynamic impedance of the rectifier, calculated using the terminal quantities of the rectifier, is directly used without introducing low-frequency approximations or algebraic loops. The proposed AVM formulation, which encompasses both stationary rectifiers and rotating rectifiers in brushless excitation systems, does not require inversion of voltage-current interfaces on either the ac or dc side and can be directly interfaced with simulation models with traditional voltage-in, current-out formulations of the ac and dc equipment. This AVM formulation is validated against the detailed model and compared with previous AVM formulations in six distinct cases. The proposed AVM formulation is shown to be accurate in providing simulations during both steady and transient states, including in cases where previous AVM formulations do not accurately predict the waveforms, while retaining the computational cost advantages of existing AVM formulations over detailed models.

The parametric or numerical approach has been extended in numerous ways (e.g., ac harmonics and frequency dependency for thyristor-controlled rectifiers are considered in [100]). The fundamental approach is the same, based on numerical averaging of the results of detailed simulations in order to establish a numerical representation of the relationship between the ac and dc variables.

6.2 Future Work

Modeling of synchronous machines has been an intensive study area for decades for various purposes in either industry or academic applications. Most of the current models can be generally traced back to phase domain (PD) models in the phase coordinate frame and qd -models in the rotating qd -coordinates frame. To improve the modeling accuracy and

numerical efficiency, the so-called voltage-behind-reactance (VBR) modeling has been recently proposed. Although the PD models and the VBR models can provide a direct interface with the external electrical network, these models are presented by rotor-position-dependent parameters (inductances). The fundamental machine parameters are expressed in terms of physical variables and the measured time constants. A constant-parameter decoupled RL -branch equivalent circuit, which can achieve a direct and explicit interface of ac machines, is proposed in [74]. It is based on the voltage-behind-reactance formulation. However, the effect of magnetic saturation has not been considered in [74]. In order to improve the accuracy of modeling synchronous machines, it is desirable to include the effect of magnetic saturation. The previous research can be extended to include magnetic saturation into the constant-parameter equivalent circuit for synchronous machines, which will take in to account the axes static and dynamic cross saturation. By adding a set of fixed winding parameters in addition to the VBR model, the synchronous machine with saturation can be represented by a constant-parameters equivalent circuit.

Depending on the objectives of studies and required accuracy, the modeling approaches for synchronous machine with saturation may be roughly divided into three categories: finite element method [104], equivalent magnetic circuit approach [68,69], and magnetically coupled electric circuit approach. This chapter mainly focuses on general-purpose models that are based on the last approach, which leads to a relatively small number of equations and has been very often utilized for predicting the dynamic responses of electrical machines in power system operations. To further simplify the coupled electric circuit approach, the machine physical variables are often transformed into quadrature and direct magnetic rotor axes [10, 13]. This approach is also known as the modeling of rotating machines, which is widely used in Electromagnetic Transient Programs (EMTP) [14] for power system transient simulations and analyses.

For synchronous machines, if $L''_{mq} = L''_{md}$, the terms inside the subtransient inductance matrix will be constant. An artificial damper winding is added to the rotor circuit in order to

enforce the numerical equality of L''_{mq} and L''_{md} . Since the subtransient inductance in the d-axis is typically smaller, the additional winding is normally added to the q-axis equivalent circuit. Therefore, $L_S(\cdot)$ and $L_M(\cdot)$ are constant as $L_S = L_{ls} + \frac{2}{3}L''_{md}$, $L_M = -\frac{1}{3}L''_{md}$. The off-diagonal elements of the constant matrix are eliminated by incorporating zero-sequence current into the voltage equation for the stator branches. A fourth branch, which is the zero-sequence branch, is defined by the voltage equation $v_{ng} = L_0 p(3i_{0s}) = L_0 p i_{ng}$. Finally, the four constant and decoupled RL -branches are defined [74]. Combined with the VBR model, the magnetic saturation will be considered to merge into the proposed constant-parameters circuit for synchronous machines.

Synchronous machines are very important and useful machinery in power systems. Modeling synchronous machines can achieve further insight in the complex electro-magnetic behavior of the machine, as well as power systems simulation and analyses. The objectives of this work are: to formulate a numerical average-value model (AVM) for machine-rectifier systems to simplify machine-rectifier interfaces issues and improve accuracy; to evaluate the alternative formulation of numerical AVMs of machine-rectifier Systems performance. In this work, derivations of the standard voltage-in, current-out formulation as well as formulations in which the stator and/or the field windings are represented in a voltage-behind-reactance (VBR) form are presented in a unified manner, including the derivation of a field-only voltage-behind-reactance formulation. It has been demonstrated that selection of the formulation with the most suitable interface for the simulation scenario has better accuracy and less run time. This work develops a numerical average-value model of machine-rectifier systems, which encompasses both stationary rectifiers and rotating rectifiers in brushless excitation systems. Furthermore, numerical AVMs of machine-rectifier systems are reformulated so that it does not require inversion of the voltage-current interfaces on either the ac or dc side and can be simply incorporated in simulation models with traditional voltage-in, current-out formulations on both the ac and dc sides. Advanced synchronous machine modeling can be extended to different applications. For example, it can

be used in observer-based fault detection and isolation, and generator protection. Different spine functions can be extracted, via numerical averaging, from the behaviors of systems, which include systems without any faults and systems with different kinds of faults. Those functions can further form a database, with the purpose of diagnosis of potential faults from any system by comparing its spine functions with those in the database. Through matching the functions, the nature of fault(s), if any, in the system can not only be identified, but the location of fault(s) may also be found.

Bibliography

- [1] P. Krause, O. Wasynczuk, S. Sudhoff, and S. Pekarek, *Analysis of Electric Machinery and Drive Systems*, 3rd ed. Piscataway, NJ: Wiley-IEEE Press, 2013.
- [2] G. Grater and T. Doyle, “Propulsion powered electric guns—a comparison of power system architectures,” *IEEE Trans. Magn.*, vol. 29, no. 1, pp. 963–968, Jan. 1993.
- [3] J. M. Carrasco, L. G. Franquelo, J. T. Bialasiewicz, E. Galvan, R. C. PortilloGuisado, M. A. M. Prats, J. I. Leon, and N. Moreno-Alfonso, “Power-electronic systems for the grid integration of renewable energy sources: A survey,” *IEEE Transactions on Industrial Electronics*, vol. 53, no. 4, pp. 1002–1016, Jun. 2006.
- [4] E. Mouni, S. Tnani, and G. Champenois, “Synchronous generator output voltage real-time feedback control via h_∞ strategy,” *IEEE Trans. Energy Convers.*, vol. 24, no. 2, pp. 329–337, Jun. 2009.
- [5] D. S. O. Jr., M. M. Reis, C. E. A. Silva, L. H. S. C. Barreto, F. L. M. Antunes, and B. L. Soares, “A three-phase high-frequency semicontrolled rectifier for pm wecs,” *IEEE Transactions on Power Electronics*, vol. 25, no. 3, pp. 677–685, Mar. 2010.
- [6] Z. Bingyi, S. Shaonan, F. Guihong, and G. Xin, “A switchable cascaded multi-dc-branch for permanent magnet synchronous generator in wide speed range on wind energy conversion system,” in *2017 IEEE 12th International Conference on Power Electronics and Drive Systems (PEDS)*, Dec. 2017, pp. 131–135.
- [7] T. Noguchi, Y. Kurebayashi, T. Osakabe, and T. Takagi, “Development of high-efficiency permanent magnet synchronous generator for motorcycle application,” in *2017 IEEE 12th International Conference on Power Electronics and Drive Systems (PEDS)*, Dec. 2017, pp. 769–774.
- [8] M. M. Ostojić and M. B. Djurić, “Out-of-step protection of synchronous generators based on a digital phase comparison in the time domain,” *IET Generation, Transmission Distribution*, vol. 12, no. 4, pp. 873–879, Feb. 2018.
- [9] N. A. E. R. Council, *Reliability Concepts in Bulk Power Electric Systems*. Princeton, NJ: North American Electric Reliability Council, 1985.
- [10] B. Stott, O. Alsac, and A. Monticelli, “Security analysis and optimization,” *Proceedings of the IEEE*, vol. 75, no. 12, pp. 1623–1644, Dec. 1987.

- [11] N. Balu, T. Bertram, A. Bose, V. Brandwajn, G. Cauley, D. Curtice, A. Fouad, L. Fink, M. Lauby, B. Wollenberg, and J. N. Wrubel, "On-line power system security analysis," *Proceedings of the IEEE*, vol. 80, no. 2, pp. 262–282, Feb. 1992.
- [12] S. Racewicz, D. Riu, N. Retiere, and P. Chzran, "Non linear half-order modeling of synchronous machine," in *IEEE International Electric Machines and Drives Conference(IEMDC)*, May 2009, pp. 778–783.
- [13] A. Kumar, S. Marwaha, A. Singh, and A. Marwaha, "Performance investigation of a permanent magnet generator," *Simulation Modelling Practice and Theory*, vol. 17, no. 10, pp. 1548–1554, Nov. 2009.
- [14] S. Maiti, C. Chakraborty, and S. Sengupta, "Simulation studies on model reference adaptive controller based speed estimation technique for the vector controlled permanent magnet synchronous motor drive," *Simulation Modelling Practice and Theory*, vol. 17, no. 4, pp. 585–596, Apr. 2009.
- [15] R. H. Park, "Two-reaction theory of synchronous machines generalized method of analysis-Part I," *Trans. AIEE*, vol. 48, no. 3, pp. 716–727, Jul. 1929.
- [16] Y. Zhang and A. M. Cramer, "Unified model formulations for synchronous machine model with saturation and arbitrary rotor network representation," *IEEE Trans. Energy Convers.*, vol. 31, no. 4, pp. 1356–1365, Dec. 2016.
- [17] J. G. Kettleborough, I. R. Smith, and B. A. Fanthome, "Simulation of a dedicated aircraft generator supplying a heavy rectified load," *IEE Proc. B, Electr. Power Appl.*, vol. 130, no. 6, pp. 431–435, Nov. 1983.
- [18] T. H. Warner and J. G. Kassakian, "Transient characteristics and modeling of large turboalternator driven rectifier/inverter systems based on field test data," *IEEE Power Eng. Rev.*, vol. PER-5, no. 7, pp. 47–47, Jul. 1985.
- [19] I. Jadrić, D. Borojević, and M. Jadrić, "Modeling and control of a synchronous generator with an active dc load," *IEEE Trans. Power Electron.*, vol. 15, no. 2, pp. 303–311, Mar. 2000.
- [20] J. G. Ciezki and R. W. Ashton, "Selection and stability issues associated with a navy shipboard dc zonal electric distribution system," *IEEE Trans. Power Del.*, vol. 15, no. 2, pp. 665–669, Apr. 2000.
- [21] J. Rivas, D. Perreault, and T. Keim, "Performance improvement of alternators with switched-mode rectifiers," *IEEE Trans. Energy Convers.*, vol. 19, no. 3, pp. 561–568, Sep. 2004.
- [22] S. B. Leeb, J. L. Kirtley, W. W. Jr, Z. Remscrim, C. N. Tidd, J. A. Goshorn, K. Thomas, R. W. Cox, and R. Chaney, "How much dc power is necessary?" *Nav. Eng. J.*, vol. 122, no. 2, pp. 79–92, Jun. 2010.

- [23] C. A. Platero, F. Blázquez, P. Frías, and D. Ramírez, “Influence of rotor position in FRA response for detection of insulation failures in salient-pole synchronous machines,” *IEEE Trans. Energy Convers.*, vol. 26, no. 2, pp. 671–676, Jun. 2011.
- [24] I. M. Canay, “Causes of discrepancies on calculation of rotor quantities and exact equivalent diagrams of the synchronous machine,” *IEEE Transactions on Power Apparatus and Systems*, vol. PAS-88, no. 7, pp. 1114–1120, Jul. 1969.
- [25] M. R. Harris, P. J. Lawrenson, and J. M. Stephenson, *Per-Unit Systems With Special Reference to Electrical Machines*. Cambridge, U.K.: Cambridge Univ. Press, 1970.
- [26] G. R. Slemon, “Analytical models for saturated synchronous machines,” *IEEE Transactions on Power Apparatus and Systems*, vol. PAS-90, no. 2, pp. 409–417, Mar. 1971.
- [27] R. P. Schulz, W. D. Jones, and D. N. Ewart, “Dynamic models of turbine generators derived from solid rotor equivalent circuits,” *IEEE Trans. Power App. and Syst.*, vol. PAS-92, no. 3, pp. 926–933, May 1973.
- [28] R. G. Harley, D. J. N. Limebeer, and E. Chirricozzi, “Comparative study of saturation methods in synchronous machine models,” *IEE Proceedings B - Electric Power Applications*, vol. 127, no. 1, pp. 1–7, Jan. 1980.
- [29] L. Salvatore and M. Savino, “Experimental determination of synchronous machine parameters,” *IEE Proceedings B - Electric Power Applications*, vol. 128, no. 4, pp. 212–218, Jul. 1981.
- [30] J. E. Brown, K. P. Kovacs, and P. Vas, “A method of including the effects of main flux path saturation in the generalized equations of a.c. machines,” *IEEE Transactions on Power Apparatus and Systems*, vol. PAS-102, no. 1, pp. 96–103, Jan. 1983.
- [31] R. S. Ramshaw and G. Xie, “Nonlinear model of nonsalient synchronous machines,” *IEEE Transactions on Power Apparatus and Systems*, vol. PAS-103, no. 7, pp. 1809–1815, Jul. 1984.
- [32] G. Xie and R. S. Ramshaw, “Nonlinear model of synchronous machines with saliency,” *IEEE Transactions on Energy Conversion*, vol. EC-1, no. 3, pp. 198–204, Sep. 1986.
- [33] F. P. de Mello and L. N. Hannett, “Representation of saturation in synchronous machines,” *IEEE Transactions on Power Systems*, vol. 1, no. 4, pp. 8–14, Nov. 1986.
- [34] I. M. Canay, “Physical significance of sub-subtransient quantities in dynamic behaviour of synchronous machines,” *IEE Proceedings B - Electric Power Applications*, vol. 135, no. 6, pp. 334–340, Nov. 1988.
- [35] J. O. Ojo and T. A. Lipo, “An improved model for saturated salient pole synchronous motors,” *IEEE Transactions on Energy Conversion*, vol. 4, no. 1, pp. 135–142, Mar. 1989.

- [36] H. Bissig, K. Reichert, and T. S. Kulig, "Modelling and identification of synchronous machines, a new approach with an extended frequency range," *IEEE Trans. Energy Convers.*, vol. 8, no. 2, pp. 263–271, Jun. 1993.
- [37] I. M. Canay, "Determination of the model parameters of machines from the reactance operators $x_d(p)$, $x_q(p)$ (evaluation of standstill frequency response test)," *IEEE Trans. Energy Convers.*, vol. 8, no. 2, pp. 272–279, Jun. 1993.
- [38] ———, "Modelling of alternating-current machines having multiple rotor circuits," *IEEE Transactions on Energy Conversion*, vol. 8, no. 2, pp. 280–296, Jun. 1993.
- [39] A. Keyhani and H. Tsai, "Identification of high-order synchronous generator models from SSFR test data," *IEEE Trans. Energy Convers.*, vol. 9, no. 3, pp. 593–603, Sep. 1994.
- [40] J. L. Kirtley, "On turbine-generator rotor equivalent circuits," *IEEE Trans. Power Syst.*, vol. 9, no. 1, pp. 262–271, Feb. 1994.
- [41] I. Kamwa and P. Viarouge, "On equivalent circuit structures for empirical modeling of turbine-generators," *IEEE Transactions on Energy Conversion*, vol. 9, no. 3, pp. 579–592, Sep. 1994.
- [42] P. C. Krause, O. Wasynczuk, and S. D. Sudhoff, *Analysis of Electric Machinery*. New York: Wiley-IEEE Press, 1995.
- [43] P. L. Dandeno and M. R. Iravani, "Third order turboalternator electrical stability models with applications to subsynchronous resonance studies," *IEEE Transactions on Energy Conversion*, vol. 10, no. 1, pp. 78–86, Mar. 1995.
- [44] J. Tamura and I. Takeda, "A new model of saturated synchronous machines for power system transient stability simulations," *IEEE Transactions on Energy Conversion*, vol. 10, no. 2, pp. 218–224, Jun. 1995.
- [45] S.-A. Tahan and I. Kamwa, "A two-factor saturation model for synchronous machines with multiple rotor circuits," *IEEE Trans. Energy Convers.*, vol. 10, no. 4, pp. 609–616, Dec. 1995.
- [46] H. Tsai, A. Keyhani, J. A. Demcko, and D. A. Selin, "Development of a neural network based saturation model for synchronous generator analysis," *IEEE Transactions on Energy Conversion*, vol. 10, no. 4, pp. 617–624, Dec. 1995.
- [47] C.-M. Ong, *Dynamic Simulation of Electric Machinery Using Matlab/Simulink*. Englewood Cliffs, NJ: Prentice Hall, 1998.
- [48] K. A. Corzine, B. T. Kuhn, S. D. Sudhoff, and H. J. Hegner, "An improved method for incorporating magnetic saturation in the q-d synchronous machine model," *IEEE Transactions on Energy Conversion*, vol. 13, no. 3, pp. 270–275, Sep. 1998.

- [49] J. Verbeeck, R. Pintelon, and P. Guillaume, "Determination of synchronous machine parameters using network synthesis techniques," *IEEE Transactions on Energy Conversion*, vol. 14, no. 3, pp. 310–314, Sep. 1999.
- [50] J. Verbeeck, R. Pintelon, and P. Lataire, "Relationships between parameter sets of equivalent synchronous machine models," *IEEE Transactions on Energy Conversion*, vol. 14, no. 4, pp. 1075–1080, Dec. 1999.
- [51] —, "Influence of saturation on estimated synchronous machine parameters in standstill frequency response tests," *IEEE Transactions on Energy Conversion*, vol. 15, no. 3, pp. 277–283, Sep. 2000.
- [52] S. Pillutla and A. Keyhani, "Neural network based saturation model for round rotor synchronous generator," *IEEE Transactions on Energy Conversion*, vol. 14, no. 4, pp. 1019–1025, Dec. 1999.
- [53] —, "Neural network based modeling of round rotor synchronous generator rotor body parameters from operating data," *IEEE Transactions on Energy Conversion*, vol. 14, no. 3, pp. 321–327, Sep. 1999.
- [54] H. B. Karayaka, A. Keyhani, B. L. Agrawal, D. A. Selin, and G. T. Heydt, "Identification of armature, field, and saturated parameters of a large steam turbine-generator from operating data," *IEEE Transactions on Energy Conversion*, vol. 15, no. 2, pp. 181–187, Jun. 2000.
- [55] H. B. Karayaka, A. Keyhani, G. T. Heydt, B. L. Agrawal, and D. A. Selin, "Neural network based modeling of a large steam turbine-generator rotor body parameters from on-line disturbance data," *IEEE Transactions on Energy Conversion*, vol. 16, no. 4, pp. 305–311, Dec. 2001.
- [56] S. D. Sudhoff, D. C. Aliprantis, B. T. Kuhn, and P. L. Chapman, "An induction machine model for predicting inverter-machine interaction," *IEEE Transactions on Energy Conversion*, vol. 17, no. 2, pp. 203–210, Jun. 2002.
- [57] N. Dedene, R. Pintelon, and P. Lataire, "Estimation of a global synchronous machine model using a multiple-input multiple-output estimator," *IEEE Transactions on Energy Conversion*, vol. 18, no. 1, pp. 11–16, Mar. 2003.
- [58] D. C. Aliprantis, S. D. Sudhoff, and B. T. Kuhn, "Experimental characterization procedure for a synchronous machine model with saturation and arbitrary rotor network representation," *IEEE Trans. Energy Convers.*, vol. 20, no. 3, pp. 595–603, Sep. 2005.
- [59] I. M. Canay, "Causes of discrepancies on calculation of rotor quantities and exact equivalent diagrams of the synchronous machine," *IEEE Trans. Power App. and Syst.*, vol. PAS-88, no. 7, pp. 1114–1120, Jul. 1969.
- [60] *IEEE Guide for Synchronous Generator Modeling Practices and Applications in Power System Stability Analyses*, IEEE Std.1110-2002, Nov. 2003.

- [61] S. D. Pekarek, E. A. Walters, and B. T. Kuhn, "An efficient and accurate method of representing magnetic saturation in physical-variable models of synchronous machines," *IEEE Trans. Energy Convers.*, vol. 14, no. 1, pp. 72–79, Mar. 1999.
- [62] E. Levi, "Saturation modelling in d-q axis models of salient pole synchronous machines," *IEEE Trans. Energy Convers.*, vol. 14, no. 1, pp. 44–50, Mar. 1999.
- [63] D. C. Aliprantis, O. Wasynczuk, and C. D. Rodríguez Valdez, "A voltage-behind-reactance synchronous machine model with saturation and arbitrary rotor network representation," *IEEE Trans. Energy Convers.*, vol. 23, no. 2, pp. 499–508, Jun. 2008.
- [64] D. C. Aliprantis, S. D. Sudhoff, and B. T. Kuhn, "A synchronous machine model with saturation and arbitrary rotor network representation," *IEEE Trans. Energy Convers.*, vol. 20, no. 3, pp. 584–594, Sep. 2005.
- [65] A. M. Cramer, B. P. Loop, and D. C. Aliprantis, "Synchronous machine model with voltage-behind-reactance formulation of stator and field windings," *IEEE Trans. Energy Convers.*, vol. 27, no. 2, pp. 391–402, Jun. 2012.
- [66] E. Levi and V. A. Levi, "Impact of dynamic cross-saturation on accuracy of saturated synchronous machine models," *IEEE Trans. Energy Convers.*, vol. 15, no. 2, pp. 224–230, Jun. 2000.
- [67] S. D. Pekarek, O. Wasynczuk, and H. J. Hegner, "An efficient and accurate model for the simulation and analysis of synchronous machine/converter systems," *IEEE Trans. Energy Convers.*, vol. 13, no. 1, pp. 42–48, Mar. 1998.
- [68] G. R. Slemon, "An equivalent circuit approach to analysis of synchronous machines with saliency and saturation," *IEEE Trans. Energy Convers.*, vol. 5, no. 3, pp. 538–545, Sep. 1990.
- [69] Y. Xiao, G. R. Slemon, and M. R. Iravani, "Implementation of an equivalent circuit approach to the analysis of synchronous machines," *IEEE Trans. Energy Convers.*, vol. 9, no. 4, pp. 717–723, Dec. 1994.
- [70] X. Cao, A. Kurita, H. Mitsuma, Y. Tada, and H. Okamoto, "Improvements of numerical stability of electromagnetic transient simulation by use of phase-domain synchronous machine models," *Electrical Engineering in Japan*, vol. 128, no. 3, pp. 53–62, Apr. 1999.
- [71] L. Wang, J. Jatskevich, and S. D. Pekarek, "Modeling of induction machines using a voltage-behind-reactance formulation," *IEEE Trans. Energy Convers.*, vol. 23, no. 2, pp. 382–392, Jun. 2008.
- [72] L. Wang, J. Jatskevich, V. Dinavahi, H. W. Dommel, J. A. Martinez, K. Strunz, M. Rioual, G. W. Chang, and R. Iravani, "Methods of interfacing rotating machine models in transient simulation programs," *IEEE Trans. Power Del.*, vol. 25, no. 2, pp. 891–903, Apr. 2010.

- [73] L. Wang and J. Jatskevich, "A phase-domain synchronous machine model with constant equivalent conductance matrix for EMTP-type solution," *IEEE Trans. Energy Convers.*, vol. 28, no. 1, pp. 191–202, Mar. 2013.
- [74] M. Chapariha, L. Wang, J. Jatskevich, H. W. Dommel, and S. D. Pekarek, "Constant-parameter rl -branch equivalent circuit for interfacing ac machine models in state-variable-based simulation packages," *IEEE Trans. Energy Convers.*, vol. 27, no. 3, pp. 634–645, Sep. 2012.
- [75] M. Chapariha, F. Therrien, J. Jatskevich, and H. W. Dommel, "Constant-parameter circuit-based models of synchronous machines," *IEEE Trans. Energy Convers.*, vol. 30, no. 2, pp. 441–452, Jun. 2015.
- [76] R. W. Ferguson, R. Herbst, and R. W. Miller, "Analytical studies of the brushless excitation system," *Transactions of the American Institute of Electrical Engineers. Part III: Power Apparatus and Systems*, vol. 78, no. 4, pp. 1815–1821, Dec. 1959.
- [77] E. C. Whitney, D. B. Hoover, and P. O. Bobo, "An electric utility brushless excitation system," *Transactions of the American Institute of Electrical Engineers. Part III: Power Apparatus and Systems*, vol. 78, no. 4, pp. 1821–1824, Dec. 1959.
- [78] S. Feng, X. Jianbo, W. Guoping, and X. Yong-hong, "Study of brushless excitation system parameters estimation based on improved genetic algorithm," in *Third International Conference on Electric Utility Deregulation and Restructuring and Power Technologies (DRPT)*, Apr. 2008, pp. 915–919.
- [79] V. Ruuskanen, M. Niemela, J. Pyrhonen, S. Kanerva, and J. Kaukonen, "Modelling the brushless excitation system for a synchronous machine," *IET Electric Power Applications*, vol. 3, no. 3, pp. 231–239, May 2009.
- [80] A. Griffo, R. Wrobel, P. H. Mellor, and J. M. Yon, "Design and characterization of a three-phase brushless exciter for aircraft starter/generator," *IEEE Trans. Ind. Appl.*, vol. 49, no. 5, pp. 2106–2115, Sep. 2013.
- [81] D. C. Aliprantis, S. D. Sudhoff, and B. T. Kuhn, "A brushless exciter model incorporating multiple rectifier modes and preisach's hysteresis theory," *IEEE Trans. Energy Convers.*, vol. 21, no. 1, pp. 136–147, Mar. 2006.
- [82] T. L. Skvarenina, S. Pekarek, O. Wasynczuk, P. C. Krause, R. J. Thibodeaux, and J. Weimer, "Simulation of a more-electric aircraft power system using an automated state model approach," in *IECEC 96. Proceedings of the 31st Intersociety Energy Conversion Engineering Conference*, vol. 1, Aug. 1996, pp. 133–136 vol.1.
- [83] A. M. Cramer, X. Liu, Y. Zhang, J. D. Stevens, and E. L. Zivi, "Early-stage shipboard power system simulation of operational vignettes for dependability assessment," in *2015 IEEE Electric Ship Technologies Symposium (ESTS)*, Jun. 2015, pp. 382–387.

- [84] D. Montenegro, G. A. Ramos, and S. Bacha, "A-diakoptics for the multicore sequential-time simulation of microgrids within large distribution systems," *IEEE Trans. Smart Grid*, vol. 8, no. 3, pp. 1211–1219, May 2017.
- [85] T. Zouaghi and M. Poloujadoff, "Modeling of polyphase brushless exciter behavior for failing diode operation," *IEEE Trans. Energy Convers.*, vol. 13, no. 3, pp. 214–220, Sep. 1998.
- [86] S. Chiniforoosh, J. Jatskevich, A. Yazdani, V. Sood, V. Dinavahi, J. A. Martinez, and A. Ramirez, "Definitions and applications of dynamic average models for analysis of power systems," *IEEE Trans. Power Del.*, vol. 25, no. 4, pp. 2655–2669, Oct. 2010.
- [87] S. Chiniforoosh, H. Atighechi, and J. Jatskevich, "A generalized methodology for dynamic average modeling of high-pulse-count rectifiers in transient simulation programs," *IEEE Trans. Energy Convers.*, vol. 31, no. 1, pp. 228–239, Mar. 2016.
- [88] H. A. Petrosen and P. C. Krause, "A direct-and quadrature-axis representation of a parallel ac and dc power system," *IEEE Trans. Power App. Syst.* *, vol. PAS-85, no. 3, pp. 210–225, Mar. 1966.
- [89] P. C. Krause and T. A. Lipo, "Analysis and simplified representations of a rectifier-inverter induction motor drive," *IEEE Trans. Power App. Syst.* *, vol. PAS-88, no. 5, pp. 588–596, May 1969.
- [90] E. Kimbark, *Direct current transmission*. Wiley-Interscience, 1971.
- [91] S. D. Sudhoff and O. Wasynczuk, "Analysis and average-value modeling of line-commutated converter-synchronous machine systems," *IEEE Trans. Energy Convers.*, vol. 8, no. 1, pp. 92–99, Mar. 1993.
- [92] S. D. Sudhoff, K. A. Corzine, H. J. Hegner, and D. E. Delisle, "Transient and dynamic average-value modeling of synchronous machine fed load-commutated converters," *IEEE Trans. Energy Convers.*, vol. 11, no. 3, pp. 508–514, Sep. 1996.
- [93] M. Shahnazari and A. Vahedi, "Improved dynamic average modelling of brushless excitation system in all rectification modes," *IET Electric Power Applications*, vol. 4, no. 8, pp. 657–669, Sep. 2010.
- [94] J. Jatskevich and T. Aboul-Seoud, "Impedance characterization of a six-phase synchronous generator-rectifier system using average-value model," in *Canadian Conference on Electrical and Computer Engineering*, vol. 4, May 2004, pp. 2231–2234 Vol.4.
- [95] J. Jatskevich, S. D. Pekarek, and A. Davoudi, "Parametric average-value model of synchronous machine-rectifier systems," *IEEE Trans. Energy Convers.*, vol. 21, no. 1, pp. 9–18, Mar. 2006.

- [96] —, “Fast procedure for constructing an accurate dynamic average-value model of synchronous machine-rectifier systems,” *IEEE Trans. Energy Convers.*, vol. 21, no. 2, pp. 435–441, Jun. 2006.
- [97] J. Jatskevich and S. D. Pekarek, “Numerical validation of parametric average-value modeling of synchronous machine-rectifier systems for variable frequency operation,” *IEEE Trans. Energy Convers.*, vol. 23, no. 1, pp. 342–344, Mar. 2008.
- [98] H. Atighechi, S. Chiniforoosh, K. Tabarraee, and J. Jatskevich, “Average-value modeling of synchronous-machine-fed thyristor-controlled-rectifier systems,” *IEEE Transactions on Energy Conversion*, vol. 30, no. 2, pp. 487–497, Jun. 2015.
- [99] Y. Zhang and A. M. Cramer, “Numerical average-value modeling of rotating rectifiers in brushless excitation systems,” *IEEE Transactions on Energy Conversion*, vol. PP, no. 99, pp. 1–1, 2017.
- [100] S. Ebrahimi, N. Amiri, H. Atighechi, Y. Huang, L. Wang, and J. Jatskevich, “Generalized parametric average-value model of line-commutated rectifiers considering ac harmonics with variable frequency operation,” *IEEE Transactions on Energy Conversion*, vol. PP, no. 99, pp. 1–1, 2017.
- [101] *Simulink User’s Guide*, MathWorks, Natick, MA.
- [102] *Automated State Model Generator (ASMG) Reference Manual*, P. C. Krause and Associates, Inc., West Lafayette, IN, 2002.
- [103] F. Therrien, M. Chapariha, and J. Jatskevich, “Pole selection procedure for explicit constant-parameter synchronous machine models,” *IEEE Transactions on Energy Conversion*, vol. 29, no. 3, pp. 790–792, Sep. 2014.
- [104] S. J. Salon, *Finite Element Analysis of Electrical Machines*. New York, NJ: Springer, 1995.

Vita

YuQi Zhang was born in Yichun, Jiangxi, China.

Education

M.S. in Electrical Engineering, University of Kentucky, Lexington, KY, U.S., June, 2014.

B.S. in Electrical Engineering, Harbin Institute of Technology, Harbin, China, July, 2005.

Awards

Best Papers in the IEEE TRANSACTIONS ON ENERGY CONVERSION 2016-2017.

Publications

1. Y. Zhang and A. M. Cramer, "Formulation of Rectifier Numerical Average-Value Model for Direct Interface with Inductive Circuitry," submitted in IEEE Transactions on Energy Conversion, Jan. 2018.
2. Y. Zhang and A. M. Cramer, "Numerical Average-Value Modeling of Rotating Rectifiers in Brushless Excitation Systems," in IEEE Transactions on Energy Conversion, vol. 32, no. 4, pp. 1592-1601, Dec. 2017.
3. Y. Zhang and A. M. Cramer, "Unified Model Formulations for Synchronous Machine Model With Saturation and Arbitrary Rotor Network Representation," in IEEE Transactions on Energy Conversion, vol. 31, no. 4, pp. 1356-1365, Dec. 2016.

4. Y. Zhang and A. M. Cramer, "Market-based control of electric ship power systems," 2017 IEEE Electric Ship Technologies Symposium (ESTS), Arlington, VA, 2017, pp. 372-379.
5. Y. Zhang, N. Uzegbunam, W. Xu and S. c. S. Cheung, "RoboMirror: Simulating a mirror with a robotic camera," 2016 IEEE International Conference on Image Processing (ICIP), Phoenix, AZ, 2016, pp. 1734-1738.
6. A. M. Cramer, X. Liu, Y. Zhang, J. D. Stevens and E. L. Zivi, "Early-stage ship-board power system simulation of operational vignettes for dependability assessment," 2015 IEEE Electric Ship Technologies Symposium (ESTS), Alexandria, VA, 2015, pp. 382-387.